FINAL REPORT

Next Generation Data Collection System for Mobile Detection and Discrimination of Unexploded Ordnance

SERDP Project MM-1571

September 2008

Dr. Stephen Billings, Lead Performer
Sky Research, Inc.

Mr. Darren O'Connor
Stratton Park Engineering Corporation

Dr. Paul Lawson
Stratton Park Engineering Corporation

Dr. Lin Ping Song
University of British Columbia

Dr. Douglas Oldenburg
University of British Columbia

Strategic Environmental Research and Development Program

REPORT DOCUMENTATION PAGE

Form Approved
OMB No. 0704-0188

1. AGENCY USE ONLY (Leave blank)	2. REPORT DATE	3. REPORT TYPE AND DATES COVERED
	10 September 2008	Final Report, 2007-2008

4. TITLE AND SUBTITLE
Next Generation Data Collection System for Mobile Detection and Discrimination of Unexploded Ordnance

5. FUNDING NUMBERS
SERDP MM-1571

6. AUTHOR(S)
Dr. Stephen Billings, Sky Research, Inc.
Darren O'Connor and Dr. Paul Lawson , SPEC, Inc.
Dr. Lin Ping Song and Dr. Douglas Oldenburg, UBC-GIF

7. PERFORMING ORGANIZATION NAME(S) AND ADDRESS(ES)
Sky Research, Inc
445 Dead Indian Memorial Road,
Ashland, OR 97520

PERFORMING ORGANIZATION REPORT NUMBER

9. SPONSORING/MONITORING AGENCY NAME(S) AND ADDRESS(ES)
SERDP
901 North Stuart Street, Suite 303,
Arlington, VA 22203

10.SPONSORING/MONITORING AGENCY REPORT NUMBER

11. SUPPLEMENTARY NOTES

12a. DISTRIBUTION/AVAILABILITY STATEMENT
Unclassified/Unlimited

12b. DISTRIBUTION CODE

13. ABSTRACT (Maximum 200 words)
A feasibility analysis for one-pass detection and discrimination of unexploded ordnance was conducted. Position and orientation accuracies were optimized through Kalman filtering of Global Positioning System and tactical grade Inertial Motion Unit data output from a Novatel SPAN. In controlled tests on a rotating amusement park carousel and when mounted on a towed array, the SPAN demonstrated positional and orientation accuracies of better than 2 cm and 0.6 degrees respectively. Survey design analysis and monte-carlo simulations were used to predict the expected performance of next-generation cart and towed-array systems. A modification of the TEMTADS cued interrogation array, comprising four 1 m by 1 m transmitters that fire-sequentially, display excellent discrimination potential. The four-transmitter TEMTADS with 5 cm position error and 2 degree orientation error outperformed a EM63 equivalent sensor with 1 cm and 1 degree error. We conclude that one-pass detection and discrimination will be feasible at many UXO contaminated sites.

14. SUBJECT TERMS
Positioning accuracy
UXO discrimination
Navigation systems

15. NUMBER OF PAGES
75

16. PRICE CODE

17. SECURITY CLASSIFICATION OF REPORT	18. SECURITY CLASSIFICATION OF THIS PAGE	19. SECURITY CLASSIFICATION OF ABSTRACT	20. LIMITATION OF ABSTRACT
Unclassified	Unclassified	Unclassified	Unlimited

Executive Summary

This project was formulated in response to the Munitions Management Statement of Need MMSON-07-04, "Advanced technologies for detection, discrimination and remediation of munitions and explosives of concern (MEC): UXO technology". Several years ago it was determined that discrimination performance using single-component electromagnetic induction (EMI) sensors in the field had been uniformly poor relative to expectations, predominantly due to stringent requirements on positional accuracy and signal-to-noise ratio (SNR). This lead to the development of a number of multi-transmitter, multi-receiver EMI sensors that could be deployed in a cued-interrogation mode so that data could be collected without moving the platform. Initials tests with these systems have shown excellent discrimination potential. However, at many sites, we believe that the most cost-effective discrimination strategy will be to deploy a time-domain EMI one-pass detection and discrimination system where positional and orientation accuracy, data-density and SNR are maximized. In this project, we conduct a feasibility analysis of such a system. We focus on (i) estimating the position and orientation accuracies that can be achieved in a dynamic survey mode; and (ii) on simulating the discrimination performance of a number of candidate EMI sensors when subjected to different position and orientation errors.

For sensor positioning we use the commercial off the shelf, Novatel SPAN system which comprises a Global Positioning System (GPS) receiver combined with a Honeywell HG1700 tactical grade Inertial Motion Unit (IMU) which has a drift rate of $1° \text{ hr}^{-1}$. The data are post-processed in a commercially available package called Inertial Explorer. Two positional tests were conducted, the first using a Rotating Amusement Park (RAP) carousel, and the second using an EM61 towed array.

The RAP was instrumented with a precision optical encoder and the SPAN system was installed on a tilt-table at a fixed position on the RAP. The known distance of the SPAN system from the axis of revolution of the RAP ride, the tilt table angle and the optical encoder information provided accurate ground-truth. The GPS and IMU data from the SPAN were augmented by an optical encoder attached to a bicycle wheel that was attached to the RAP and which was in constant contact with the ground. For one run, when the system was moving at a brisk 2 meters per second, the position estimated from the IMU/GPS combination had a root-mean-square error of between 1.1 and 1.8 cm.

For the second position test, a laser prism was mounted on the rear left corner of an EM61 towed-array, about 1.5 m away from the Novatel SPAN system which was mounted on the tow-bar in line with the center of the towed-array. The SPAN-predicted position of the prism was compared to the prism position measured with a Trimble SCS930 Universal Total Station. Data were collected at various speeds between 0.2 and 1.3 meters per second, on both smooth and rough ground, with the array traveling along, straight or curved paths and with ramps sometimes present that one side of the cart had to travel over. Amongst all the tests the root-mean-squared (RMS) horizontal error varied from a minimum of 0.6 cm to a maximum of 1.7 cm. These represent upper bounds on

the horizontal positional error of the SPAN system. If the error was entirely due to the SPAN heading, the RMS heading error would vary from a minimum of 0.2^o to a maximum of 0.6^o. RMS errors of the 3-D positions (including elevation) varied from 0.8 to 3.2 cm. The runs with larger errors typically exhibited systematic biases in the elevation angles. This indicates that there may 1-2 cm magnitude systematic differences in the SPAN elevations along adjacent transect paths.

Numerical investigation of simulation performance occurred along two fronts. The first was semi-analytical and based on estimating the expected errors in the positions and polarizabilities of a buried metallic object. The second was based on monte-carlo simulations of systems subjected to different amounts of sensor, position and orientation noise. Five different sensor systems were simulated, including two Geonics EM63 equivalent, one with a single receiver coil, the other with three orthogonal receiver coils. The remaining three systems were based on the 25 transmitter / 25 receiver TEMTADS system developed at the Naval Research Laboratory. The first was deployed in the standard cued mode, with the other two deployed in dynamic mode, one with a single large transmitter around the array, and the other with four 1 m by 1 m transmitters that fire sequentially. Both the semi-analytical and Monte-Carlo approaches demonstrated the excellent performance of the cued-system. They also revealed that the dynamic variants of that system have significantly improved performance over an EM63 equivalent. In particular, the multiple receiver coils makes the TEMTADS more tolerant of position and orientation errors than the EM63. The four-transmitter TEMTADS with 5 cm position error and 2^o orientation error outperforms an EM63 with 1 cm and 1^o error.

We conclude that the SPAN system is able to position a towed-array at better than 1-2 cm positional error and better than 0.6^o orientation error. Combined with the fact that multi-sensor systems such as the TEMTADS are more tolerant of position/orientation error we hypothesize that, at many sites, one-pass detection and discrimination with a suitably modified TEMTADS would be feasible. Furthermore, depending on anomaly density, this one pass survey would be more cost-effective than the two pass mode required when the TEMTADS is deployed in a cued-mode.

TABLE of CONTENTS

LIST of FIGURES

LIST OF TABLES

ACRONYMS

AOL	Advanced Ordnance Locator
CDU	Control and display unit
cm	centimeter
COTS	Commercial-off-the-shelf
DAS	Data acquisition system
dB	Decibel
D&D	Detection & discrimination
DoD	Department of Defense
EM	Electromagnetic
EMI	Electromagnetic induction
ESTCP	Environmental Security Technology Certification Program
FIM	Fisher information matrix
FLBGR	Former Lowry Bombing and Gunnery Range
GHz	Gigahertz
GPS	Global positioning system
HH	hand-held
Hz	hertz
IE	Inertial Explorer
IMU	Inertial motion unit
IR	infrared
KF	Kalman Filter
m	meter
μs	microsecond
ms	millisecond
MEC	Munitions and explosives of concern
mph	miles per hour
MTADS	Multi-sensor Towed Array Detection System
NRL	Naval Research Laboratory
pps	pulse-per-second
RAP	Rotating amusement park
RMSE	Root-mean-square error
rpm	Rotations per minute
RTK	Real-Time Kinematic
RTS	Robotic total station
R_x	Receive
SERDP	Strategic Environmental Research and Development Program
SPAN	Synchronized Position Attitude & Navigation
SNR	Signal-to-noise ratio
TEM	Time-domain electromagnetic
T_x	Transmit
UTM	Universal Transverse Mercator
UXO	Unexploded ordnance
VSEMS	Vehicular Simultaneous EM and Magnetometer System

1 PROJECT BACKGROUND AND OBJECTIVES

This project was formulated in response to the Munitions Management Statement of Need MMSON-07-04, "Advanced technologies for detection, discrimination and remediation of munitions and explosives of concern (MEC): UXO technology". The prohibitive costs of excavating all geophysical anomalies are well known and are one of the greatest impediments to efficient cleanup of unexploded ordnance (UXO) contaminated lands at department of defense (DoD) sites. Therefore, innovative discrimination techniques are required. Several years ago it was determined that discrimination performance using single-component electromagnetic induction (EMI) sensors in the field had been uniformly poor relative to expectations, predominantly due to stringent requirements on positional accuracy and signal-to-noise ratio (SNR) (e.g. Bell, 2005). This lead to the development of a number of multi-transmitter, multi-receiver EMI sensors (e.g. Berkeley UXO Discriminator, Naval Research Laboratory [NRL] cued-interrogation array or TEMTADS) that could be deployed in a cued-interrogation mode so that data could be collected without moving the platform. Initials tests with these systems have shown excellent discrimination potential. However, the need to deploy the systems in a cued-mode can significantly increase the time and costs of the geophysical survey. Recent results at the Former Lowry Bombing and Gunnery Range (FLBGR, Billings et al., 2007) and the former Camp Sibert (e.g Billings et al., 2008) have demonstrated that, at certain sites, effective discrimination is possible by careful interpretation of single-component time-domain EMI data collected in a one-pass detection and discrimination mode. The discrimination strategy was more effective when the time-decay was measured over a wider time range (180 microseconds [μs] to 25 milliseconds [ms]). At many sites, we believe that the most cost-effective discrimination strategy will be to deploy a time-domain EMI one-pass detection and discrimination system where positional and orientation accuracy, data-density and SNR are maximized. In this project, we conduct a feasibility analysis of a one-pass detection and discrimination system.

1.1 THEORETICAL BACKGROUND

EMI is generally considered to be the most promising technology for discriminating between UXO and non-UXO items. In the EMI method, a time varying field illuminates a buried, conductive target. Currents induced in the target then produce a secondary field that is measured at the surface. EM data inversion involves using the secondary field generated by the target for recovery of the position, orientation, and parameters related to the target's material properties and shape. In the UXO community, the inverse problem is usually simplified by assuming that the secondary field can be accurately approximated as a dipole.

In general, time-domain electromagnetic (TEM) sensors use a step-off field to illuminate a buried target. The currents induced in the buried target decay with time, generating a decaying secondary field that is measured at the surface.

The time-varying secondary magnetic field $\mathbf{B}(t)$ at a location $\mathbf{r}$ from the dipole $\mathbf{m}(t)$ is

$$\mathbf{B}(t) = \frac{\mu_o}{4\pi r^3}\mathbf{m}(t)\cdot\left(3\hat{\mathbf{r}}\hat{\mathbf{r}} - \overline{\overline{\mathbf{I}}}\right) \quad (1)$$

where $\hat{\mathbf{r}} = \mathbf{r}/|\mathbf{r}|$ is the unit-vector pointing from the dipole to the observation point, I is the 3 x 3 identity matrix, $\mu_o = 4\ \pi$ x 10^{-7} H/m is the permittivity of free space and $r = |\mathbf{r}|$ is the distance between the center of the object and the observation point.

The dipole induced by the interaction of the primary field $\mathbf{B}_o$ and the buried target is given by

$$\mathbf{m}(t) = \frac{1}{\mu_o}\overline{\overline{\mathbf{M}}}(t)\cdot\mathbf{B}_o \quad (2)$$

where $\mathbf{M}(t)$ is the target's polarization tensor. The polarization tensor governs the decay characteristics of the buried target and is a function of the shape, size, and material properties of the target. The polarization tensor is written as:

$$\overline{\overline{\mathbf{M}}}(t) = \begin{bmatrix} L_1(t) & 0 & 0 \\ 0 & L_2(t) & 0 \\ 0 & 0 & L_3(t) \end{bmatrix} \quad (3)$$

where we use the convention that $L_1(t_1) \geq L_2(t_1) \geq L_3(t_1)$, so that polarization tensor parameters are organized from largest to smallest. The polarization tensor components are parameterized such that the target response can be written as a function of a model vector containing components that are a function of target characteristics.

The success of dipole model based discrimination algorithms depends on the accuracy with which the polarization tensor can be estimated. With noisy and inaccurately positioned data it can be difficult to constrain the depth and location of the item, leading to considerable uncertainty in the magnitude and ratio of the components of the polarization tensor (e.g. Smith *et al*., 2004). For instance, when using EM61 Hand Held (EM61-HH) data, Bell (2005) found that a SNR of 30 decibels (dB) and positional accuracy on the centimeter level were required for successful discrimination. Bell further argues that the data quality requirements of the EM61-HH (17 centimeter [cm] coils) are indicative of those required by other sensors such as the regular 1 meter (m) by 0.5 m coil EM61. This perception that such stringent data quality objectives are a requirement for advanced discrimination has led many groups to practically abandon efforts to develop one-pass detection and discrimination systems and instead concentrate on the development of cued interrogation platforms (e.g. ESTCP MM-0601).

Cued interrogation is one way to optimize data quality because only a limited area about each anomaly needs to be surveyed. As a second data collection effort is required, the survey and processing costs for UXO remediation using cued-interrogation will usually be higher than for one-pass detection and discrimination (D&D). For this latter mode of surveying, two different sophisticated towed array systems have been developed over the past decade: the Multi-sensor Towed Array Detection System (MTADS) developed by the NRL and the Vehicular Simultaneous EM and Magnetometer System (VSEMS)

developed by Geo-Centers (now SAIC). Both systems use purposely built tow-vehicles and trailers and both deploy arrays of Geonics EM61 metal detectors and total-field magnetometers. The main difference is that the VSEMS collects the EM and magnetic data in one-pass, while the MTADS uses two passes. Neither of these systems can achieve the data quality requirements suggested by Bell (2005) and as he points out, '*the discrimination performance using the MTADS EM61 array in the field has been uniformly poor relative to expectations based on results of inverting controlled measurements over ordnance and exploded shell fragments'*.

To address the issue of whether data quality requirements for discrimination are as stringent as Bell (2005) found for the EM61-HH, we first outline the four main types of features extracted from the polarization tensor that are used for discrimination:

1) Size of the object: typically inferred from $L_1(t)$ at one or more time-channels, or may involve some combination of the three polarizations;
2) "Two-dimensional" shape of the object: typically inferred from the values of $L_1(t)$ and $L_2(t)$ at a particular time-channel;
3) "Three dimensional" shape of the object: typically inferred from the values of all three polarizations. For example, asymmetric scrap has $L_1(t_1) \neq L_2(t_1) \neq L_3(t_1)$ while ferrous items with cylindrical symmetry have $L_1(t_1) \geq L_2(t_1) = L_3(t_1)$ and aluminium items with cylindrical symmetry have $L_1(t_1) = L_2(t_1) \geq L_3(t_1)$;
4) Time-decay characteristics of the object: typically inferred from the primary polarization $L_1(t)$ using ratios of time-channels or power-law and/or exponential fits to the decay shape.

Recent results achieved with EM61 and EM63 sensors deployed at FLBGR and the Former Camp Sibert (Billings *et al*., 2007 and 2008) demonstrated good discrimination performance in the presence of positional errors on the order of 2 to 5 cm. The analysis focused on features 1) and 4) (the size and time-decay properties) derived from the primary polarization tensor. These features were used to guide a statistical classifier and rank anomalies according to UXO likelihood. As only the primary polarization was used, the features were more robust and tolerant of positional error and sensor/geological noise, than feature vectors extracted from the secondary and tertiary polarizations (the "two" and "three" dimensional features above). The longer measurement time of the EM63 resulted in more effective discrimination due to the significantly different late-time behavior of the UXO items compared to the encountered clutter. Therefore, we suggest that previous poor discrimination performance was partly due to the use of unstable polarization tensor features (the secondary and tertiary polarizations) and the lack of time-decay information past 1.2 ms.

It's apparent that the more accurate the position and orientation information, the better the discrimination performance. However, we assert that, at many sites, UXO discrimination will be achievable using one-pass detection and discrimination. Therefore, we don't believe that these systems should be ignored in favor of static cued-interrogation platforms.

The following issues need to be considered when contemplating using an EMI sensor in a one-pass detection and discrimination mode:

1) Positional and orientation accuracy: In a dynamic mode, discrimination relies on accurate relative position between successive measurements. We will tackle this issue using a Novatel SPAN system comprising a real-time kinematic global positioning sytem (RTK GPS) and a tactical grade inertial motion unit (IMU), with the dynamical state of the system determined through a Kalman filter.
2) Timing accuracy: The accurate and stable synchronization of the different sensor components is a critical requirement for successful discrimination based on dynamically collected data. At a forward traverse rate of 1 m/s, a timing error of 1 ms translates to an 0.1 cm error in the position.
3) Measurement time and data-density: The longer the time-range measured, the further the array will move during a single measurement, the lower the density of the measurements and the lower the SNR at the later time-channels. Systems such as the TEMTADS have the ability to measure the time-decay to 25 ms after transmitter shut-off, with a single measurement with that time range requiring about 100 ms to collect. The Environmental Security Technology Certification Program (ESTCP) MM-0504 demonstrations at FLBGR and Camp Sibert demonstrated that the wider measurement range of the EM63 (to 25 ms) resulted in superior discrimination performance to the EM61 (to 1 ms). It's not clear as to whether measurements are required all the way out to 25 ms and some compromise of measuring out to, say, 8 ms, may prove to be more effective (measurements require 32 ms and hence the data-density will be about 3 times greater than at 25 ms decay).
4) Signal to noise ratio: In cued-mode, the data are stacked to improve SNR. In dynamic mode, the choice of the number of stacks involves a compromise between improving SNR and blurring of spatial detail. The lower the number of stacks, the less movement that occurs during each measurement. The greater the current in the transmitter the better the SNR, but it also requires waiting longer before taking the first measurement. Movement during the receive period also introduces dynamic motion noise which lowers the SNR. To combat that noise source, an extra reference sensor could be mounted at a higher elevation than the detection sensors. The reference sensor will sense approximately the same ambient noise as the other receivers, and due to its increased height, will have a significantly reduced response from any items of interest.
5) Change in background response from the ground: During mobile data collection, the geometry of the array relative to the ground is constantly changing. Emerging work from project Strategic Environmental Research and Development Program (SERDP) project MM-1573 indicates that the resulting variation in the background response can be significant and has the potential to degrade the accuracy of any polarization tensors extracted from the data. With knowledge of the array geometry relative to the ground, variations in the background response can be modeled and removed from the data.

6) Excitation of multiple axes: To be able to discriminate using feature vectors from all three polarizations, the object must be excited from a wide-range of different angles. When surveying with the MTADS EM61, array data are collected in two orthogonal excitations as a single direction does not result in significant excitation perpendicular to the direction of travel. To avoid the need for two data collection passes, a one-pass detection and discrimination system must utilize an intelligent transmitter firing sequence so that all principal axes of a buried object are excited.

The main focus of this research project is on addressing point 1) above: that is on optimizing the position and orientation accuracy of the EMI sensor. We address this challenge in the next section through the integration of a GPS with an IMU using a Kalman filter framework. Specifically, we rigorously test the positional accuracy of a Novatel SPAN system mounted on a rotating amusement park (RAP) ride. Then in the following section, we conduct a more realistic positional accuracy test with the SPAN mounted on a towed-array that is driven over both rough and smooth ground. Next, we use survey design techniques and numerical simulations to characterize the expected performance of different time-domain EMI sensors deployed in a one-pass detection and discrimination mode. In the final section, we provide recommended modifications to create an alternative dynamic deployment mode of the TEMTADS cued-interrogation sensor.

2 OPTIMIZATION OF POSITION AND ORIENTATION ACCURACY

As outlined in the last section, accurate position and orientation information are required for successful discrimination using a moving system. One of the most effective ways to obtain this information is to combine a GPS (or a laser positioning system) with an IMU (e.g. Steinhurst et al., 2005; Billings et al., 2007). The GPS and IMU can both provide information on either or both position and orientation. For the GPS, orientation information can be obtained through the use of multiple receivers. For the IMU, position and orientation can be obtained through accelerometers and gyroscopes. To obtain position information from the IMU requires a double integration of the IMU acceleration data. Due to the accumulation of errors, IMU position errors will quickly exceed the centimeter-level position accuracy specification. Frequent updating of the IMU position is therefore needed to achieve the required accuracy. GPS on the other hand, can deliver excellent position accuracy, but has a problem called "cycle slips", which are in essence gross errors leading to a discontinuity in the trajectory. The combination of the two measuring systems, therefore, offers a number of advantages. In the absence of cycle slips, the excellent positioning accuracy of differential GPS can be used to provide frequent updates for the inertial system. The inertial sensors' orientation information and the precise short-term position and velocity can be used for GPS cycle slip detection and correction. The objective of an effective processing strategy is to minimize position and orientation errors by combining IMU and GPS measurements in a manner that optimizes the attributes of each measurement system.

Steinhurst et al. (2005) implemented a combined GPS and IMU position/orientation system on the GEMTADS towed-array platform. They used three Trimble MS750 GPS antennas that operate in a RTK moving base-mode to give platform positions at 20 hertz (Hz) and platform orientation at 10 Hz. A Crossbow VG600CA Vertical Gyroscope was used to provide platform pitch and roll at a rate of up to 83 Hz. To combine the GPS angles and the IMU angles, the IMU data were high-pass filtered to retain the high frequency variation of the platform angles, the GPS data were low-pass filtered to retain the stable base in the angles, and the two were combined. To maintain RTK status, the Trimble moving base requires that all three receivers continuously track a minimum of four common satellites. In field trials, it was found that the RTK status would be lost for several minutes after trees or other obstacles obscured the sky-view of one or more of the receivers. At the sites surveyed this RTK problem only occurred infrequently and Steinhurst *et al*. (2005) estimated that the platform position was accurate to approximately 3 cm and the orientation to within 1^{o}.

The method developed in Steinhurst *et al*. (2005) combines some, *but not all,* of the relative advantages of the GPS and IMU. For instance, the linear and angular accelerations from the IMU were only used for calculating the platform pitch and roll and not for determining the position of the platform. A Kalman Filter (e.g. Kalman, 1960) provides a computational framework for optimally combining the GPS and IMU data. In

the next section we briefly describe the Kalman Filter algorithm and then describe an experiment conducted to determine the accuracy of the Novatel SPAN system. This comprises a GPS receiver combined with a Honeywell HG1700 tactical grade IMU (see http://www.novatel.com/Documents/Papers/HG1700_SPAN62.pdf for a list of technical specifications), which has a drift rate of 1° hr^{-1}. The data are post-processed in a commercially available package called Inertial Explorer.

2.1 KALMAN FILTER THEORY

A Kalman Filter (KF) is a recursive data processing algorithm that estimates the state of a noisy linear dynamic system; i.e., a vector *x* consisting of n variables that describe some interesting properties of the system. In our case, the properties of interest are the position of the sensor, consisting of the (*x, y, z)* coordinates, and the orientation φ of the sensor. In practice, a KF has access to several measurement sources that are corrupted with noise. In our application, IMU measurements are made using 3-axis accelerometers and rate gyros, and 3-dimensional position from a GPS. An additional measurement of sensor velocity is made using the bicycle wheel encoder. If the measurement noise sources follow a Gaussian distribution, which is a good assumption in this case, then the KF estimator is statistically optimal with respect to any reasonable measure for optimization (Grewal and Andrews 1993). The KF processes all available measurements to estimate the state, both accurate and inaccurate measurements. It uses knowledge of the system and sensor dynamics, probabilistic descriptions of the system and measurement noises, and any available data about the initial values of the state.

A KF can be called a state estimator that works on a prediction-correction basis. This means that it computes a "belief" in a certain state estimate by first making a prediction based on the dynamics of the system and later correcting this prediction using measurements of the system. In the case of a sensor on a RAP (or a towed-array cart in the field), there is a time history of the motion and orientation of the sensor on the RAP (or the cart). The KF first makes a prediction of the sensor position and orientation based on the time history. Next, it corrects this estimate using measurements, such as relative measurements of integrated acceleration and angular velocity, and absolute measurements such as GPS position. The main objective of the KF is to optimize the estimate of the true state of the system. In particular, it estimates the state and gives a measure of how certain it is that the state estimate is the true state. What makes estimating the state difficult is that the state will change over time and both the state and the measurements are subject to noise.

Formal derivations of KF theory are lengthy, complicated, and available in several texts and journal articles (e.g., Kalman 1960; Maybeck 1979; Grewal and Andrews 1993; Welch and Bishop 2001). Here we present a brief overview of KF theory in order to obtain some insight into how to optimize its application.

The KF estimates the conditional probability of being in state x_k given available measurements $z_1 \ldots z_k$. The probability of being in state x_k given observations $z_1 \ldots z_k$ is called the "belief ",

$$Bel(x_k) = P(x_k|z_1, \ldots, z_k). \tag{4}$$

This belief definition can then be split into the prior belief $Bel^-(x_k)$ and the posterior belief $Bel^+(x_k)$ using Bayes' rule, the theorem of total probability, and the Markov assumption. Then,

$$\begin{aligned} Bel^-(x_k) &= P(x_k|z_1, \ldots, z_{k-1}) \\ &= \int_{\Xi} P(x_k|x_{k-1}) Bel^+(x_{k-1}) dx_{k-1} \\ Bel^+(x_k) &= P(x_k|z_1, \ldots, z_k) \\ &= \frac{P(z_k|x_k) Bel^-(x_k)}{P(z_k|z_1, \ldots, z_{k-1})}. \end{aligned} \tag{5}$$

The prior belief is the conditional probability of being at state x_k given all the measurements z up to step k. The posterior belief is the conditional probability of being at state x_k given all the measurements z up to and including step k. In order to compute the beliefs, expressions are needed for the system model $P(x_k \mid x_{k\_1})$ and the measurement model $P(x_k \mid x_k)$.

The KF computes the belief by first computing the prior belief and then computing the posterior belief. The computation of the prior belief $Bel^-(x_k)$ can be seen as a prediction of the state of the system after one time step. Without looking at new measurement information, the prior belief estimates what the state of the system most likely is after one step. It uses a model of the system $P(x_k \mid x_{k\_1})$ and the belief in what the state was at the last time step $Bel^+(x_k)$. Due to noise in the system, there may be a prediction error.
That is, the prediction may be different from the true state. The computation of the posterior belief $Bel^+(x_k)$ can be seen as a correction of the state estimate resulting from the prediction. After the KF has calculated the prior belief, new measurement information gives direct information about the true state of the system. This measurement information may be used to correct the predicted state. For this the KF uses a model of the measurements $P(x_k \mid x_k)$. This model describes how likely it is that given a state x_k a sensor reading results in measurement z_k. Given this model and a real measurement, the KF corrects the prior belief in the state $Bel^-(x_k)$. Thus, the KF predicts the true state
of the system after a time step has passed and it then corrects its prediction using measurements that are made of the true state. The KF is therefore also called a predictor-corrector state estimator (Maybeck 1979).

2.2 SPAN POSITION AND ORIENTATION ACCURACY TESTING

We set out to accurately measure the position and orientation accuracy achievable in a dynamic platform. Position errors of less than 1 cm and orientation to 0.1 degree or less were targeted. Initially a custom system featuring the following components was proposed:

- On board GPS with RTK base station.
- Custom inertial measurement unit (IMU).
- Wheels custom fit with optical encoders to provide distance measurements.
- Trimble laser-based robotic total station (RTS) position measurement system.
- Custom hardware data acquisition system (DAS).
- Custom Kalman filtering software to optimize the data set.

To demonstrate the feasibility of achieving the above accuracies, a system using an off the shelf GPS and IMU from Novatel was used. The SPAN system, as it is called, comes with its own custom Kalman filtering software, Inertial Explorer (IE), enabling a significant cost savings to be realized during this initial phase. IE is optimized for 1 Hz position estimates, targeting vehicle navigation applications but can be used for estimation of positions at up to a 100 Hz rate.

The system in Figure 1 was placed on a rotating amusement park (RAP) ride at a fixed distance from the center of the ride. The set up is shown in Figure 2. The RAP provides the means to repeatedly place the detection system over a locus of points on a circle. One of the two encoders shown in Figure 1 was used to measure the instantaneous angle of the RAP. This angle, along with the known distance between the center of the RAP and the detection system provides a highly accurate estimate of the system position at fixed points in time.

Figure 1 shows a block diagram of the system components used to collect position data. A laptop computer logs incoming data from both the SPAN system and the DAS. Both the SPAN and DAS time tag their respective data with highly accurate GPS times. This yields the capability to highly accurately post-process the parallel data streams. The SPAN system time stamping is accurate to the 10s of nanoseconds, and the DAS is accurate to 10 microseconds. The SPAN system is used to measure GPS and IMU data. The DAS is used to measure optical encoder data.

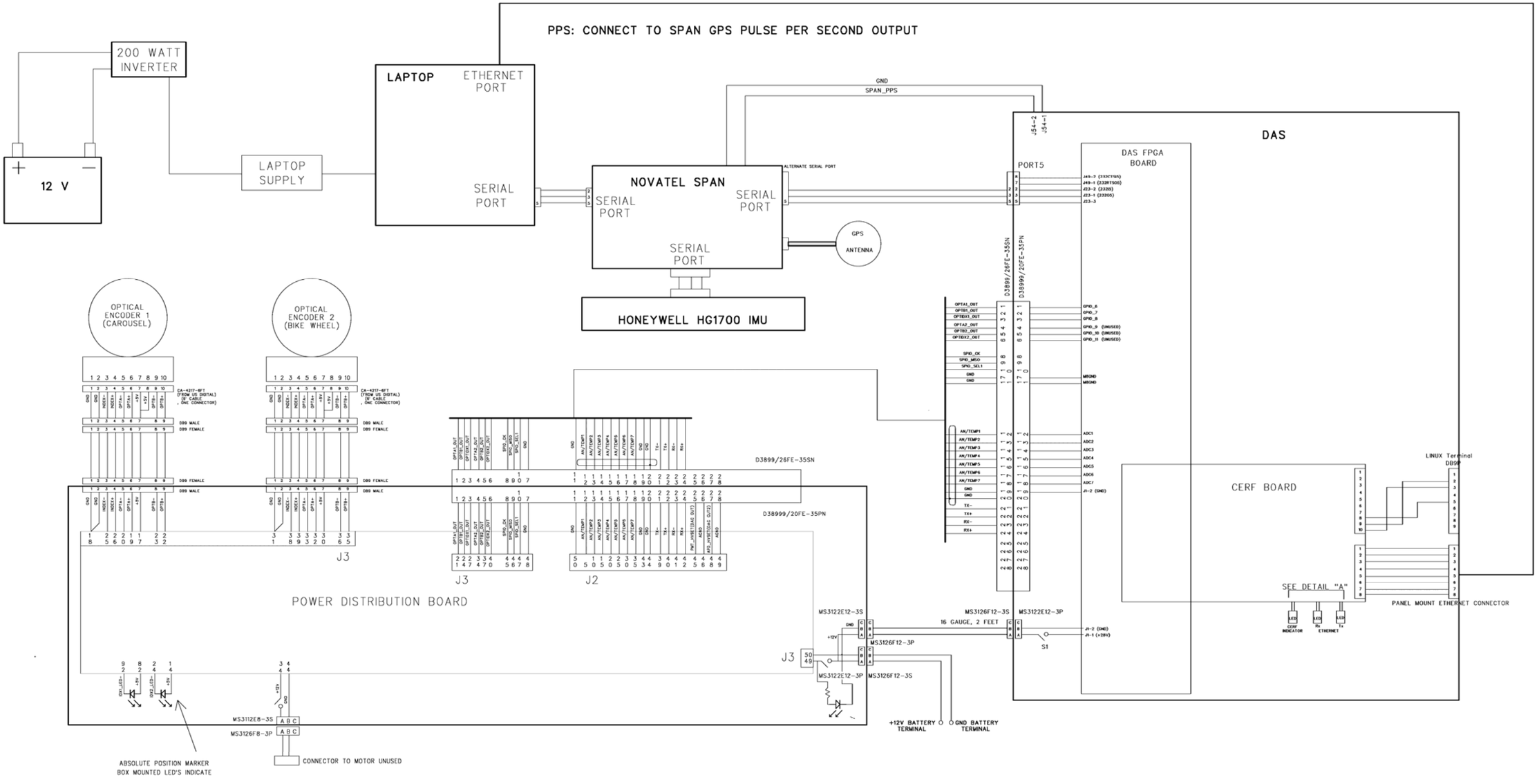

Figure 1: Block diagram of SERDP1571 test system.

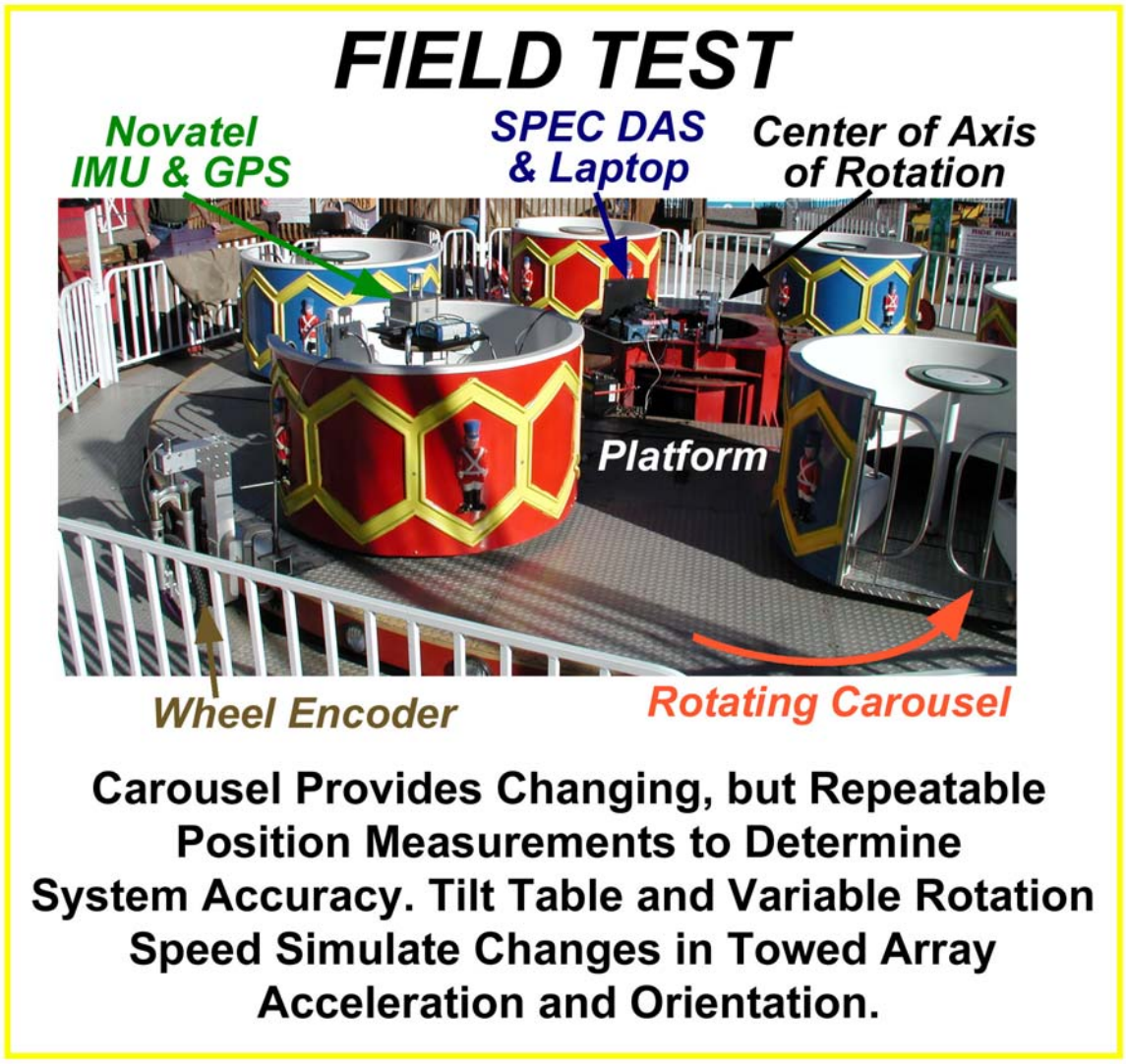

Figure 2: Rotating amusement park (RAP) ride with position measurement system components.

A second optical encoder was integrated into a bicycle wheel, seen in the lower left of Figure 2. The two encoders provide a very accurate measurement of the location of the SPAN system at any given time. The next stage of this project was spent using IE to predict SPAN location vs. time and comparing the predictions to the known location based on the encoder data.

In addition to improving the accuracy of the SPAN location measurement, the bicycle wheel measurement provides a proof of concept for using such a device on the UXO measurement platform in the future.

2.3 DESIGN OF ENCODER ASSEMBLIES

Figure 3 shows a detailed schematic of the center encoder assembly. The optical encoders purchased from US Digital require a tight mechanical tolerance for mounting. The Mylar encoder wheel has 1800 lines used to measure position and is sensed with a differential optical sensor that measures in quadrature using two detectors for a resolution of 7200 positions for one full rotation. The encoder wheel must be positioned to the optical sensor within 0.026 inches in the radial direction and 0.020 inches in the axial direction. The methods used to mount the encoders to both the center shaft assembly and the bicycle wheel must maintain these tolerances during normal operation.

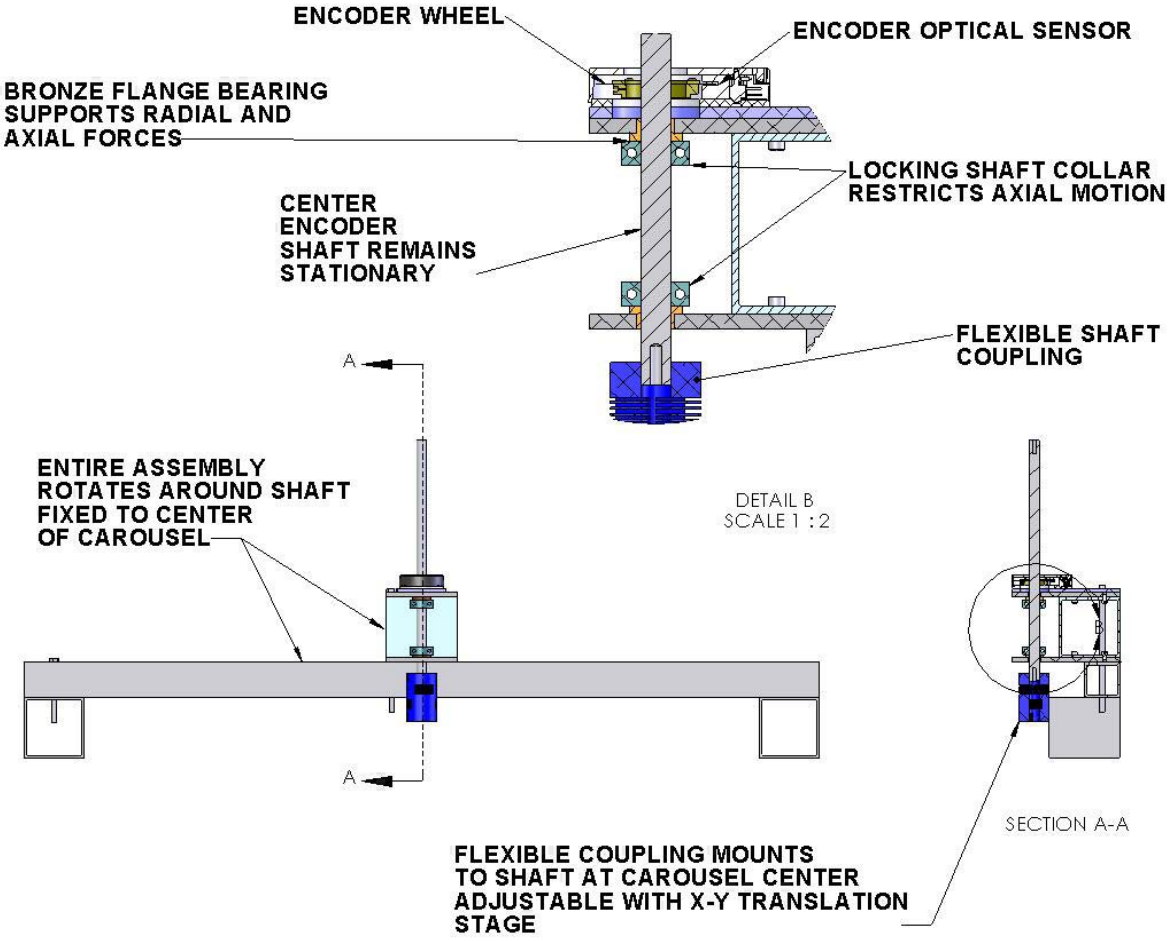

Figure 3: Schematic of center shaft optical encoder assembly.

In the case of the center shaft assembly, an encoder mounting scheme was designed to maintain these tolerances using two shafts joined with a flexible coupling. As seen in

Figure 3, detail B, the shaft used to mount the encoder wheel utilizes two flange bearings and two locking shaft collars to limit the radial and axial motion of this shaft between the mount plates. This confines the encoder wheel to a range of motion that is within the tolerances stated above to prevent the wheel from colliding with the optical sensor and damaging the fragile encoder wheel. A flexible shaft coupling is then used to connect to another shaft mounted to an X-Y translation stage which is clamped near the center of the carousel.

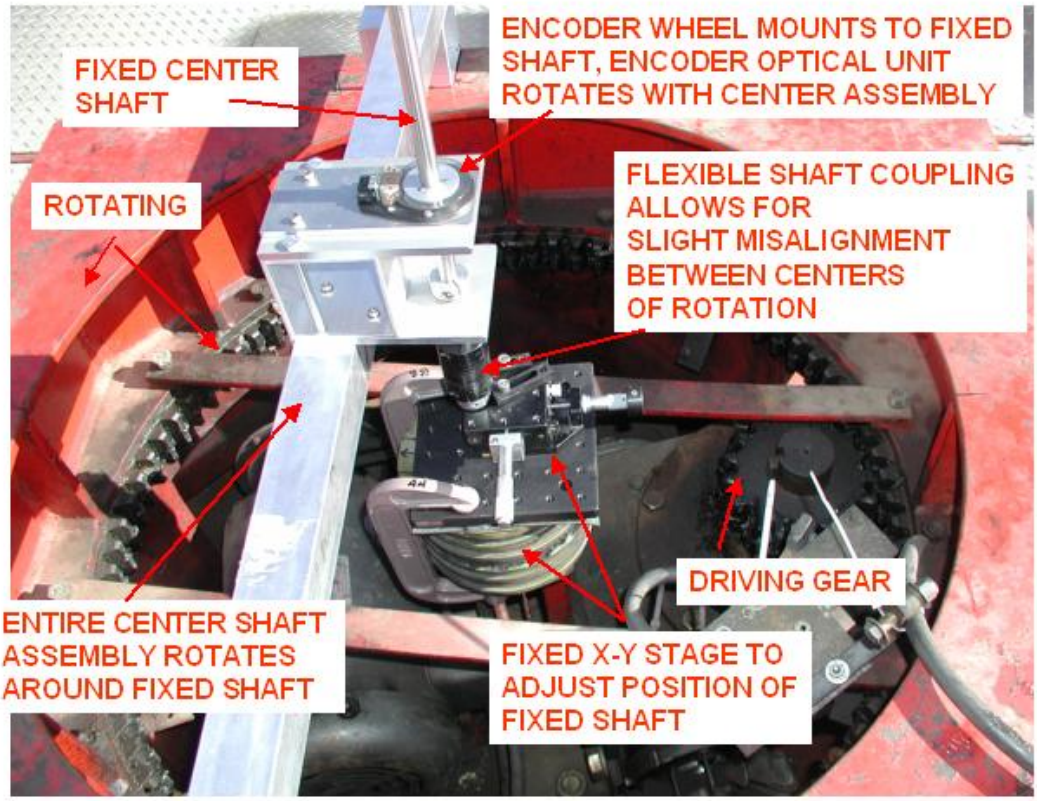

Figure 4: Photograph of center encoder assembly mounted to carousel.

Figure 4 is a photograph showing the center shaft assembly mounted to the center of the carousel. The X-Y stage, flexible shaft coupling, and center shaft are clamped to a cylindrical part that is stationary. The driving gear is rotated by a stationary motor and drives a planetary gear that rotates the entire carousel. Because there is no geometric center of rotation position indicated on the carousel, an iterative procedure was used to position the center encoder assembly by rotating the carousel and adjusting the X-Y stage to place the shaft at the geometric center of rotation. The flexible coupling allows for two shafts to have a slight misalignment and still count the rotations accurately with the optical encoder.

Figure 5 is a schematic of the bicycle wheel encoder assembly. This wheel is mounted to the carousel at the outer edge and rolls on the stationary platform tracking the motion of the moving carousel with approximately 19.16 rotations of the bike wheel for one

carousel revolution. A mountain bike suspension fork is used to maintain contact between the wheel and platform. The suspension fork is necessary because the vertical clearance between the bottom of the rotating carousel and the stationary platform varies up to 75 mm during one revolution of the carousel. A 16-inch diameter wheel is used to allow for clearance to mount the encoder assembly within the limits of the fork.

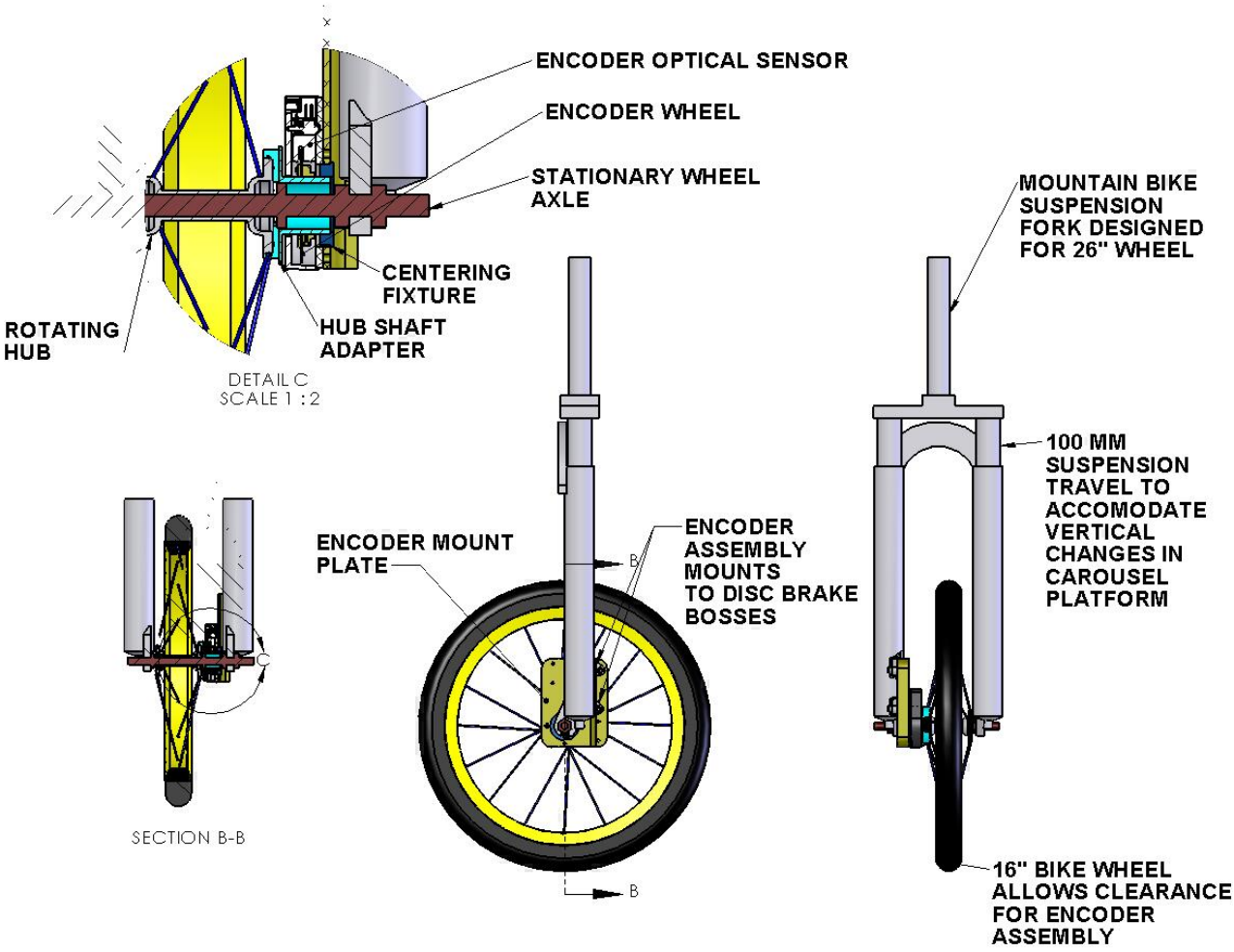

Figure 5: Schematic of bike wheel encoder assembly.

In the case of the bicycle wheel encoder assembly, the optical sensor of the encoder is stationary and the encoder wheel is mounted to a hub shaft adapter that rotates. Detail C of Figure 5 shows the hub shaft adapter mounted to the rotating hub of the wheel. The encoder optical sensor mounts on a plate this is mounted to the disc brake mount bosses on the suspension fork. A centering fixture is used during assembly to position all the components to the correct position. The adjustment screws are then tightened and the centering fixture is removed. This approach successfully allowed the encoder wheel to rotate within the mechanical limits described above and not collide with the optical sensor.

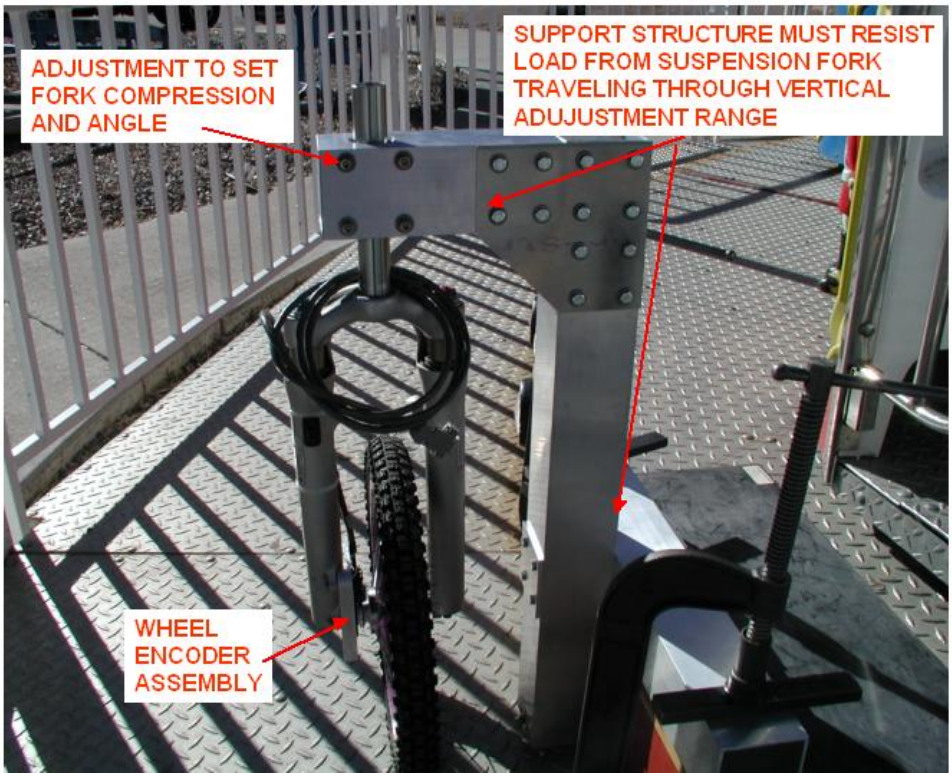

Figure 6: Bicycle wheel assembly mounted to carousel.

Figure 6 is a photograph of the bike wheel encoder assembly mounted to the carousel. A rigid support structure is necessary to rigidly couple the wheel assembly to the carousel to accurately track the rotation. The mount structure must also rigidly resist the compression force of the air shock as the suspension force is compressed. An adjustment mechanism is used to position the angle of the fork and set the vertical position to maintain rolling contact as the carousel rotates.

2.4 RESULTS

On December 13th, 2007, the system was installed and operated. In addition to the system components discussed, a base station GPS also was set up and operated. The base station is necessary to attain the maximum accuracy from the SPAN GPS measurements. The following sections describe the results.

2.4.1 Encoder Measurements

Figure 7 is a diagram showing the relationship between the center encoder, the wheel encoder, and the SPAN GPS system. The encoder assemblies were installed on the carousel and several data collection runs were performed. The data was quality checked to insure smooth movement of the encoders and verify no slipping of the center shaft. Figure 8 is a plot of the raw encoder data. The blue trace is the center encoder and the red trace is the wheel encoder. In this data set, the carousel is gradually accelerating and coming up to full speed. As expected, several wheel encoder revolutions occur for each

center encoder revolution and the peaks representing one revolution get closer together as the speed increases.

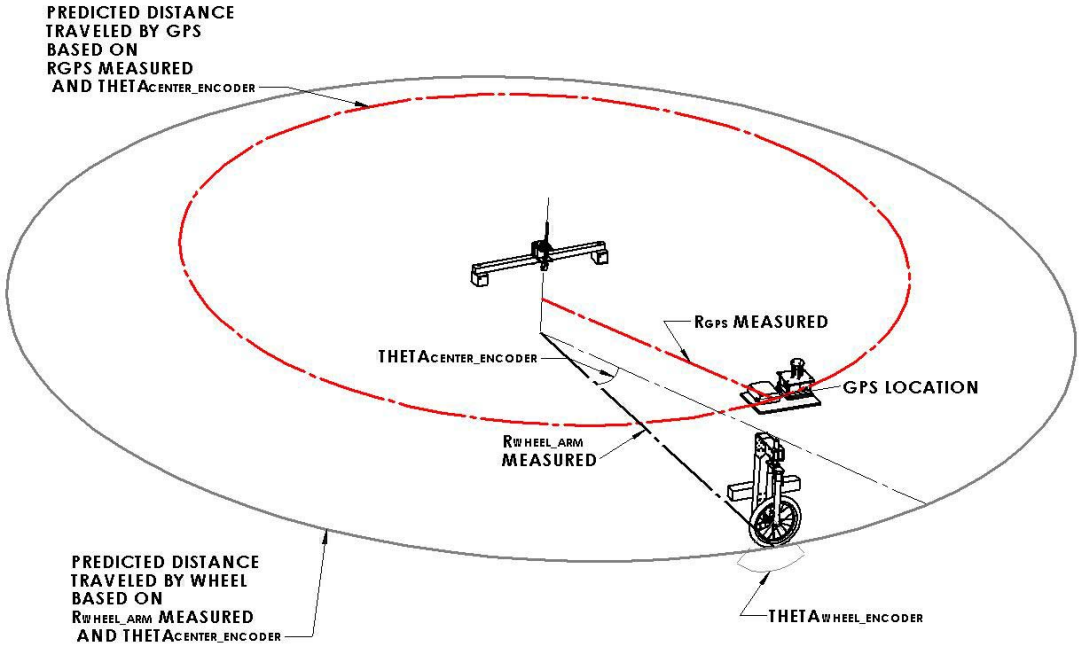

Figure 7: Diagram showing relationship between center encoder and wheel encoder.

Based on the information in Figure 8, it is possible to determine the number of wheel revolutions for each carousel revolution and determine if this number is constant, as expected and desired. It is also possible to determine the distance traveled by the wheel for each carousel revolution. The top graph in Figure 9 is a plot of the number of wheel revolutions for consecutive carousel rotations. Over the course of 25 rotations the average number of wheel revolutions per carousel revolution is 19.169.

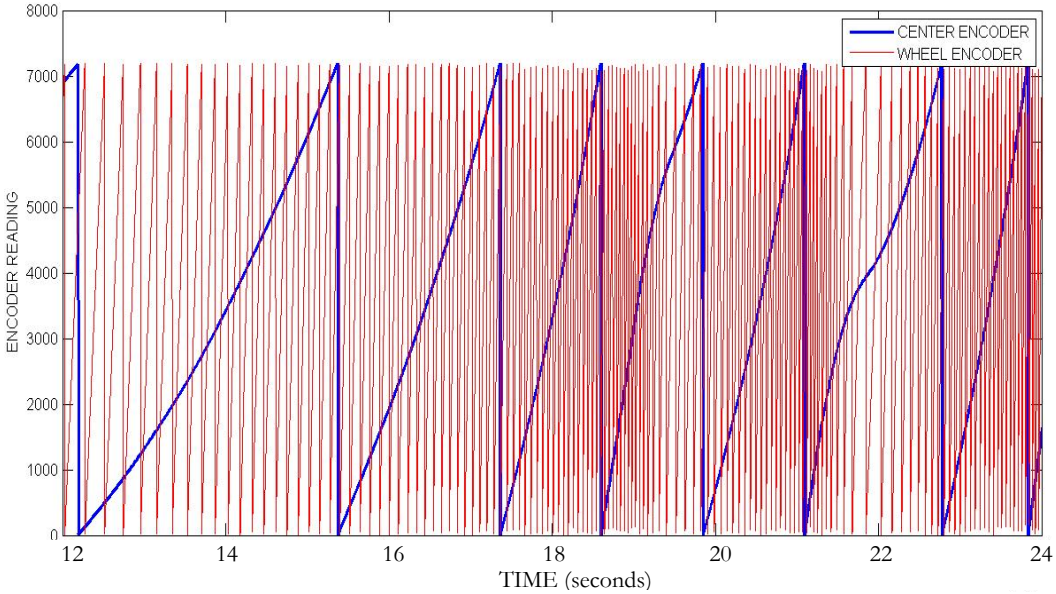

Figure 8. Plot of center encoder and wheel encoder as carousel rotates.

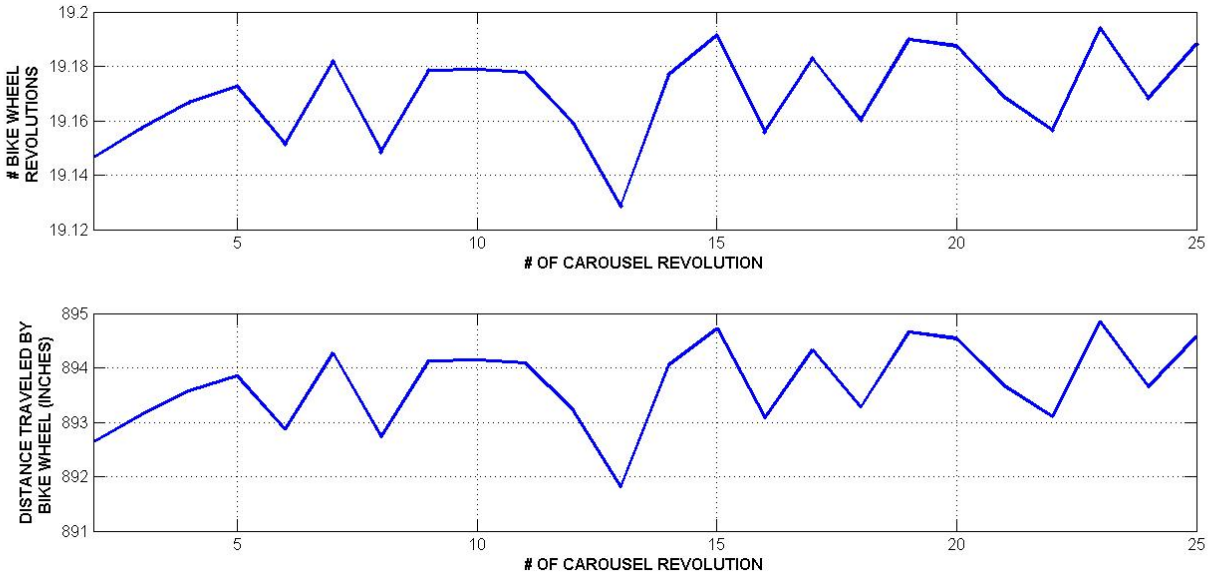

Figure 9. Number of carousel revolutions versus number of wheel revolutions (top) and number of carousel revolutions versus distance traveled by wheel (bottom).

The total distance traveled by the wheel for one carousel revolution can be estimated using the value for R_{wheel_arm}=142.18 inches and multiplying by 2π to get 893.39 inches. Since we know the number of revolutions required for the wheel to cover this distance, we can solve for the radius of the bicycle wheel. This is not easily measurable as the air-filled wheel undergoes some compression due to the force of the suspension fork. Furthermore, this compression changes depending on the force applied by the fork. Using an average of 19.169 revolutions to cover the 893.39 inches, the radius of the

wheel is calculated to be 14.835 inches. Using this value, the distance covered by the wheel for each revolution is plotted in the lower graph of Figure 9.

2.4.2 IMU Measurements

On the SPAN system, the antenna was located directly above the IMU center with a zero offset in the X and Y direction, and 0.167 m of vertical separation. Figure 10 is a photograph of the assembly. The IMU and GPS antenna are mounted on a tilt table to vary the roll angle of the assembly. The tilt table is precisely varied by rotating a micrometer. During one of the experimental runs, while the carousel was stationary, the tilt table angle was changed 0.763° by moving the micrometer two full revolutions. Figure 11 is a plot of the roll angle recorded by the IMU at a 5 Hz sample rate. The IMU roll angle indicates a change of 0.768°, extremely close to the change induced by the tilt table. Once the carousel starts rotating again, the roll angle varies as the GPS rotates through each carousel revolution. The predicted vs. measured discrepancy of 0.005° highlights the accuracy of the SPAN IMU.

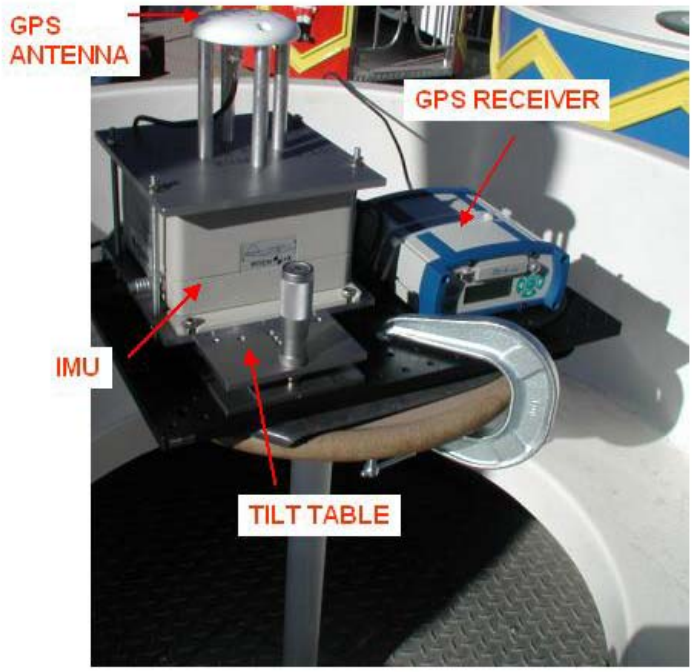

Figure 10: IMU/ GPS assembly mounted to carousel.

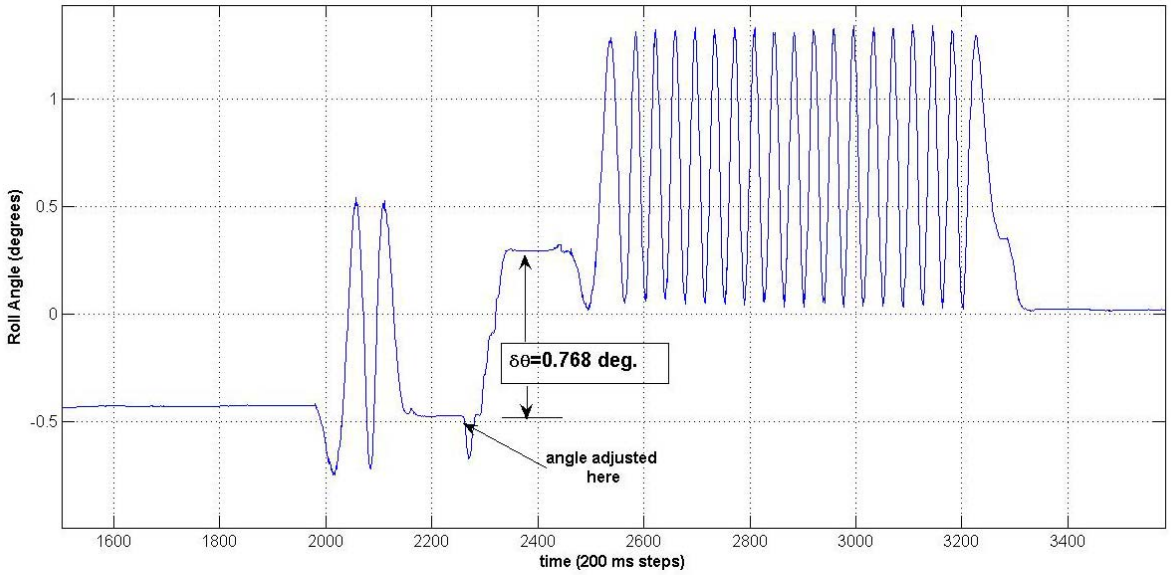

Figure 11: Roll angle recorded by the IMU showing the effect of varying the tilt table angle.

2.4.3 SPAN Measurements

Figure 12 shows a plot of the estimated positions produced by the IE software using the SPAN GPS and IMU data, plus the base station GPS data. The location of each data point was stored in Universal Transverse Mercator (UTM) coordinates, along with the time of each data point, to a data file. This data was read into Matlab. The set of data points is assumed to match the equation of a circle centered at coordinates (x_o, y_o):

$$(x - x_o)^2 + (y - y_o)^2 = R^2 \quad (6)$$

A least squares regression was used to determine the values of x_o and y_o, and a new set of variables were solved:

$$x' = x - x_o \quad (7)$$

$$y' = y - y_o \quad (8)$$

Using these variables to estimate the position on a circle centered at x', y' = 0 allowed comparisons between the IE estimated position and the known position, the latter based on the center encoder data. The least squares regression also yielded the value of the radius R: 2.406 meters. During the test set up, the value R_{GPS} was measured to be 2.419 meters. This difference of 1.33 cm could have been an error in the measured value of R_{GPS} taken using a tape measure. Future processing of more data sets, each yielding a linear regression value for the radius R, will provide more confidence in the actual value. However, for this analysis, the value of 2.406 meters is used hereafter.

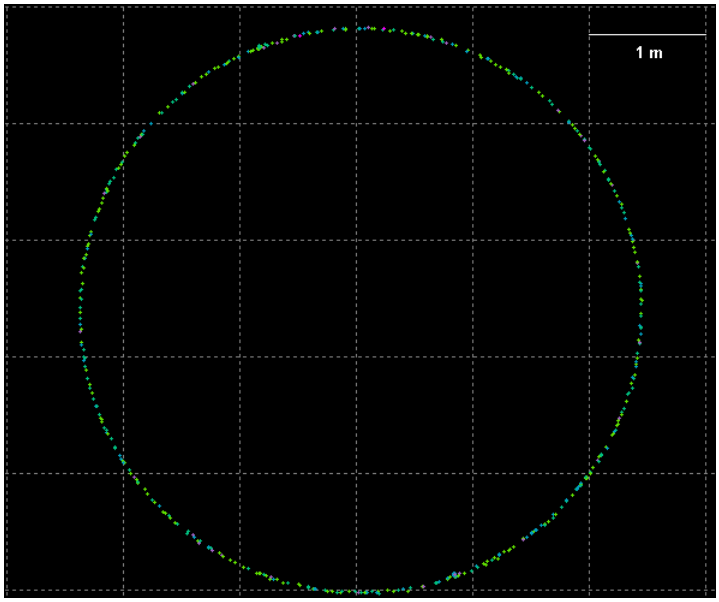

Figure 12: Plot of Inertial Explorer estimated position output after filtering for one of the carousel measurement runs.

Figure 13 (top) shows the estimated radius and. the estimated constant value versus time during the data collection period. For this data set, the RAP was stopped for three minutes during the middle of the data collection, and this period can be seen to be relatively quiet in the plot. On either side of that stoppage, the carousel was moving relatively fast with the SPAN system covering 2 meters each second.

Using the angle data from the encoder, and the constant value for the radius discussed above, a known position vs. time was generated. The absolute value of the distance at each point between the known position and the IE estimated position is shown in the bottom plot of Figure 13. This is not simply the difference between the constant radius value and estimated radius value shown in the top plot; it also takes into account the angular position of the SPAN system at each point in time.

For the first part of the plot the mean error is 1.54 cm, the standard deviation is 0.80 cm and the root-mean-square error (RMSE) (which combines the bias and variance) is 1.74 cm. For the last part of the plot the mean is 1.14 cm, the standard deviation is 0.58 cm and the RMSE is 1.28 cm. The error is less after the stoppage and we suspect that this may be due to better satellite coverage.

The RMSE in position is between 1.1 and 1.8 cm: this is approaching our specified performance objective of 1 cm. We are encouraged by this result, as it was obtained using default values for the noise densities of the IMU and GPS. Unlike GPS, inertial computations are very sensitive to the input of *a priori* stochastic information that is available for each inertial system. According to Novatel, as a rule of thumb, the more expensive the IMU, the less likely it is to achieve poor results from a non-optimal choice of input statistical quantities. A poor choice of noise densities for a navigation grade

inertial system may simply provide the user with a sub-optimal set of outputs, say for attitude. An inappropriate choice of noise densities for an inexpensive IMU (e.g., MEMS array with a drift of 300° per hour) may result in meaningless attitude information. The Honeywell tactical grade IMU used in the SPAN system is state-of-the-art and has excellent performance specifications.

Rather than focusing on optimizing the accuracy of the positions in the RAP test, we instead designed another more realistic test of the positional/orientation accuracy of the SPAN.

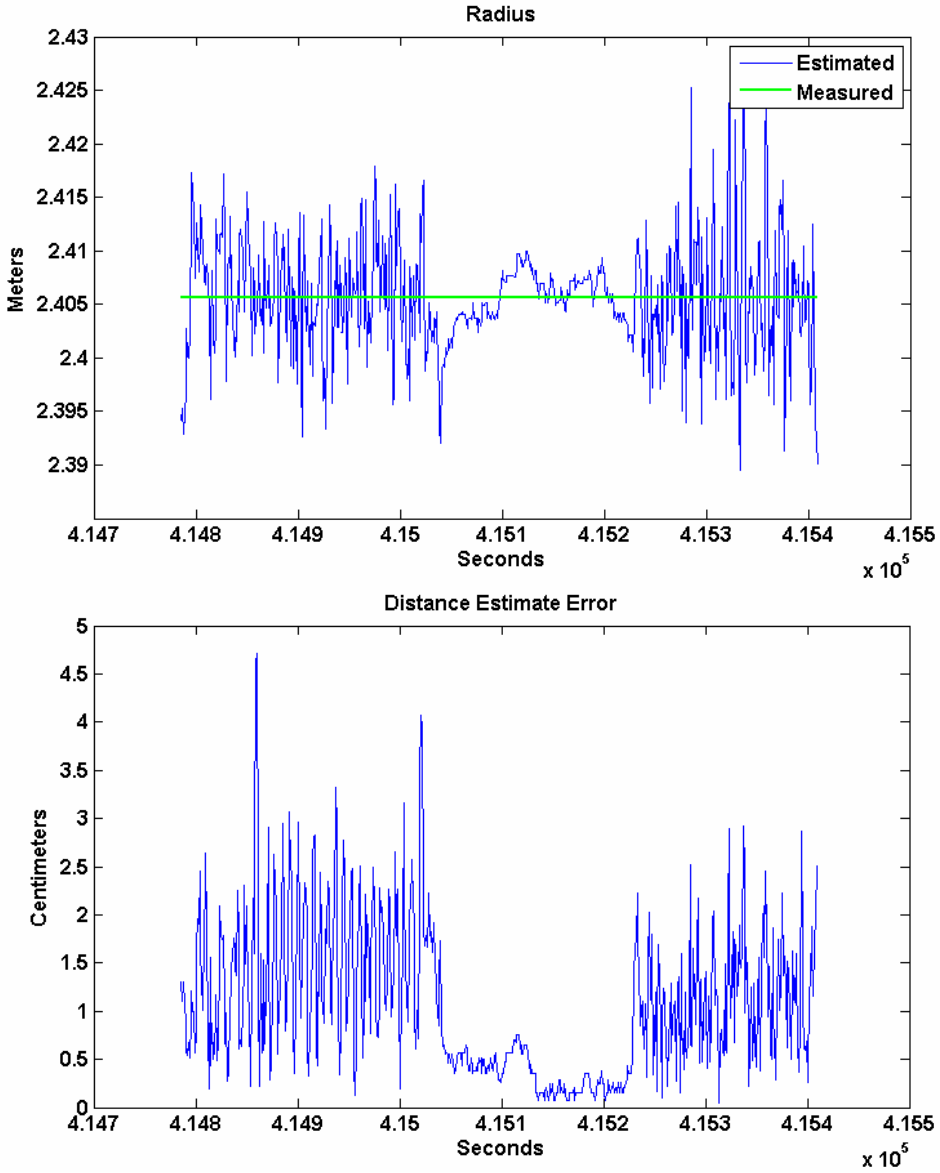

Figure 13: Radius estimate vs. time (top) and location estimate error (bottom) for one data set taken on the RAP platform.

3 POSITIONAL AND ORIENTATION ACCURACY TEST ON A TOWED ARRAY

While the accuracies achieved with the RAP test were encouraging, the test was not representative of the dynamic environment of a towed-array or cart collecting data over a real-world site. The dynamics in the RAP were not representative of cart-motions in the field, but perhaps more importantly, the RAP tests concentrated on determining the accuracy of predicting the position of the GPS antenna. In practice, there is almost always an offset (sideways, forwards, up/down or all three) between the antenna and the sensor. That is, for rectangular EMI sensor we are more interested in the positions of the four corners of the transmitter and receiver coils than in the position of the GPS antenna. We therefore decided to conduct a more realistic positional test by mounting the SPAN on one of Sky Research's EM61 towed arrays. "Ground-truth" information was collected by a laser-based positioning system tracking a prism mounted on the rear-left corner of the towed array (one of the corners of the transmitter/reciever). The laser-prism has a lever-arm of close to 1.5 m relative to the SPAN system. Roughly speaking, an error of 1^{o} in orientation will translate to approximately 2.5 cm error in the predicted location of the prism. Therefore, if, for instance, 2.5 cm accuracy were demonstrated, it would place upper bounds of 2.5 cm position and 1^{o} orientation error of the SPAN system. While this test does not have the accuracy and rigor of the RAP test, it does have the potential to estimate the positional and orientation accuracy under realistic data collection conditions.

For the laser-based positioning system we used Trimble's SPS930 Universal Total Station, capable of collecting data at 20 Hz with an accuracy of ±5 mm +2 mm parts per million (ppm). The SPS930 was released in August 2007 and fully characterized as part of SERDP MM-1441 (Foley et al. 2008). It uses Trimble's MultiTrack technology, allowing the instrument to track a passive prism (mirror-only) or active prism (mirrors with an infrared (IR) light source), and Trimble's MagDrive fourth generation servo technology. The MagDrive technology uses magnetic levitation to eliminate friction in the system producing smooth horizontal and vertical angular measurements. The SPS930 uses a 2.4 gigahertz (GHz), 115,200 baud radio to receive data and transmit commands. For this survey, we used an active MT900 prism.

3.1 METHODOLOGY

3.1.1 Test-plan

Figures 14 and 15 show the Sky Research EM61 towed array with the Novatel SPAN system mounted on the tow-bar support and the MT900 active prism on the rear-left corner of the array. Tests were conducted using the following general test-plan

1) Accurately measure the position of the MT900 prism relative to the SPAN. The prism position needs to be determined at sub-centimeter accuracy relative to the SPAN location for this test to be meaningful.
2) SPAN to SPS930 time-alignment: Lift the right-hand side of the array up by 1-2 feet while collecting data with all instruments. Then lift the rear of the array up also while collecting data with all instruments. These tests will allow the time-offset of the SPS930 relative to the SPAN to be determined.
3) "Parking lot" tests: On a smooth surface perform the following tests:
    a. Drive a 50 m long straight line at approximately 0.5 miles per hour (mph) then repeat at 1, 1.5, 2 and 3 mph .
    b. Drive in an S-pattern along the same 50 m section at 0.5, 1, 1.5, 2 and 3 miles per hour.
    c. Put several small "speed bumps" along the path such that only the left wheel will go over them and drive in a straight line at 0.5 and 1 mph (try and do 1.5, 2 and 3 mph if the array and gator can handle the bumps.
    d. Repeat c with the speed bumps on the right-hand wheel.
4) "Rough field" tests: Repeat the tests in 3) on a rough field.

In early June 2008 we made an initial attempt to conduct the tests described above at the FLBGR. Mobilization and equipment rental costs were minimized by conducting the test in conjunction with a test of the Sky Research HeliMag system as part of ESTCP MM-0741. The SPAN data were logged on an internal flash-card on the SPAN receiver and there was no formal integration of the SPAN and DAS. A second GPS receiver on the towed-array was used to provide the timing synchronization pulse to the DAS. The test was essentially a total failure: the SPAN kept rebooting due to a faulty power-connector and the problem went undetected by the operator as no information on the state of the SPAN was displayed in the software controlling the DAS. The project team had to demobilize before the power-problem could be remedied. We decided to tightly integrate the SPAN into the DAS before attempting another test.

Figure 14: Sky Research EM61 towed array with GPS receiver (point 81), HG1700 IMU (points 4 and 9) and MT900 prism (point 132). The numbers delineate reference points used to define the precise geometry of the array through analysis of multiple photographs taken from different positions.

Figure 15: The new Trimble SPS930 (left) uses radio modems to send commands and positions data to and from a portable controller while tracking the prism on the bottom corner of the towed array.

3.1.2 System integration

To prevent a repeat of the system failure experienced during the first test at FLBGR, the SPAN was tightly integrated into the DAS. This system integration task required the following:

- Characterize the reason for frequent resets of the SPAN: The SPAN would over load the serial port when streaming data to the SPAN's COM1 while using the Novatel control and display unit (CDU) executable. The Novatel CDU executable was initially used in order to configure and send commands to the SPAN. Hyperterminal was finally used instead to mitigate the overhead and resulting overload of the SPAN COM port of using CDU. Additionally, a SPAN power supply interface was loose and caused intermittent resetting. This interface was removed and replaced with a direct connection to the 12V battery.
- Characterize why the current SPAN configuration changed dynamically and seemingly randomly: when using the Novatel CDU and exiting, the SPAN would be left configured differently than just prior to using the Novatel CDU. After switching to Hyperterminal for command and control this problem was mitigated.
- Characterize why the SPAN lost the stored configuration in non-volatile memory: The SPAN would frequently loose its stored configuration. The root cause was a bad cable between the SPAN and the IMU. When this cable was rebuilt the SPAN maintained the configuration in non-volatile memory.
- A sequence of SPAN commands had to be derived for our deployment needs resulting in the following script:

```
FRESET
COM COM1 115200 N 8 1 OFF
INTERFACEMODE AUX IMU IMU OFF
COM COM2 38400 N 8 1 OFF
INTERFACEMODE COM2 CMR NONE
SETIMUTYPE IMU_HG1700_AG11
SETIMUORIENTATION 5
VEHICLEBODYROTATION 0 0 0
SAVECONFIG
GROUP CLEAR
GROUP ADD POWERUP
GROUPLOG ADD POWERUP COM1 INSPVAB ONTIME 1
GROUPLOG ADD POWERUP COM1 BESTPOSB ONTIME 1
GROUPLOG ADD POWERUP FILE RAWEPHEMB ONCHANGED 0
GROUPLOG ADD POWERUP FILE RANGECMPB ONTIME .1
GROUPLOG ADD POWERUP FILE RAWIMUSB ONNEW
GROUPLOG ADD POWERUP FILE INSPVASB ONTIME 1
GROUPLOG ADD POWERUP FILE BESTPOSB ONTIME 1
GROUPUSE START POWERUP
```

- A pulse-per-second (PPS) interface had to be created to condition the PPS signal from the SPAN's input/output (I/O) port so that it was compatible with the DAS.
- The second PPS port on one of our DAS units was modified to be compatible with the external PPS conditioning circuit.

- Software processing modules were written that would remove the timestamps and stitch the binary blocks together and maintain byte alignment.
- Various SPAN/IMU states were exposed to the operator by extracting values from the SPAN binary stream (Figure 16).

Figure 16: Partial screen shot of the DAS user-interface showing the SPAN system status.

- In order to collect quality data with the SPAN, requirements and constraints were discovered that must be met:
  - A sufficient number of satellite views for a good GPS solution
  - IMU data to start streaming after a good GPS solution has been met
  - Visual validation that the SPAN COM1 and AUX back panel lights are blinking and the SPAN LCD display is stating "Logging"
  - An IMU alignment to succeed
  - Once the alignment has succeeded, start moving with enough heading and height changes for the IMU to converge, change state, and report INS_SOLUTION_GOOD
  - At this time the vehicle needs to be stationary for at least 2 minutes before the test is initiated and prior to the start of data collection with binary data being written to the SPAN Flash card (this is a requirement from the post processing tool "Inertia Explorer")
  - After the test run has completed and "Close Survey" has been pressed, the vehicle will again have to be stationary for 2 minutes.
- In order to help the operator validate and conform, the DAS Front End was modified with a custom EM61/SPAN configuration selectable from the configuration pull down menu. This included display of the indicators above as well as strip-charts and text-fields of the GPS and IMU data.

3.1.3 Precise measurement of the array geometry

To meaningfully compare the SPAN GPS positions with the SCS930 reported positions requires precise measurement of the geometry of the MT900 prism relative to the GPS antenna phase center. Lever arm measurements were performed on the Sky towed array system by utilizing close range photogrammetry techniques. Photomodeler Scanner, version 6.2.2.596 was used to process the imaging data and generate 3 dimensional (3D) coordinates.

Images of the towed array were taken with a Sony A-200, 10.2 mega pixel, digital single lens reflex (DSLR) camera with an 18mm focal length lens. The A-200 has a field of view crop factor of 1.5, thus the field of view for the digital images is comparable to a 27mm focal length lens if a full frame camera format such as 35mm film was used. The Sony A-200 was calibrated to determine finite values for the focal length, lens distortion,

format aspect ratio, and principal point. The camera is calibrated by taking multiple images of a calibration grid from different perspectives and processed using a calibration routine in the software. The computed finite camera parameters are stored in a calibration file to be used during photo processing. The grid used to calibrate the A-200 camera is shown in Figure 17.

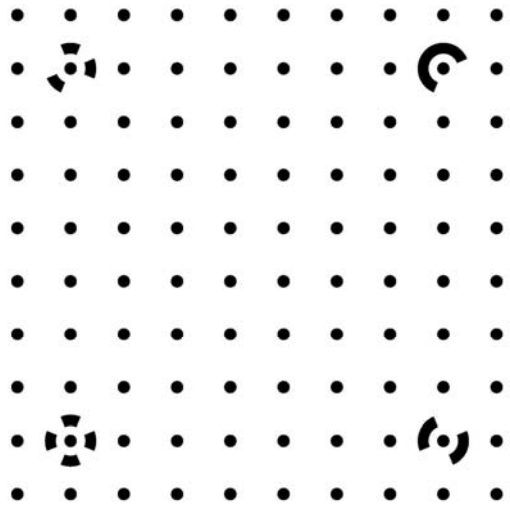

Figure 17: Grid used for calibrating the A-200 camera in the Photomodeler software.

Four images of the towed array were taken and imported into the photomodeler software (Figure 18). The raw images were then idealized using the camera calibration parameters. Idealizing the image removes the effects of lens distortion, non-centered principal point and non-square pixels.

Once the photos have been imported and idealized common points among the photos are selected and used to reference and orient the photos to each other. Figures 14 and 19 show examples of selected reference points on the GPS, IMU and MT900 prism.

After the photos have been referenced to each other they are processed through an image bundle adjustment. Once the bundle adjustment has been successfully computed the camera stations are oriented to the image planes. Figure 20 displays a picture of the solved camera stations and image planes.

From the computed camera stations and image planes a 3D model is generated. Rotation, translation and scale factor parameters are applied to the 3D model to allow for the extraction of physical distances. The scale factor is applied by defining a distance between two reference points in the photos. The left panel of Figure 20 is an image for the 3D model points and solved camera stations.

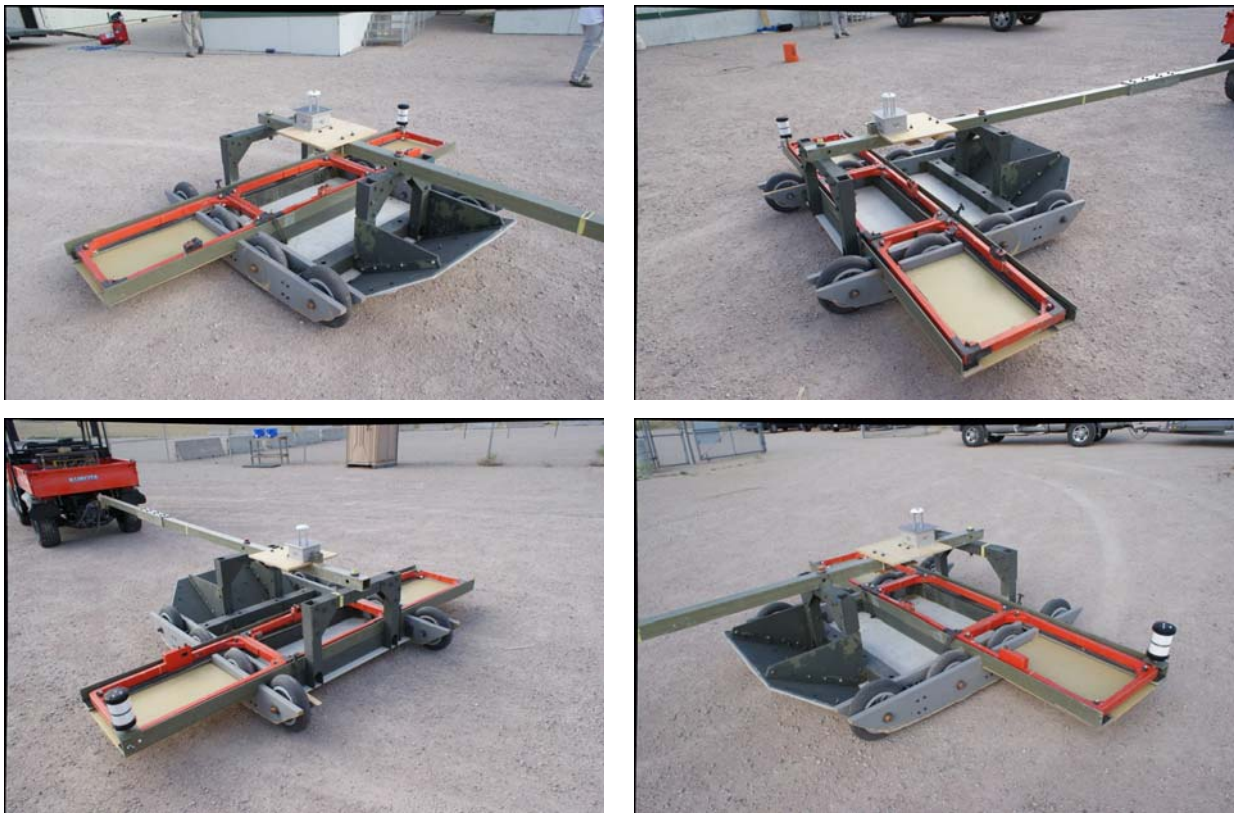

Figure 18: These four photos of the towed array were imported into the photomodeller software.

Figure 19: Example reference points on MT900 prism, GPS and IMU.

The results of the bundle adjustment yielded sub millimeter results, quality statistics of the bundle adjustment are listed below:

Quality Photographs Total Number: 4 Bad Photos: 0 Weak Photos: 0 OK Photos: 4 Number Oriented: 4 Number with inverse camera flags set: 0	Point Marking Residuals Overall RMS: 0.402 pixels Maximum: 1.533 pixels Point 124 on Photo 1 Minimum: 0.061 pixels Point 72 on Photo 4 Maximum RMS: 1.258 pixels Point 124 Minimum RMS: 0.058 pixels Point 72

Cameras Camera1: DSLR-A200 [18.00] Calibration: yes Number of photos using camera: 0 Average Photo Point Coverage: 83% Camera2: DSLR-A200 [18.00] - Idealized Calibration: yes Number of photos using camera: 4 Average Photo Point Coverage: 83%	Point Tightness Maximum: 2.8 mm Point 124 Minimum: 0.082 mm Point 72
Photo Coverage Number of referenced points outside of the Camera's calibrated coverage: 0	Point Precisions Overall RMS Vector Length: 0.817 mm Maximum Vector Length: 1.08 mm Point 41 Minimum Vector Length: 0.653 mm Point 62 Maximum X: 0.761 mm Maximum Y: 0.739 mm Maximum Z: 0.564 mm Minimum X: 0.362 mm Minimum Y: 0.276 mm Minimum Z: 0.302 mm

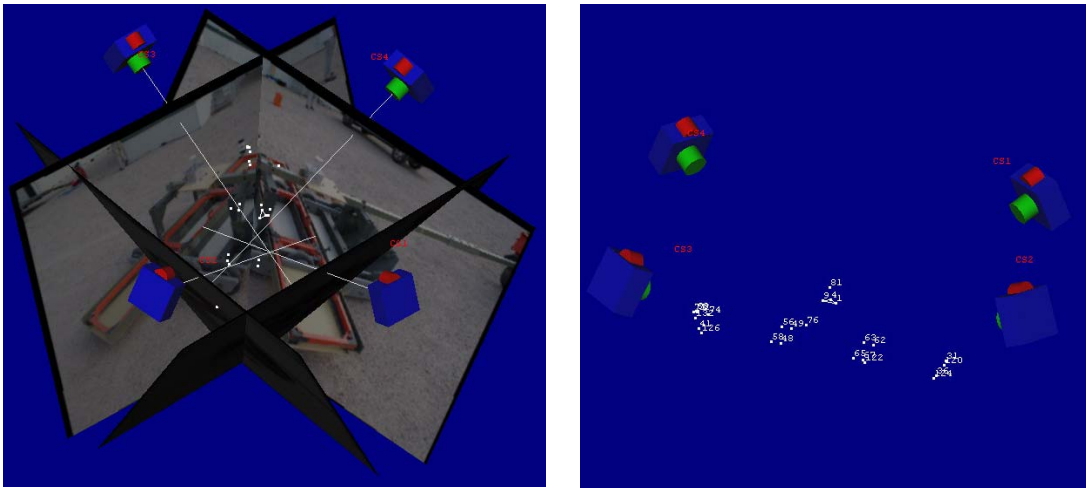

Figure 20: Image planes and camera station solution for the towed-array (left) along with a 3-D model of the points and camera stations (right).

The quality statistics indicate sub millimeter precisions. However, after independently verifying known distances in the 3D model an accuracy of approximately 2mm is expected. This discrepancy can be attributed to the distance that was applied to the photo reference points used to compute the project scale factor. The 3D model was augmented in AutoCAD and center points for the GPS antenna, ATS prism and IMU center were computed from the reference points generated in the photo modeler software. The

geometry of the SPAN IMU and MT900 prism relative to the phase-center of the GPS antenna are given in Table 1.

Position	Left-right offset (cm)	Front-back offset (cm)	Up-down offset (cm)
SPAN IMU	0	0	-16.7
SCS930 prism	-148.3	-40.8	-51.6

Table 1: Position of the IMU and SCS930 prism relative to the GPS receiver in the local coordinate system of the towed-array.

3.2 RESULTS

The SCS930 laser-gun was set-up over Control Point 2 (CP-2, Table 2). The MT900 prism was located over points CP-1 and CP-3 and back-site measurements were taken so that distance and angle measurements from the SCS930 could be converted to UTM, NAD-83 coordinates. The SCS930 orientation was taken as the average of the computed orientations for the CP-1 and CP-3 back-sites. Raw distances measured between the SCS930 and the MT900 prism were corrected for distortions in the UTM grid using a scale factor of 0.999330 (that is the distance measurements were multiplied by this number). The SCS930 was operated at a rate of 10 Hz.

The SPAN GPS corrections came from a permanent GPS base-station on control point Sky-Base2, about 9.0 km from the FLBGR site compound where the experiments were conducted. The GPS data were logged at 20 Hz and the IMU at 100 Hz.

Control Point	Easting (m)	Northing (m)	Elevation (m)
CP-1	527385.316	4385648.348	1800.825
CP-2	527449.999	4385652.390	1802.377
CP-3	527480.617	4385621.359	1805.264
Sky-Base2	536552.830	4385850.456	1814.185

Table 2: Local survey control around the FLBGR site-compound along with the main GPS base station position for the FLBGR site. Positions are given in UTM Zone 13N, NAD-83 (Conus) datum, with the Geiod03 (Conus) geoid.

3.2.1 Position and time-calibrations

The SPAN positions are precisely synchronized to GPS time. A 1 PPS output from the SPAN disciplines the clock in the DAS which allows the arrival of the SCS930 to be time-stamped with an accuracy of 10 μs (actually plus or minus 1 integer second depending on the relative time of arrival of the pulse UTC message). The SCS930 reports its position with a very stable time-lag that appears to vary by less than 4 milliseconds. To accurately compare the SPAN and SCS reported positions we need to precisely determine the latency of the SPS positions relative to GPS time. We lift the rear-left corner of the array in a calibration measurement, and then vary the time-lag of the SCS until it best matches the positions reported by the SPAN (Figure 21). This procedure revealed best fit lags for the different coordinates of -1.07 seconds for easting, -1.039 for

northing and -1.047 for elevation. There was very little movement in the easting so we use the average of the northing and elevation channels to specify a best-fit lag of -1.043 seconds. This lag is used for all the comparisons that follow.

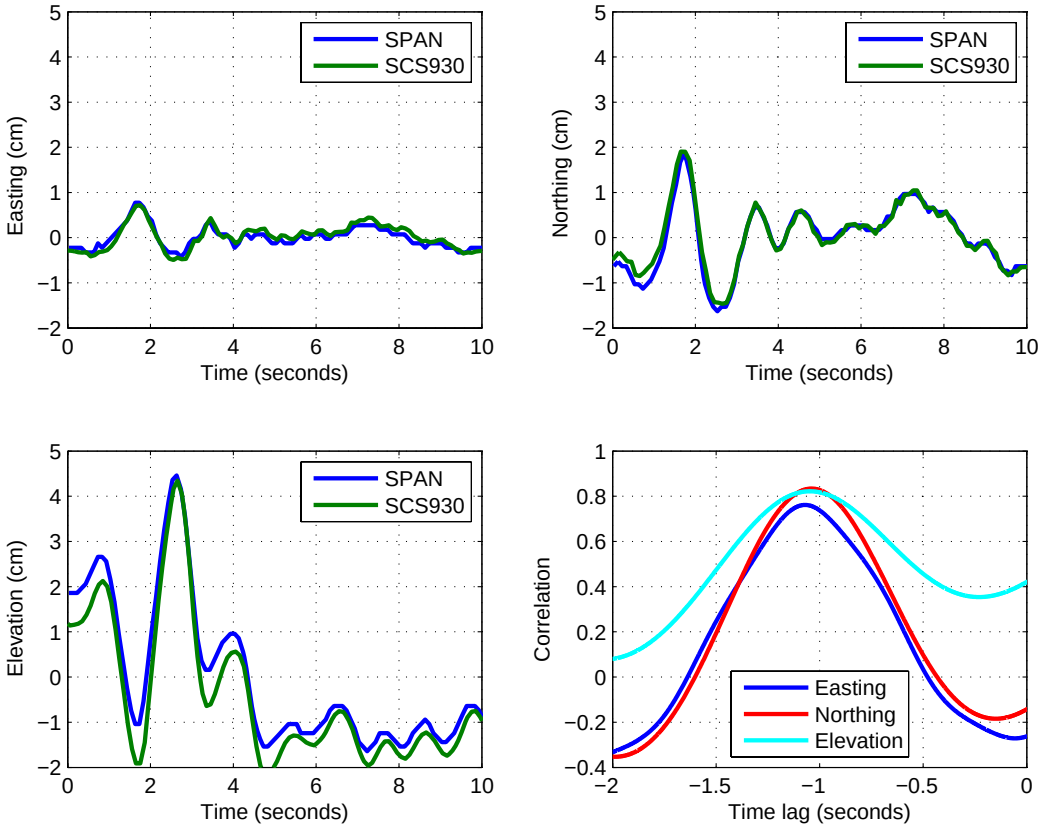

Figure 21: Comparison of SPAN and SCS930 positions during a calibration measurement where the left-hand side of the array is lifted. The SCS930 times are corrected by -1.043 seconds for the comparisons. This time-lag was obtained through cross-correlation of the time-series of the SPAN and SCS930 positions (bottom right plot).

3.2.2 Smooth surface tests

We start by analyzing the data collected while the towed-array traversed a smooth gravel road. There were four different types of tests (Figure 22): (i) driving along a straight line; (ii) driving in an S-pattern; (iii) driving straight with the left-side of the array going over a ramp; and (iv) same as (iii) but with the right-side going over the ramp. Data were collected at speeds of 0.5, 1.0, 1.5, 2.0 and 3.0 mph for each of these four tests.

The SPAN data were post-processed in Inertial Explorer and the position of the MT900 prism was predicted using the offsets measured by the photogrammetry survey (Table 1). The SCS930 position time-base was corrected by the measured time-lag of -1.043 seconds, and the SCS930 positions were interpolated to the same times as the SPAN. The error in the position prediction of the SPAN was then calculated by subtracting the SCS930 measured positions. Immediately, we noticed that there was a bias in the coordinate systems of the SPAN and SCS930 reported positions (Figure 23a). The easting coordinate bias varied from about -1 cm at the most westerly point, to +4 cm at

the most easterly point. The northing and elevation biases were approximately constant with values of +7 cm and -1772 cm respectively (the SPAN and SCS height-datums were different). The bias could result from one or more of the following issues: (i) Offset between the SPAN and SCS930 control points (translation error); (ii) incorrect establishment of the orientation of the SCS930 through the back-site procedure (rotation error); and/or (iii) incorrect scale factor (dilation error). To correct for this coordinate system mismatch, we used all SPAN and SCS930 positions and solved for the affine transformation (combination of translation, rotation and dilation) that produced the best match, in a least-squared sense, between the two coordinate systems. The rotation occurred around the CP-2 control-point. The best-fitting transformation was clockwise rotation of 0.0440^{o}, corrected scale factors of 1.001202 and translation of 3.0 cm East, 9.6 cm North and -1769.5 cm upwards. The affine transformation appears to have removed any bias between the SPAN and SCS930 coordinate systems (Figure 23b).

After applying the affine transformation, we then compared the SPAN predicted position of the MT900 prism against the position measured by the SCS930 for the straight line and S-curve tests (Figure 24) and the left- and right-ramp tests (Figure 25). RMS errors and standard deviations for each of the tests are given in Table 3. For the straight-line path, the total error is generally less than 1 cm, with RMS errors in 3-D position of between 0.78-0.93 cm. Thus, for a smooth, straight-line path, the Novatel SPAN is able to produce errors of less than 1 cm in position and better than 0.4^{o} in error (recall that with the lever-arm, a 1 degree error in orientation results in a 2.5 cm error in position). For the S-bends there is a larger error around the turns, with the errors increasing to closer to 2 cm. Nevertheless, the 3-D RMS errors for this case are between 1.26 and 1.45 cm. When the left-hand side of the array goes over a ramp there is a relatively large elevation change in prism position and a corresponding increase in the positional error (Figure 25a). The elevation errors, in general, appear to have a bias in this run, which may indicate a systematic error in the estimated GPS elevation. Three-dimensional RMS errors approach 3.25 cm, but the horizontal errors are smaller with RMS less than 1.8 cm. By the time the right-hand side ramp test is conducted, any systematic error appears to have disappeared, and the 3-D RMS errors are between 1.5 and 2.5 cm.

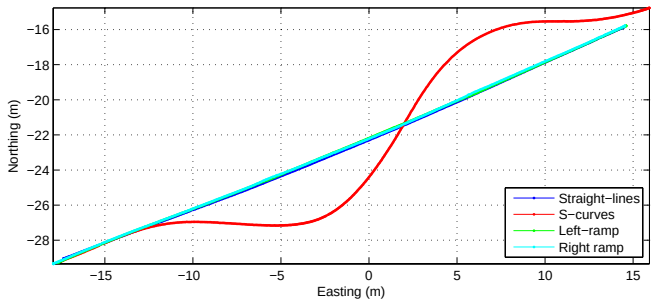

Figure 22: Plan-view (relative to CP-2) of the prism path for the four position tests.

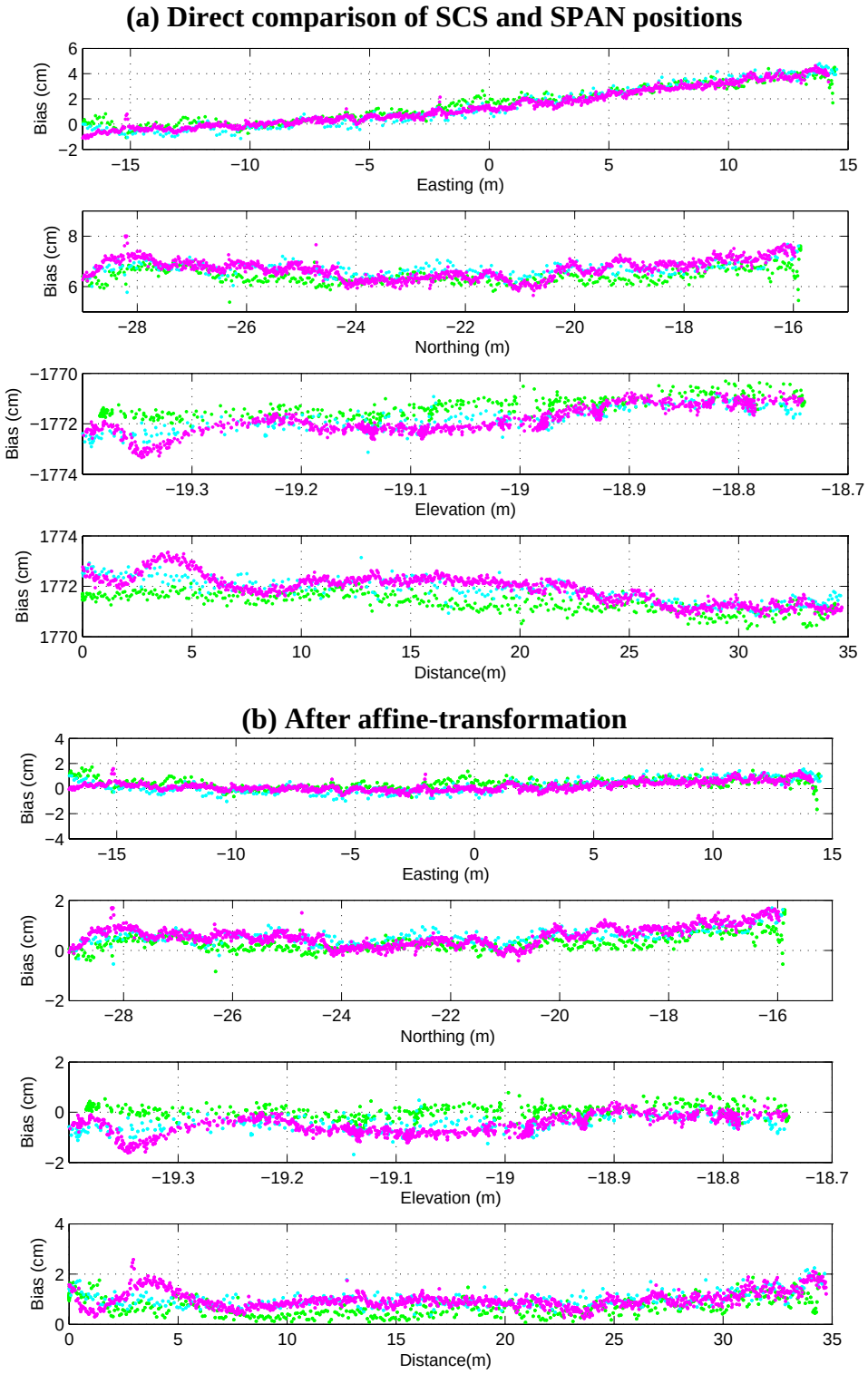

Figure 23: Bias in the SCS930 positions before (a) and after (b) an affine transformation. The different colors represent data collection events with the towed-array traveling at different speeds (blue: 0.5; red: 1.0; green: 1.5; cyan: 2.0; and magenta 3.0 mph).

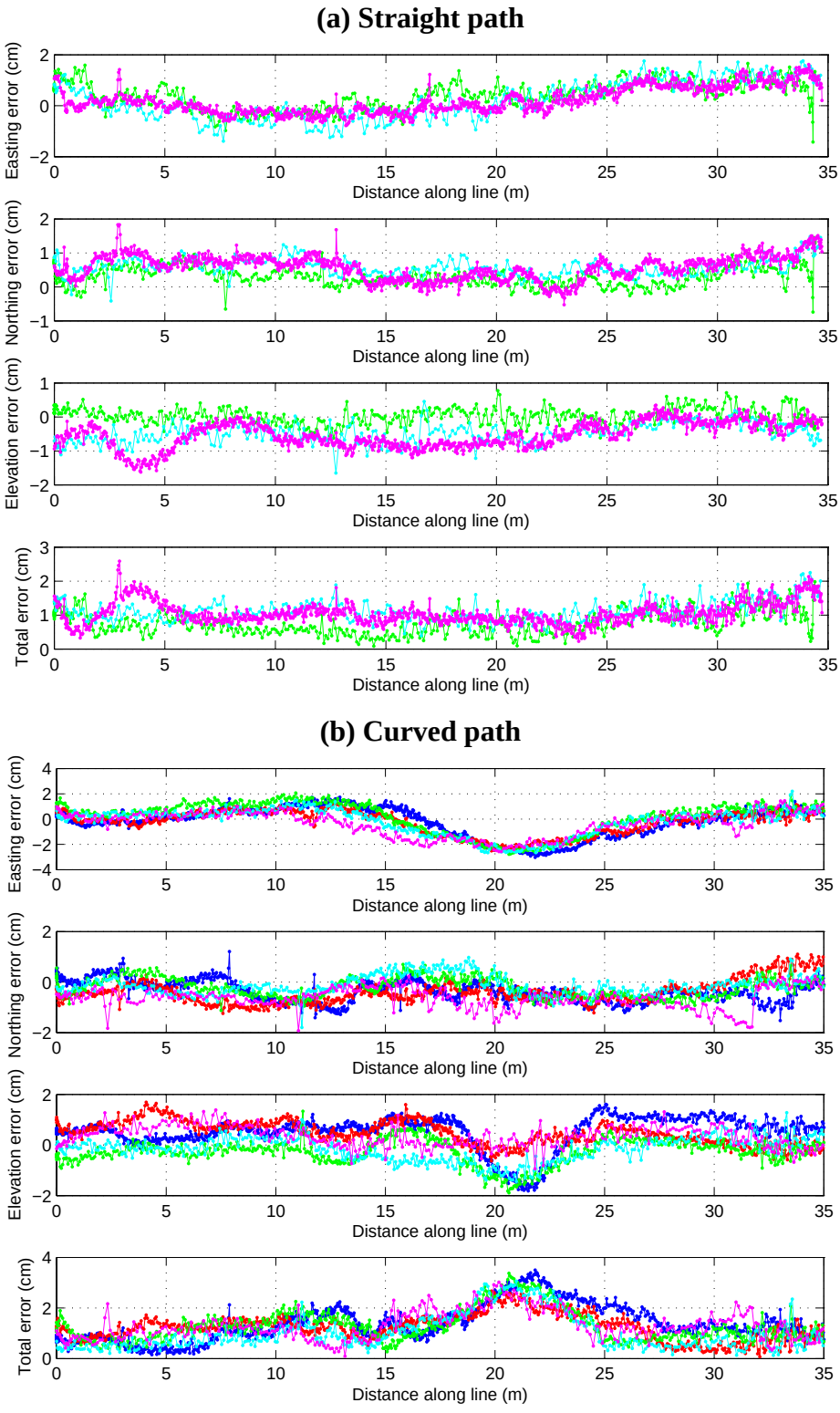

Figure 24: Difference between the SPAN predicted position of the MT900 prism and the SCS930 measured position of the prism when driving: (a) straight; and (b) along an S-curve. Colors are different speeds: blue: 0.5; red: 1.0; green: 1.5; cyan: 2.0; and magenta 3.0 mph.

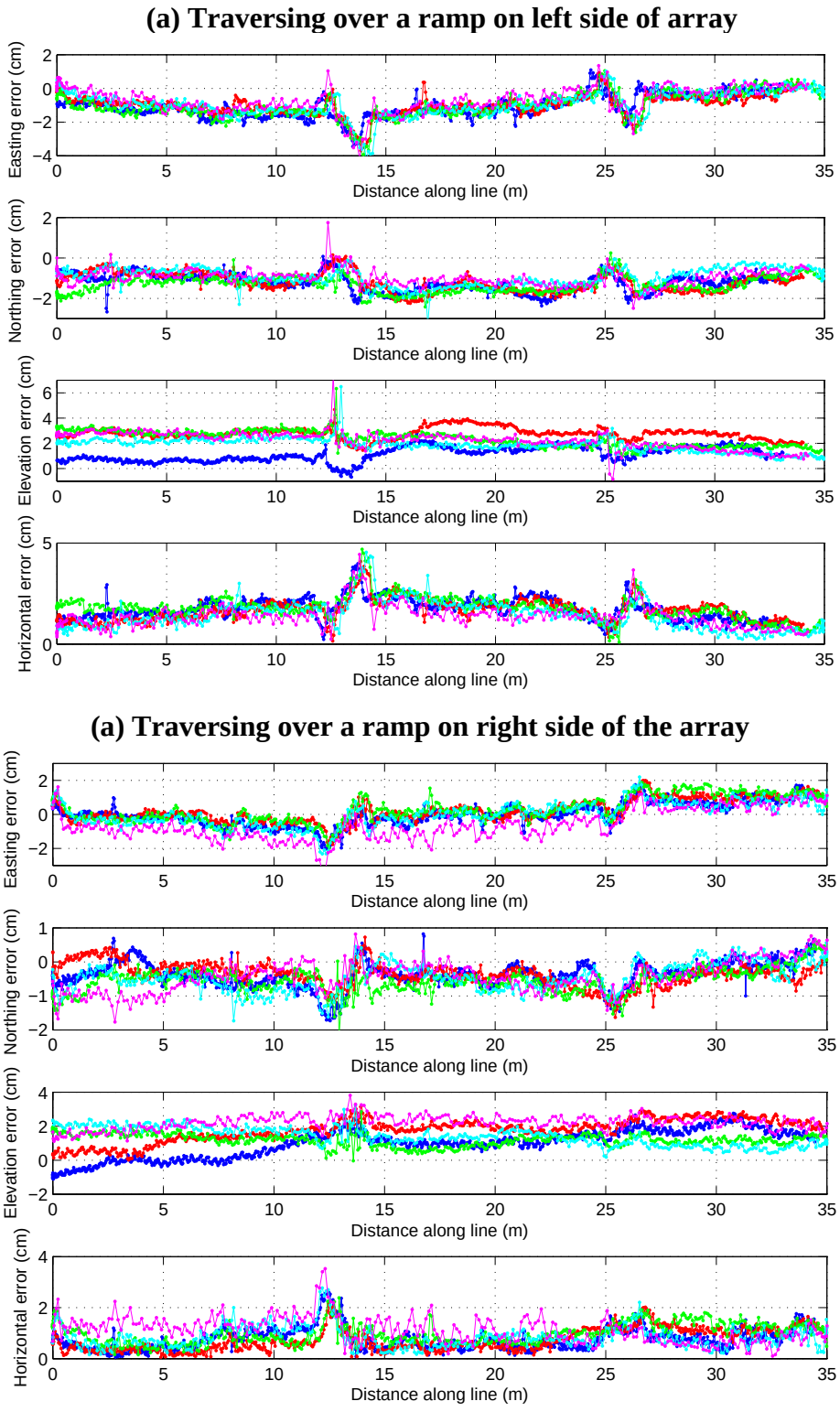

Figure 25: Difference between the SPAN predicted position of the MT900 prism and the SCS930 measured position of the prism when driving over: (a) left-ramp; and (b) right-ramp. Colors are different speeds: blue: 0.5; red: 1.0; green: 1.5; cyan: 2.0; and magenta 3.0 mph.

Statistic	Root mean squared error (cm)				Standard deviation (cm)			
Coordinate	**Easting**	**Northing**	**Elevation**	**Total**	**Easting**	**Northing**	**Elevation**	**Total**
Straight line	**0.57**	**0.60**	**0.49**	**0.84**	**0.47**	**0.35**	**0.31**	**0.41**
0.22 m/s (0.5 mph)	0.43	0.69	0.65	0.81	0.37	0.38	0.38	0.42
0.9 m/s (2 mph)	0.64	0.45	0.25	0.78	0.45	0.33	0.25	0.42
1.3 m/s (3 mph)	0.64	0.67	0.57	0.93	0.58	0.32	0.30	0.39
S-bends	**1.22**	**0.58**	**0.61**	**1.36**	**1.20**	**0.47**	**0.50**	**0.66**
0.22 m/s (0.5 mph)	1.30	0.56	0.81	1.42	1.28	0.47	0.65	0.81
0.45 m/s (1 mph)	1.11	0.59	0.66	1.25	1.08	0.43	0.46	0.59
0.67 m/s (1.5 mph)	1.36	0.49	0.57	1.45	1.36	0.47	0.50	0.60
0.9 m/s (2 mph)	1.16	0.48	0.52	1.26	1.15	0.47	0.50	0.68
1.3 m/s (3 mph)	1.17	0.79	0.51	1.41	1.14	0.53	0.41	0.61
Ramp on left	**1.01**	**1.26**	**2.17**	**2.73**	**0.57**	**0.43**	**0.59**	**0.62**
0.22 m/s (0.5 mph)	1.11	1.35	1.29	2.18	0.53	0.41	0.60	0.53
0.45 m/s (1 mph)	1.00	1.31	2.80	3.25	0.47	0.41	0.48	0.48
0.67 m/s (1.5 mph)	1.08	1.45	2.45	3.04	0.59	0.43	0.62	0.70
0.9 m/s (2 mph)	1.01	1.09	1.93	2.44	0.61	0.49	0.54	0.69
1.3 m/s (3 mph)	0.84	1.09	2.37	2.73	0.63	0.40	0.72	0.72
Ramp on right	**0.66**	**0.62**	**1.64**	**1.89**	**0.62**	**0.46**	**0.57**	**0.52**
0.22 m/s (0.5 mph)	0.53	0.58	1.29	1.51	0.53	0.45	0.87	0.62
0.45 m/s (1 mph)	0.53	0.46	1.91	2.03	0.49	0.31	0.67	0.68
0.67 m/s (1.5 mph)	0.70	0.72	1.27	1.62	0.59	0.44	0.37	0.36
0.9 m/s (2 mph)	0.60	0.67	1.50	1.75	0.59	0.51	0.53	0.56
1.3 m/s (3 mph)	0.96	0.69	2.23	2.52	0.88	0.61	0.40	0.38

Table 3: Root mean-squared errors and standard deviation for various tests on the smooth surface.

3.2.3 Rough surface tests

We repeated the smooth-road tests on an adjacent field where the towed array suffered larger changes in orientation and elevation. The tests were conducted on the second day of mobilization and utilized a new set-up of the SCS930 base-station. An affine transformation was again required to remove any positional biases. Best fitting parameters were clockwise rotation of 0.0853^{o}, corrected scale factors of 1.00225 and translation of 3.9 cm East, 6.0 cm North and -1771.0 cm upwards. The results of the rough-surface tests (Figures 26 and 27, Table 4) are similar to those of the smooth surface tests. Several of the datasets display biases on the 1 to 2 cm level on the reported elevations. RMS errors on the straight-line were 0.8 cm on the smooth surface and 1.5 cm on the rough surface, for the S-curves RMS errors were 1.4 cm on both surfaces, for the left ramp the RMS errors were 2.7 cm and 2.3 cm and for the right ramp they were 1.9 cm and 1.5 cm respectively. Much of the differences in the smooth and rough-road scenarios were in the different biases in the elevation angles. Amongst all the tests (smooth and rough road, different speed, straight, s-bend, ramps etc) the RMS horizontal error varied from a minimum of 0.6 cm to a maximum of 1.7 cm. These represent upper bounds on the horizontal positional error of the SPAN system. If the error was entirely due to an error in the SPAN heading, the RMS heading error would vary from a minimum of 0.2^{o} to a maximum of 0.6^{o}. These results are remarkable given that the SCS930 measured positions are on the order of 0.5 cm.

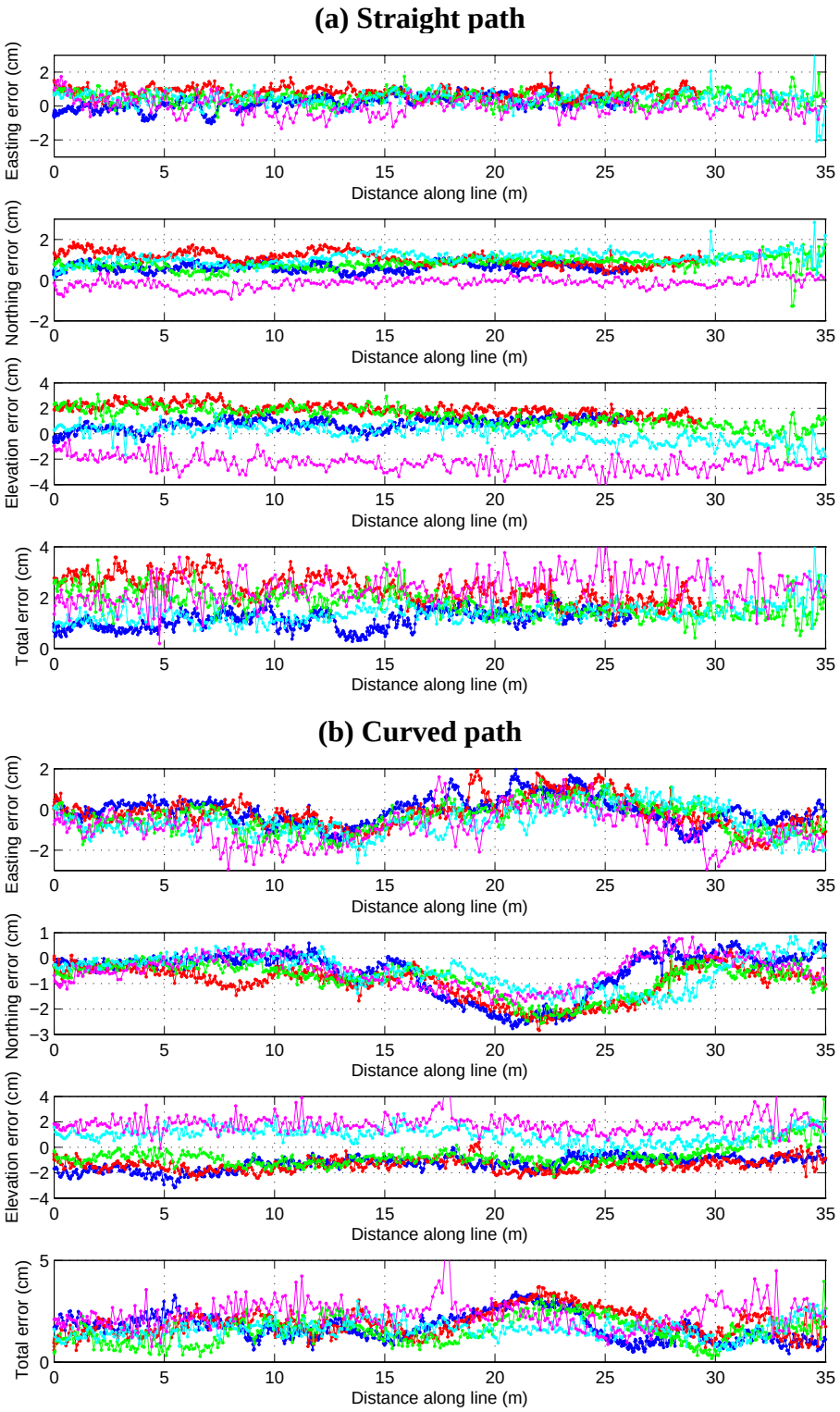

Figure 26: For the rough field tests, the difference between the SPAN predicted position of the MT900 prism and the SCS930 measured position of the prism when driving: (a) straight; and (b) along an S-curve. Colors are different speeds: blue: 0.5; red: 1.0; green: 1.5; cyan: 2.0; and magenta 3.0 mph

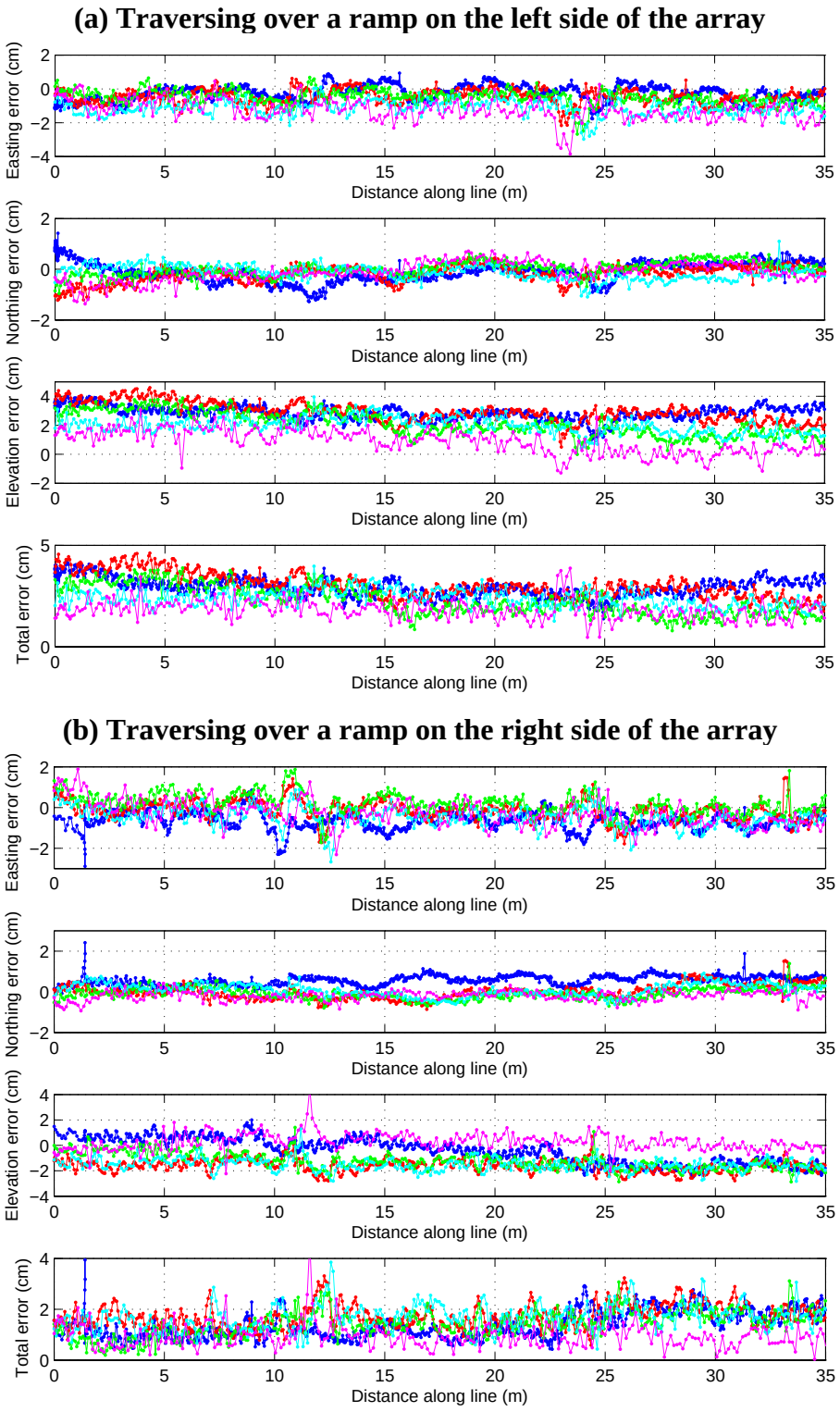

Figure 27: For the rough field tests, the difference between the SPAN predicted position of the MT900 prism and the SCS930 measured position of the prism when driving over: (a) left-ramp; and (b) right ramp. Colors are different speeds: blue: 0.5; red: 1.0; green: 1.5; cyan: 2.0; and magenta 3.0 mph

Statistic	Root mean squared error (cm)				Standard deviation (cm)			
Coordinate	**Easting**	**Northing**	**Elevation**	**Total**	**Easting**	**Northing**	**Elevation**	**Total**
Straight line	**0.61**	**0.82**	**1.49**	**1.88**	**0.41**	**0.28**	**0.61**	**0.48**
0.22 m/s (0.5 mph)	0.45	0.67	0.89	1.20	0.40	0.20	0.49	0.36
0.45 m/s (1 mph)	0.86	1.12	1.94	2.40	0.31	0.32	0.46	0.52
0.67 m/s (1.5 mph)	0.60	0.87	1.53	1.86	0.36	0.30	0.73	0.49
0.9 m/s (2 mph)	0.60	1.13	0.72	1.47	0.44	0.31	0.72	0.39
1.3 m/s (3 mph)	0.54	0.31	2.38	2.46	0.54	0.28	0.65	0.61
S-bends	**0.90**	**0.95**	**1.37**	**1.92**	**0.73**	**0.71**	**0.61**	**0.61**
0.22 m/s (0.5 mph)	0.67	1.03	1.34	1.81	0.66	0.89	0.51	0.66
0.45 m/s (1 mph)	0.78	1.14	1.49	2.03	0.75	0.68	0.48	0.62
0.67 m/s (1.5 mph)	0.81	1.00	0.99	1.63	0.69	0.63	0.77	0.64
0.9 m/s (2 mph)	0.98	0.79	1.16	1.71	0.72	0.63	0.61	0.44
1.3 m/s (3 mph)	1.27	0.81	1.87	2.41	0.83	0.71	0.68	0.66
Ramp on left	**0.92**	**0.37**	**2.26**	**2.54**	**0.50**	**0.36**	**0.69**	**0.55**
0.22 m/s (0.5 mph)	0.60	0.46	2.97	3.07	0.48	0.46	0.49	0.48
0.45 m/s (1 mph)	0.63	0.37	2.97	3.06	0.42	0.33	0.70	0.65
0.67 m/s (1.5 mph)	0.69	0.27	2.18	2.31	0.45	0.27	0.84	0.72
0.9 m/s (2 mph)	1.27	0.33	1.99	2.38	0.48	0.31	0.59	0.43
1.3 m/s (3 mph)	1.42	0.42	1.20	1.90	0.67	0.41	0.82	0.50
Ramp on right	**0.63**	**0.40**	**1.34**	**1.56**	**0.50**	**0.30**	**0.66**	**0.50**
0.22 m/s (0.5 mph)	0.79	0.64	1.12	1.51	0.43	0.26	1.00	0.54
0.45 m/s (1 mph)	0.50	0.42	1.76	1.87	0.47	0.41	0.49	0.49
0.67 m/s (1.5 mph)	0.52	0.31	1.50	1.61	0.51	0.30	0.64	0.52
0.9 m/s (2 mph)	0.66	0.32	1.64	1.80	0.47	0.30	0.50	0.51
1.3 m/s (3 mph)	0.68	0.33	0.69	1.02	0.62	0.25	0.65	0.47

Table 4: Root mean-squared errors and standard deviation for various tests on the rough surface.

4 SIMULATIONS OF TEM SYSTEMS

In this section of the report we describe numerical evaluation of different candidate sensor systems designed for one-pass detection and discrimination. We conducted the assessment using both semi-analytic methods (e.g., system spatial resolution, model uncertainty) and monte-carlo based simulations. The semi-analytic techniques provide powerful metrics to assess the expected performance of different systems, but do not easily allow positional uncertainties to be incorporated. On the other-hand, the monte-carlo simulations can incorporate all types of errors (including positional and orientation uncertainty) but the results can be difficult to interpret and don't always support unambiguous conclusions.

4.1 CANDIDATE SENSOR SYSTEMS AND ASSESSMENT PLAN

All of the candidate sensor systems are time-domain system with equivalent measurement characteristics to the TEMTADS. This system records the time-decay in a user-configuration number of time-channels between 40 μ s and 25 ms after pulse turn-off. ESTCP Project MM0601 is using that system as the basis for a cued-interrogation mode sensor that would collect data while stationary over a suspected ordnance item. We assume the time-gates have been configured to be equivalent to the EM-63 with 26 logarithmically spaced time-gates between 180 μs and 25 ms after pulse turn-off. We consider three different array configurations and two cart-based configurations. The array-based systems are:

1) Cued-interrogation array: The TEMTADS array with 25 transmitters and receivers deployed in a static mode (this will define the base-line performance). The array is centered over an estimated target location, and then transmitter 1 is fired several times with all receivers measuring the secondary field. Next transmitter 2 is fired with all receivers measuring the data, and so-forth until all 25 transmitters have been fired. Figure 28 (a) is a schematic view of 25 transmitters (red)/receivers (blue), where each loop has the size of 0.4 m $\times 0.4$ m and the receiver loops are plotted slightly smaller for clear display.
2) Modification of MTADS cued-interrogation array to conduct one-pass detection and discrimination by replacing the 25 transmitters with a single 2 m by 2 m transmitter (but keeping the 25 receivers). This modified system is shown in Figure 28 (b). We will refer to this system as "Single-Tx/25-Rx";
3) As per 2) but with four 1 m by 1 m transmitters that are fired sequentially as the array transverses over an area, as shown in 28 (c). We will refer to this system as "Four-Tx/25-Rx".

These two modifications to the cued MTADS array represent feasible changes to the system that could be easily implemented.

We consider two cart systems:

1) Geonics EM-63 equivalent system: with a 0.5 m by 0.5 m receiver coil and a 1 m by 1 m transmitter.

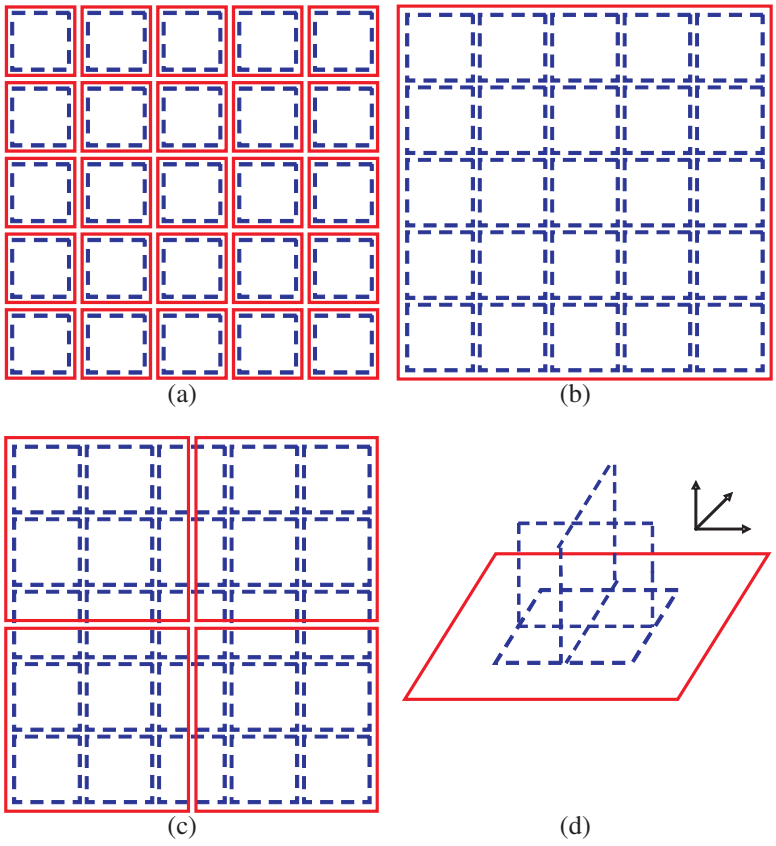

Figure 28: Schematic views of arrays in candidate sensor systems. The loop in red represents a transmitter, in blue a receiver. (a) The cued-interrogation array of 25 transmitters /receivers. Each loop is 0.4 m $\times$0.4 m. (b) The array of single-Tx (2 m $\times$2 m)/25-Rx. (c) Four-Tx/25-Rx, transmitter: 1 m $\times$ 1 m; receiver: 0.4 m $\times$0.4 m. (d) EM63-M: transmitter of 1 m $\times$ 1 m. Multi-component receivers: 0.5 m $\times$ 0.5 m.

2) Modification of the EM-63 equivalent to include horizontal component receivers as shown in 28 (d). We refer to this modified system as "EM63-M", where M indicates a multi-component receiver.

The EM-63 equivalent will provide a performance base-line of the "last generation" of EMI sensors. The horizontal coil receiver configurations are representative of next-generation systems that could feasibly be deployed in a one-pass detection and discrimination mode.

4.2 SEMI-ANALYTICAL APPROACH

A transient EM (TEM) system assumed in this study is distributed in a plane above the surface to interrogate a buried object. When the target dimension is smaller than the target-senor distance, it is known that the low frequency EMI scattering from the metallic target can be well described by an equivalent induced dipole (Bell., 2005; Das et al., 1990; Smith et al.,

2004) characterized by a 3×3 magnetic polarizability tensor

$$P(t) = \begin{bmatrix} p_{11}(t) & p_{12}(t) & p_{13}(t) \\ p_{21}(t) & p_{22}(t) & p_{23}(t) \\ p_{31}(t) & p_{32}(t) & p_{33}(t) \end{bmatrix}. \tag{6}$$

The elements of the tensor $p_{ij}(t)$ represent a dipole component in the ith Cartesian direction due to a primary field in the jth Cartesian direction and $p_{ij} = p_{ji}$. The equivalent dipole polarizability tensor $P(t)$ contains information regarding the geometry and material properties of a target as well as its orientation.

For the n-th measurement in a survey, the secondary response d_n at time instant t to an equivalent dipole source $P(t)$ located at $\mathbf{r}$ can be written as (Das et al., 1990)

$$d_n(\mathbf{r}_{Rx_n}, t) = \mathbf{H}_R^T(\mathbf{r}, \mathbf{r}_{Rx_n}) P(t) \mathbf{H}_T(\mathbf{r}, \mathbf{r}_{Tx_n}), \tag{7}$$

where $\mathbf{H}_R(\mathbf{r}, \mathbf{r}_{Rx_n}) = [H_R^x \; H_R^y \; H_R^z]^T$ and $\mathbf{H}_T(\mathbf{r}, \mathbf{r}_{Tx_n}) = [H_T^x \; H_T^y \; H_T^z]^T$ are the magnetic fields at the object location $\mathbf{r}$ generated by the receiver and transmitter coils with their centers at $\mathbf{r}_{Rx_n}$ and $\mathbf{r}_{Tx_n}$, and the superscripts x, y, and z denote the Cartesian components of a field and the superscript T denotes a transpose. The magnetic fields are computed via line integrals along each of the coils (Das et al., 1990). Equation (7) describes the basic EMI process of illuminating, scattering and sensing and can be rearranged in another scalar-product form as

$$d_n(\mathbf{r}_{Rx_n}, t) = \mathbf{a}_n^T(\mathbf{r}, \mathbf{r}_{Rx_n}, \mathbf{r}_{Tx_n}) \mathbf{q}(t), \tag{8}$$

where $\mathbf{a}_n(\mathbf{r}, \mathbf{r}_{Rx_n}, \mathbf{r}_{Tx_n})$ is a 6×1 column vector representing spatial sensitivities of the n-th pair of transmitters-receivers to the object located at $\mathbf{r}$, and $\mathbf{q}(t)$ a 6×1 column vector whose components are the elements of the polarizability tensor $P(t)$ of the object:

$$\mathbf{a}_n(\mathbf{r}, \mathbf{r}_{Rx_n}, \mathbf{r}_{Tx_n}) = \begin{bmatrix} H_R^x H_T^x \\ H_R^x H_T^y + H_R^y H_T^x \\ H_R^x H_T^z + H_R^z H_T^x \\ H_R^y H_T^y \\ H_R^y H_T^z + H_R^z H_T^y \\ H_R^z H_T^z \end{bmatrix}, \mathbf{q}(t) = \begin{bmatrix} p_{11}(t) \\ p_{12}(t) \\ p_{13}(t) \\ p_{22}(t) \\ p_{23}(t) \\ p_{33}(t) \end{bmatrix}. \tag{9}$$

With a total of N measurements the data and model parameter relationship can be conveniently expressed in vector-matrix notation as follows,

$$\mathbf{d}(t) = A(\mathbf{r}, \mathbf{r}_s) \mathbf{q}(t) + \mathbf{n}(t), \tag{10}$$

where $\mathbf{d}(t) = [d_1(t), \cdots, d_N(t)]^T$ is $N \times 1$ measured data vector at time instant t, $\mathbf{n}(t)$ the corresponding $N \times 1$ additive noise vector, and $A(\mathbf{r}, \mathbf{r}_s)$ is a $N \times 6$ matrix denoting the sensitivities of the N sensors to the object located at $\mathbf{r}$,

$$A(\mathbf{r}, \mathbf{r}_s) = \begin{bmatrix} \mathbf{a}_1^T(\mathbf{r}, \mathbf{r}_s) \\ \vdots \\ \mathbf{a}_N^T(\mathbf{r}, \mathbf{r}_s) \end{bmatrix},$$

and we simply condense $\mathbf{r}_{\rm s} = [\mathbf{r}_{Rx_n}, \mathbf{r}_{Tx_n}]$ to represent a transmitter-receiver configuration. Note that generally $N = N_s \times N_T \times N_R$, where N_s denotes the number of survey locations, N_T and N_R the numbers of transmitters and receivers designed in a sensor system. Equation (10) is the underlying physical model used for semi-analytical assessment of a sensor system.

4.2.1 Linear least-squares solution

Consider an EMI survey that collects data with a specific sensor system above the surface to interrogate a buried object. The objective of the survey is to estimate the target polarization and location from the measured data through the relationship defined in (10). For the semi-analytical approach, we consider the response of a single-time channel data. Thus at time t, the unknown model vector, $\mathbf{m}$, is given by

$$\mathbf{m} = \left[\begin{array}{c} \mathbf{r} \\ \mathbf{q} \end{array} \right], \tag{11}$$

where $\mathbf{r}$ is a location vector of an object and $\mathbf{q}$ is composed of 6 polarizabilities at time-channel t as given in Equation (9). To simplify notation we will stop referring to the explicit dependance on the time t. The inverse problem is nonlinear because of the unknown object location and its coupling with the unknown dipolar polarization, although the latter is linearly related to the measured data, as observed in Equation (10).

For a nonlinear problem, the observations $\mathbf{d}_{\rm obs}$ can be generally expressed as

$$\mathbf{d}_{\rm obs} = \mathcal{F}[\mathbf{m}] + \mathbf{n}, \tag{12}$$

where $\mathcal{F}$ denotes a forward functional operator and $\mathcal{F}[\mathbf{m}]$ represents the theoretical data which are computed using the forward model. The inverse problem can be stated as finding a model $\mathbf{m}$ that can best explain the observations in a least-squares sense, i.e., minimize the following weighted misfit,

$$\phi_d = ||W_d(\mathbf{d}_{\rm obs} - \mathcal{F}[\mathbf{m}])||^2, \tag{13}$$

where W_d is a weighting matrix (that is usually related to the inverse covariance matrix of the data).

To make the nonlinear problem tractable, we adopt the standard approach and linearize the problem by expanding the misfit function as a Taylors series in the vicinity of some model $\mathbf{m}_0$. We retain only first-order terms so that

$$\mathcal{F}[\mathbf{m}] \approx \mathcal{F}[\mathbf{m}_0] + J\Delta\mathbf{m}, \tag{14}$$

where $\Delta\mathbf{m} = \mathbf{m} - \mathbf{m}_0$ is a model correction vector and J is $N \times M$ the Jacobian matrix comprising the partial derivatives of the data functional evaluated at the current model,

$$J = \frac{\partial \mathcal{F}}{\partial \mathbf{m}} \mid_{\mathbf{m}_0}, \tag{15}$$

where M is the number of unknowns which is 9 in our case. By inserting equation (14) into equation (13), we obtain a linearized approximation to the misfit function,

$$\phi_d = ||W_d(\Delta\mathbf{d} - J\Delta\mathbf{m})||^2, \tag{16}$$

where $\Delta\mathbf{d} = \mathbf{d}_{\text{obs}} - \mathcal{F}[\mathbf{m}_0]$ are the data residuals between the measured data and the predicted ones at the current model $\mathbf{m}_0$. Equations. (14) through (16) define a linearized problem. By minimizing Equation (16), we obtain the weighted least-squares solution to the model correction vector (Menke, 1989; Tarantola, 1987) at one step

$$\Delta\mathbf{m} = (J^T W_d^T W_d J)^{-1} J^T W_d^T W_d \Delta\mathbf{d}. \tag{17}$$

In most cases, the matrix $W_d^T W_d$ in Equation (17) can be chosen as the inverse of the covariance matrix C_d of data errors (if it can be estimated). Using the notation of $W_d^T W_d = C_d^{-1}$, Equation (17) can be simplified slightly as

$$\Delta\mathbf{m} = (J^T C_d^{-1} J)^{-1} J^T C_d^{-1} \Delta\mathbf{d}. \tag{18}$$

This is a general formal solution to a linear or linearized problem. If errors are independent, C_d is a diagonal matrix and if the variance of each observation is also the same, then each diagonal element of C_d will be equal to the variance. For a nonlinear inverse problem, the linearization procedure in Equations (17) or (18) may be applied iteratively to attain the optimal estimate of the model parameters.

4.2.2 Solution uncertainty

Uncertainty in the estimated model parameters can be assessed in terms of the model covariance matrix (Menke, 1989; Tarantola, 1987). Denote J^+ as the generalized inverse in Equation (18), i.e., $J^+ = (J^T C_d^{-1} J)^{-1} J^T C_d^{-1}$. The model covariance matrix C_m can be written as (Menke, 1989; Tarantola, 1987)

$$C_m = J^+ C_d J^{+T} = (J^T C_d^{-1} J)^{-1} \tag{19}$$

and assuming each measurement is contaminated by Gaussian white-noise with variance σ_d^2, then $C_d = \sigma_d^2 I$, and

$$C_m = \sigma_d^2 (J^T J)^{-1}. \tag{20}$$

The model parameter covariance matrix depends upon the uncertainty in the data as well as the data kernel J which contains the sensitivities of the data functional with respect to the source location and polarizability. Thus C_m can be used to quantify the capability of a sensor system to accurately determine the polarization tensor and location parameter. The diagonal elements of C_m contain the variance of each model parameter; while the non-diagonal elements describes the correlation between parameters if the matrix is normalized. The sum of the diagonal terms of the covariance matrix can be used as a single measure of the quality

of a given survey. For example, Liao and Carin (2004) used the trace of the inverse of the Fisher Information Matrix (FIM) as a measure of survey quality in the development of an adaptive framework for optimal EMI surveying for UXO characterization. The inverse of the FIM, is known as the Hessian in the signal processing community and is equivalent to the model covariance matrix. In the linearized problem considered here, $J^T C_d^{-1} J$ in (19) is a Jacobian-based approximation to the Hessian, which is often used when solving least-squares problems (e.g. Menke, 1989).

Since we have two types of unknown parameters (the object location and its polarizability), we derive two measures of uncertainty as follows. Partition the covariance matrix of C_m into

$$C_m = \begin{pmatrix} C_r & \cdots \\ \cdots & C_p \end{pmatrix}, \tag{21}$$

where C_r and C_p are block matrices of size 3×3 and 6×6, i.e., the covariance matrices corresponding to the parameters of the source location and polarizability. We could then, for instance, define the total squared uncertainty of the polarizabilitties as

$$\epsilon_p = \sum_4^9 (C_m)_{ii} = \mathrm{Tr}(C_p). \tag{22}$$

This is the metric that was used by Smith et al. (2004) to assess the relative merits of different transmitter/receiver combinations in resolving equivalent dipole polarizabilities.

To accurately estimate the polarizability parameters, requires a well determined estimate of the source location $\mathbf{r}_0$. For the two sub-covariance matrices of C_r and C_p, we can derive analytical expressions to determine the connection between the different parameters. Without loss of generality, set $C_d = I$, the identity matrix (we can readmit the weighting matrix at the end). Divide the Jacobian matrix into $J = [D\ A]$, where sub-matrices D and A express the sensitivities to the location and polarizabilty of an object, respectively. We can then expand the LS normal equations to the solution (18) as

$$\begin{aligned} D^T \Delta\mathbf{d} &= D^T D \Delta\mathbf{r} + D^T A \Delta\mathbf{q} \\ A^T \Delta\mathbf{d} &= A^T D \Delta\mathbf{r} + A^T A \Delta\mathbf{q} \end{aligned}. \tag{23}$$

Consequently, the linearized solution of Equation (23) can be written as

$$\begin{aligned} \Delta\mathbf{r} &= (D^T D)^{-1} D^T [\Delta\mathbf{d} - A\Delta\mathbf{q}] \\ \Delta\mathbf{q} &= (GA)^{-1} G \Delta\mathbf{d} \\ G &= A^T - A^T D (D^T D)^{-1} D^T \end{aligned}. \tag{24}$$

This equation is equivalent to Equation (18), except it explicitly separates the dependence on location from that on polarizability. Finally the model uncertainties in Equation (21) for both types of parameters may be expressed as

$$C_r = [(D^T D)^{-1} D^T (I - A(GA)^{-1} G][(D^T D)^{-1} D^T (I - A(GA)^{-1} G]^T$$
$$C_p = [(GA)^{-1} G][(GA)^{-1} G]^T \quad . \tag{25}$$

We see that the object location affects the estimation of polarizability through the G matrix, which is a modification of A by incorporating an additional term that involves the sensitivity matrix D to the object location. The above expressions of Equations (24) and (25) require the inverse of the matrices $D^T D$ and GA. The conditioning of these matrices determines how errors in the data translate to errors in the location and polarizability.

4.2.3 Survey-design framework

To determine the effectiveness of a given sensor system, we assume a survey area of 4 m $\times$ 4 m with an object located at the area center and buried at some depth (Figure 29). The red square in Figure 29 (a) represents the cued array which is positioned at the center of the region and occupies an area of 2 m $\times$ 2 m. The circles represent the designated stations for the moving systems. Figure 29 (b) illustrates how a 4-Tx system is sequentially fired when it is towed, where a square with a solid line represents an active transmitter, and a dashed line represents an inactive transmitter.

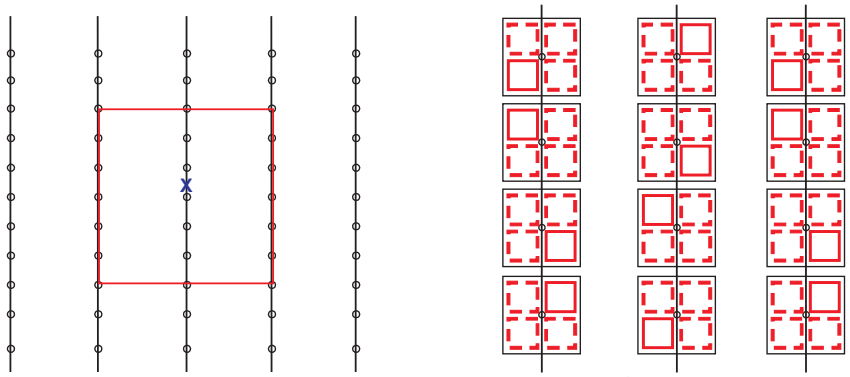

Figure 29: Schematic view of the experimental surveys. (a) The red square shows the area occupied by the cued array. The open circles represent the stations for the towed or cart systems. The cross represents the location of a buried object. (b) Schematic view of 4-Tx systems fired sequentially when moving. A square with a solid line represents an active transmitter, and a dashed line represents an inactive transmitter.

A line-spacing of $l_x = 1$ m is used for the multi-sensor towed system and $l_x = 0.4$ m for the cart system (to provide a fair comparison as the receivers in the towed system are 40 cm apart). For all the moving systems, the station spacing is $s_y = 0.125$ m which corresponds to a data collection rate of 8 measurements per second at a forward speed of 1 m/s. The sensors are assumed to be 20 cm above the surface.

We know proceed to estimate the covariance matrix of the polarizabilities and the location parameters using Equation 25. We first start with a spherical test-object and then consider a test-object with cylindrical symmetry (representative of a UXO).

4.2.4 Model covariance matrix for a spherical object

We first assume that a spherical object is buried at $(0, 0, -0.4)$. Because it is a sphere it has three equal principal polarizations and we assume these are all equal to 9.81 (the value of the principal polarization at 180 μs for a 37 mm projectile). Then the elements of the polarizability tensor $P(t)$ in Equation (6) are p_{ii} = 9.81 and $p_{ij} = 0, i \neq j$. Similar to Smith et al. (2004), we evaluate the Jacobian J at the true parameter values so as to remove any dependence of algorithms and noise realization in assessing the different systems. In these

Tables 5 list the covariance matrices for equivalent dipole polarizabilities computed for the 5 sensor systems with Equation (25) under the assumption of unit variance of $C_d = I$. Recall that the diagonal elements of the matrix represent variances of polarizability elements of p_{11}, $p_{12}, p_{13}, p_{22}, p_{23}, p_{33}$, and the off-diagonal elements the correlation between model parameters if the matrix is diagonally normalized.

The top part of Table 5 shows that the multi-Tx/Multi-Rx cued array has diagonal covariance matrix elements on the order of 10^{-3} with the off-diagonal elements even smaller. The total polarizability variance (i.e., the summation of the diagonal elements) is $\epsilon_p = 0.023$. In Table 5, we see that the single-Tx/25-Rx produces small values of variance and covariance, with $\epsilon_p = 0.2$. The 4-Tx/25-Rx, has slightly better accuracy with smaller variances in model variances and $\epsilon_p = 0.07$. The multicomponent EM-63 cart system cart system achieves similar accuracy to the two one-pass systems with $\epsilon_p = 0.12$. In contrast, the standard EM-63 system yields the largest variance in polarizabilities with $\epsilon_p = 10.34$. It also displays strong correlations between p_{11}, p_{22}, p_{33}, with the correlation coefficients equal to 0.97.

For N independent observations the uncertainty is proportional to $1/N$. To see if the small uncertainties in the new systems are mainly due to the increased number of data, we plot the total squared polarizability uncertainty against N in Figure 30. On the plot, we also show how σ^2/N behaves for different values of σ^2. If the reduction in variance was simply due to an increase in the number of observations then different system would lie along the same σ^2/N curve. The multi-sensor systems result in a much larger reduction in variance than $1/N$, indicating that they have inherently superior information on the characteristics of the buried object.

4.2.5 Object with cylindrical symmetry

We now examine the changes in the model covariances matrices for the five different systems when interrogating an object with cylindrical symmetry (UXO-like). We assume a polarization value of 9.81 along the symmetry axis and 4.36 along the transverse axis (corresponding to a 37 mm projectile). The cylindrical object is oriented at polar angles of $\theta = 90^0$, 45^0, and 0^0, corresponding to horizontal, tilted, and vertical scenarios, respectively. Note that the Jacobian D is dependent on the values of the elements of p_{ij} and thus has a dependency on the orientation of the object. In Table 6, we list model variances of locations and dipole polarizabilities for all test cases.

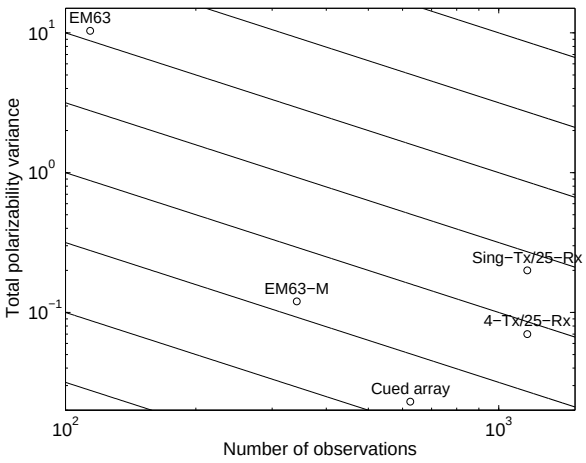

Figure 30: Comparison of total squared polarizability uncertainty against the number of observations for a sphere at 0.4 m depth. The solid black lines show how σ^2/N behaves for different values of σ^2.

For the horizontal case, the 6 polarizabilities are given by

$$[p_{11}, p_{12}, p_{13}, p_{22}, p_{23}, p_{33}] = [9.81, 0.0, 0.0, 4.36, 0.0, 4.36].$$

The polarizability p_{11} is related to the axial polarization, while p_{22} and p_{33} are related to the transverse polarization. All systems have small uncertainties in location but the standard EM-63 produces the largest values for locational uncertainty. Examining the polarizability uncertainty results in Table 6 reveals that the next-generation systems are more accurate than the standard EM63. The EM63 has the largest uncertainty in axial polarization with relatively small uncertainties in transverse polarization. Total squared uncertainty for the EM63 is 3.07, significantly larger than those of the other systems.

When the object is tilted at 45^0, the polarizabilities are

$$[p_{11}, p_{12}, p_{13}, p_{22}, p_{23}, p_{33}] = [7.09, 0.0, -2.72, 4.36, 0.0, 7.09].$$

where p_{11} and p_{33} are related to the average of the axial and transverse polarization, p_{13} is half the difference between the transverse and axial polarizations, while p_{22} is the transverse polarization. When compared with the horizontal case, the magntitude of the location uncertainties in the EM-63 are increased. This is illustrated in the relevant part of Table 6, where the corresponding polarizability uncertainties (for example p_{11}, p_{33}) becomes larger. Conversely, the modified systems still produce well resolved results. In this case, the total squared uncertainty of the EM-63 is 8.55, while the total squared uncertainties of the other systems remain at a similar order to the horizontal situation.

In the vertical case, the 6 polarizabilities are given by

$$[p_{11}, p_{12}, p_{13}, p_{22}, p_{23}, p_{33}] = [4.36, 0.0, 0.0, 4.36, 0.0, 9.81].$$

where p_{11} and p_{22} are related to the transverse polarization, while p_{33} is related to the axial polarization since the principal axes are coincident with the user coordinate axes. This is

the worst case scenario for the EM-63 as indicated by the very large uncertainty in the axial polarization in Table 6. The new systems still provide very satisfying results.

Overall, the new systems appear promising in their ability to accurately resolve the polarizabilities of an object at various orientations and different depths. In terms of total squared uncertainty, the system of 4-Tx/25-Rx is the best one-pass detection candidate.

4.3 FULL NON-LINEAR INVERSIONS: EFFECTS OF MEASUREMENTS ERRORS ON DIPOLE ESTIMATION

We now wish to test the performance of the candidate systems in recovering dipole polarizabilities when errors in sensor orientation and location are included. We use the polarization tensor model in a parametric form in which the $i-$th principal polarization is given by $L_i(t) = k_i t^{-\beta_i} e^{-\frac{t}{\gamma_i}}$ (Pasion and Oldenburg, 2001). The model parameters $\mathbf{m}$ contain the location of an object, its orientation, and k, β, γ parameters along three principal polarizations. Thus for a three-polarization inversion of EMI data, the total number of the unknowns is 15.

To produce synthetic data, we choose three items: 37 mm projectile, 81 mm mortar, and 4.2 inch mortar, representing small, medium, and large UXOs (with polarizabilities obtained from previous test-stand measurements). A total of 99 items consisting of 33 of each size of UXO are randomly seeded over cells with each cell taking up an area of 5 $\times 5\mathrm{m}^2$. The survey was set up with sensor heights of $h = 0.20$ m, line spacing $l_x = 1$ m, and station spacing $l_y = 0.125$ m. Based on the analysis in the semi-analytical approach, a line spacing of 0.4 m is used for the EM-63 for a fair comparison. The synthetic data are corrupted with simulated measurement errors.

Given measured data, the objective is to find the $\mathbf{m}$ that minimizes the following cost function

$$\begin{aligned} \hat{\mathbf{m}} &= \arg\min \Phi(\mathbf{m}) \\ \Phi(\mathbf{m}) &= \sum_{i=1}^{M} \sum_{j=1}^{N} w_{ij} \left| d_{i,\mathrm{obs}}(t_j) - d_{i,\mathrm{pred}}(t_j, \mathbf{m}) \right|^2 \\ &\text{subject to } \mathbf{m}_l \geq \mathbf{m} \leq \mathbf{m}_u, \end{aligned} \tag{26}$$

where $\mathbf{m}_l$ and $\mathbf{m}_u$ are model lower and upper bounds and w_{ij}'s are data weighting coefficients which are usually chosen as:

$$w_{ij} = \frac{1}{f + \eta |d_{i,\mathrm{obs}}(t_j)|}. \tag{27}$$

The parameter η is a percentage that down-weights the influence of the large data values; typically we chose $1\% \geq \eta \leq 5\%$. The parameter f (ensures that the denominator in the above equation does not get too close to zero when $d_{i,\mathrm{obs}}(t_j)$ approaches zero.

For the cued array, the simulations were carried out under assumption of Gaussian random sensor noise, randn, which an amplitude as function of time of $\frac{\alpha}{\sqrt{(t)}} * \mathrm{randn}$. We use $\alpha = 0.6$

for the dynamic systems, which produces noise of similar magnitude to what we've observed at field sites with the EM63. The cued array can achieve higher signal-to-noise ratio (SNR) than a moving system through stacking (and by elimination of motion noise). For the cued array, we ran simulations with both $\alpha = 0.6$ and 0.06 for comparison purposes. For the moving systems, the simulations were done considering all sources of data error that typically arise including inaccuracies in sensor position and orientation as well as sensor noise. We assume that the errors in sensor orientation and position are Gaussian with a standard deviation of $\sigma_{\text{orien}} = 2^0$, a standard deviation of σ_{pos} = 2 cm, and 5 cm.

We include all plots and tables of the simulations in an Appendix to demonstrate and describe the recovered parameters and polarizations and their statistics. In the main text, we present a summary of results for the 5 systems in a few combined figures and tables for easy examination and refer readers to the Appendix for additional details. The descriptions or definitions of the plots appear in the figures that are given in the appendix. Briefly, the subscripts p, s, and t represent the primary, secondary, and tertiary parameter or polarization in the analysis.

Tables 7-9 list all SD and RMSE (defined in Equations (A-1) and (A-2)) values to give a total measure of difference between the recovered parameters of (k, β, γ) and the true parameters for each of the three UXO items. In the summary tables, different noisy simulations when using the moving systems refer to:

- Noisy case I: sensor noise of $\frac{0.6}{\sqrt{t}} * \text{randn}$ and sensor errors with $\sigma_{\text{orien}} = 2^0$, $\sigma_{\text{pos}} = 2$ cm.
- Noisy case II: sensor noise of $\frac{0.6}{\sqrt{t}} * \text{randn}$ and sensor errors with $\sigma_{\text{orien}} = 2^0$, $\sigma_{\text{pos}} = 5$ cm.
- Noisy case III: only sensor positional errors with standard error of $\sigma_{\text{pos}} = 1$ cm.
- Noisy case IV: only sensor positional errors with standard error of $\sigma_{\text{pos}} = 2$ cm.
- Noisy case V: only sensor positional errors with standard error of $\sigma_{\text{pos}} = 5$ cm.

Figure 31 shows the summarized results for the 5 systems in the order of the cued array, single-Tx/25-Rx, 4-Tx/25-Rx, and EM63-M, and EM63 from the top to the bottom. For the moving systems the simulations assumed sensor position and orientation errors of $\sigma_{\text{orien}} = 2^0$, σ_{pos} = 2 cm. In the k_p-k_s plots, we generally observe three tight clusters around groundtruth values for the first 4 systems while the EM63 has a larger spread particularly for the 81 and 4.2" mortars. In the β_p-γ_p plots, the cued array has very tight parameter clusters. The single-Tx, 4-Tx, and EM63-M systems have three linearly clustered patterns but the EM63 has no significant clustering for the ATC 81 mm. In the plot $L_p(t_1)$ versus $L_p(t_{21})/L_p(t_1)$, there is a tight-clustering of all three items in the Cued, 4-Tx, EM63-M, and Single-Tx systems. The single-Tx system, has a larger spread in the relative decay rate for the 37 mm indicating that the polarization at late time is not well recovered (also refer to Figures A-3 in the appendix). For the EM63, there is very poor clustering for any of the items. The right most panel shows the difference between the secondary and tertiary polarizations at t_1 and t_{21} normalized by the respective true values. These plots may be used to examine how well the cylindrical symmetry of an object is predicted. Generally, we anticipate that polarization at early time is

recovered more accurately than that at late time and thus the spread is most likely to occur along the horizontal direction in that plot. In this simulation, we can see that the EM63 has a very large spread that would prevent use of this feaature vector for discrimination. The other systems have a relatively smaller spread thus providing an indication that the buried item has cylindrical symmetry.

Figure 32 presents the results when the level of sensor position errors is increased to a standard deviation of $\sigma_{\rm pos}$ = 5 cm while keeping the same amount of sensor noise and sensor-orientation error. The towed systems of single-Tx and 4-Tx still display good performance. The multi-component EM63 cart system yields acceptable results but the EM63 appears quite sensitive to the increasing level of sensor position errors and produces degraded results.

Overall, the simulations show that the 4-Tx towed system generally has smaller SD and RMSE values (as summarized in tables 7-9) and achieves the best performance among the moving systems.

We also conducted simulations for the EM63 under pure random errors in sensor position to examine what minimal level of positional precision is justified in the existing EMI systems. Three levels of sensor positional errors are considered in the simulation with standard deviations of $\sigma_{\rm pos} = 1$ cm, 2 cm, and 5 cm. As before, we put all the plots and tables derived from these simulation in the appendix and summarize the results in Figure 33, where the results obtained previously from the 4-Tx towed system are also displayed for comparison. For small positional errors of $\sigma_{\rm pos} = 1$ cm and 2 cm, the EM63 produces good results in which all three items can be distinguished and a small spread in the discrepancy between the secondary and tertiary polarizations is observed. When positional errors are increased to $\sigma_{\rm pos} = 5$ cm, the EM63 loses the capability to give informative results. Figure 33 illustrates that the towed 4-Tx system with a positional error $\sigma_{\rm pos} = 5$ cm has similar performance to the EM63 with a standard deviation of less than $\sigma_{\rm pos} = 2$ cm. Notice that the results from the 4-Tx system were obtained considering sources of errors icluding sensor position and orientation as well as sensor noise. Thus we can expect that the 4-Tx system can achieve the desired performance without the strict condition of 1 cm positional accuracy required in the existing systems for successful discrimination.

4.4 SUMMARY AND DISCUSSION

In EMI sensing, our ultimate goal is to accurately recover or invert for parameters of a buried target that allow some level of discrimination to be achieved between UXOs and clutter. The accuracy of the inversion solution is dependent upon a number of factors such as the specifics of the inversion method, the assumed signal model, and the data acquisition attributes. The sensor system used is probably the most fundamental determinant of discrimination capability. The work presented here was focused on the evaluation of next-generation sensor systems using a polarization tensor model.

Methods to forecast discrimination performance are essential for sound design of potential sensor systems. There are various approaches to carry out such a task. We undertook an

assessment using both deterministic and stochastic methods. In the deterministic framework, we employed semi-analytical metrics, based on a linearization of the underlying inversion algorithm. The covariance matrix of the model parameters was the diagnostic used to evaluate candidate systems. Using the framework we predicted that the multisensor systems had significantly improved performance relative to the EM-63. The 4-Tx/25-Rx system was the best performing of the one-pass detection and discrimination systems.

In the Monte Carlo simulations we conducted full non-linear inversion using synthetic data that are contaminated with sensor noise and errors in position and orienation. In the simulations we considered 37 mm projectiles, and 81 and 4.2 inch mortars. The tests show that the standard EM-63 requires high precision of position, at least within 2 cm accuracy to get reliable estimates of dipole polarizability. They further showed that the multi-sensor systems perform very well. In particular, the 4-Tx/25-Rx system is robust to positional and orientation errors of 5 cm and 2^o and outperforms noise-free EM-63 data with 1-2 cm positional error.

Table 5: Model covariance matrices C_p for all five systems for the the sphere at z_0 = -0.4 m.

	Cued array, $\epsilon_p = 0.023$					
model	p_{11}	p_{12}	p_{13}	p_{22}	p_{23}	p_{33}
p_{11}	0.007051	0.000000	0.000000	0.003936	0.000000	0.004080
p_{12}	0.000000	0.001558	-0.000000	0.000000	0.000000	0.000000
p_{13}	0.000000	-0.000000	0.001047	0.000000	0.000000	0.000000
p_{22}	0.003936	0.000000	0.000000	0.007051	0.000000	0.004080
p_{23}	0.000000	0.000000	0.000000	0.000000	0.001047	0.000000
p_{33}	0.004080	0.000000	0.000000	0.004080	0.000000	0.004889
	Single-Tx/25-Rx, $\epsilon_p = 0.2$					
p_{11}	0.068619	0.000000	0.000000	0.017538	0.000000	0.023519
p_{12}	0.000000	0.021494	-0.000000	0.000000	0.000000	-0.000000
p_{13}	0.000000	-0.000000	0.014334	0.000000	0.000000	0.000000
p_{22}	0.017538	0.000000	0.000000	0.050879	0.000000	0.024003
p_{23}	0.000000	0.000000	0.000000	0.000000	0.011604	0.000000
p_{33}	0.023519	-0.000000	0.000000	0.024003	0.000000	0.035774
	4-Tx/25-Rx, $\epsilon_p = 0.07$					
p_{11}	0.027855	-0.000232	-0.000054	0.007994	0.000048	0.008712
p_{12}	-0.000232	0.005428	0.000041	-0.000140	0.000054	-0.000168
p_{13}	-0.000054	0.000041	0.003439	-0.000022	-0.000083	-0.000068
p_{22}	0.007994	-0.000140	-0.000022	0.016335	0.000085	0.010810
p_{23}	0.000048	0.000054	-0.000083	0.000085	0.002846	0.000185
p_{33}	0.008712	-0.000168	-0.000068	0.010810	0.000185	0.012823
	EM63-M, $\epsilon_p = 0.12$					
p_{11}	0.017193	-0.000000	-0.005574	0.005462	0.000000	0.013728
p_{12}	-0.000000	0.003046	-0.000000	-0.000000	-0.000564	-0.000000
p_{13}	-0.005574	-0.000000	0.024482	0.002195	0.000000	0.002832
p_{22}	0.005462	-0.000000	0.002195	0.013430	0.000000	0.012876
p_{23}	0.000000	-0.000564	0.000000	0.000000	0.018842	0.000000
p_{33}	0.013728	-0.000000	0.002832	0.012876	0.000000	0.039962
	EM63, $\epsilon_p = 10.34$					
p_{11}	2.021576	0.000000	0.096757	1.992680	-0.000000	3.439111
p_{12}	0.000000	0.032325	0.000000	0.000000	0.002251	0.000000
p_{13}	0.096757	0.000000	0.089334	0.119573	0.000000	0.207360
p_{22}	1.992680	0.000000	0.119573	2.085530	0.000000	3.500249
p_{23}	-0.000000	0.002251	0.000000	0.000000	0.074910	0.000000
p_{33}	3.439111	0.000000	0.207360	3.500249	0.000000	6.038188

Table 6: Model variances for the object with cylindrical symmetry.

System	σ_x^2	σ_y^2	σ_z^2	$\sigma_{p_{11}}^2$	$\sigma_{p_{12}}^2$	$\sigma_{p_{13}}^2$	$\sigma_{p_{22}}^2$	$\sigma_{p_{23}}^2$	$\sigma_{p_{33}}^2$	ϵ_p
	$\theta = 90^0$, z_0 = -0.4 m, $[p_{11}, p_{12}, p_{13}, p_{22}, p_{23}, p_{33}] = [9.81, 0.0, 0.0, 4.36, 0.0, 4.36]$.									
Cued array	3.0E-6	4.0E-6	4.0E-6	0.018	1.6E-3	7.3E-4	6.0E-3	8.8E-4	3.8E-3	0.031
Single Tx	4.9E-5	5.7E-5	4.9E-5	0.12	0.02	0.007	0.044	0.010	0.026	0.22
4 Txs	1.2E-5	1.6E-5	1.6E-5	0.049	0.0054	0.0018	0.015	0.0024	0.011	0.085
EM63-M	1.6E-5	1.5E-5	1.4E-5	0.043	0.0031	0.0035	0.012	0.007	0.023	0.091
EM63	9.0E-5	9.9E-5	7.4E-4	1.90	0.033	0.025	0.27	0.039	0.81	3.17
	$\theta = 45^0$, z_0 = -0.4 m, $[p_{11}, p_{12}, p_{13}, p_{22}, p_{23}, p_{33}] = [7.09, 0.0, -2.72, 4.36, 0.0, 7.09]$.									
Cued array	3.0E-6	4.0E-6	2.0E-6	8.4E-3	1.8E-3	1.8E-3	4.6E-3	1.5E-3	4.8E-3	0.023
Single Tx	3.7E-5	3.7E-5	2.6E-5	0.074	0.024	0.019	0.035	0.015	0.036	0.203
4 Txs	9.0E-5	1.0E-5	7.0E-6	0.029	0.0061	0.005	0.009	0.004	0.013	0.067
EM63-M	1.7E-5	1.5E-5	1.0E-5	0.042	0.0078	0.018	0.0094	0.015	0.038	0.13
EM63	2.3E-4	2.1E-4	1.9E-3	2.35	0.074	1.05	0.32	0.163	4.60	8.55
	$\theta = 0^0$, z_0 = -0.4 m, $[p_{11}, p_{12}, p_{13}, p_{22}, p_{23}, p_{33}] = [4.36, 0.0, 0.0, 4.36, 0.0, 9.81]$.									
Cued Array	4.0E-6	4.0E-6	1.0E-6	4.0E-3	1.6E-3	2.7E-3	4.0E-3	2.7E-3	5.6E-3	0.021
Single Tx	2.8E-5	2.8E-5	1.8E-5	0.054	0.021	0.024	0.033	0.022	0.044	0.20
4 Txs	8.0E-6	8.0E-6	4.0E-6	0.023	5.4E-3	6.8E-3	7.8E-3	6.5E-3	0.014	0.064
EM63-M	2.9E-5	1.3E-5	8.0E-6	0.015	3.0E-3	0.048	0.010	0.024	0.051	0.15
EM63	5.0E-4	4.8E-4	2.20E-3	0.22	0.032	0.68	0.20	0.66	10.38	12.16
	$\theta = 0^0$, z_0 = -0.2 m. $[p_{11}, p_{12}, p_{13}, p_{22}, p_{23}, p_{33}] = [4.36, 0.0, 0.0, 4.36, 0.0, 9.81]$.									
Cued array	0.00	0.00	0.00	2.4E-4	1.1E-4	1.2E-4	2.4E-4	1.2E-4	3.0E-4	0.001
Single Tx	0.00	0.00	0.00	0.012	2.5E-3	3.2E-3	3.5E-3	1.8E-3	4.0E-3	0.027
4 Txs	0.00	0.00	0.00	3.8E-3	4.2E-4	5.7E-4	5.5E-4	3.9E-4	9.8E-4	6.7E-3
EM63-M	0.0	0.0	0.0	6.2E-4	1.56E-4	8.5E-4	3.3E-4	1.56E-4	3.7E-4	2.5E-3
EM63	2.0E-5	1.6E-5	1.3E-4	0.025	0.0023	0.04	0.017	0.03	0.76	0.88

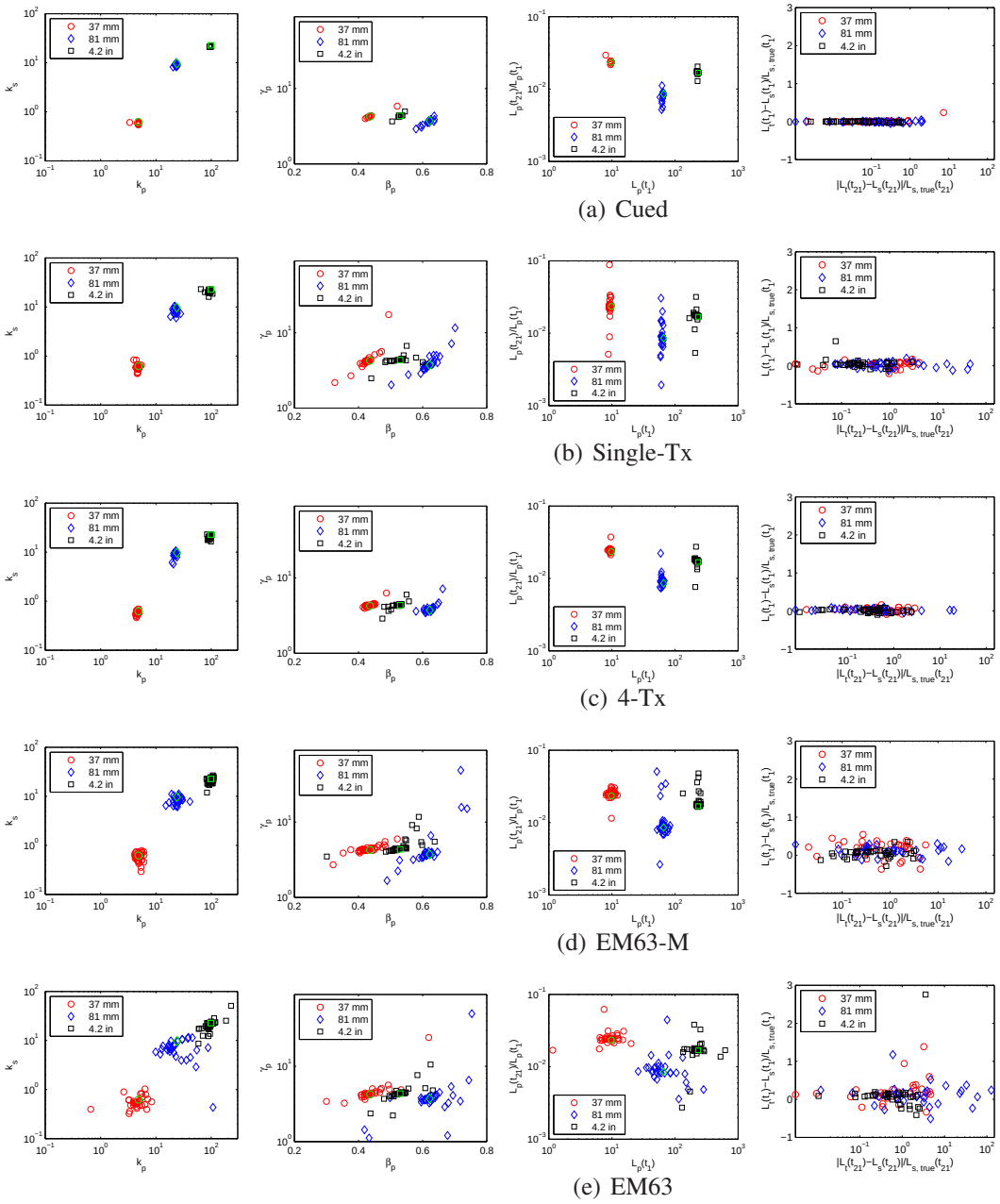

Figure 31: The results of three-polarization inversion of noisy data using 5 systems. Five rows: (a) Cued array, sensor noise only; (b) Single-Tx/25-Rx; (c) 4-Tx/25-Rx; (d) EM63-M; (e) EM63. For (b)-(e) measurement errors: sensor noise + errors in sensor position and orientation with $\sigma_{\text{orien}} = 2^0$, $\sigma_{\text{pos}} = 2$ cm. In all cases, sensor noise is simulated as $\frac{0.6}{\sqrt{t}} * \text{randn}$.

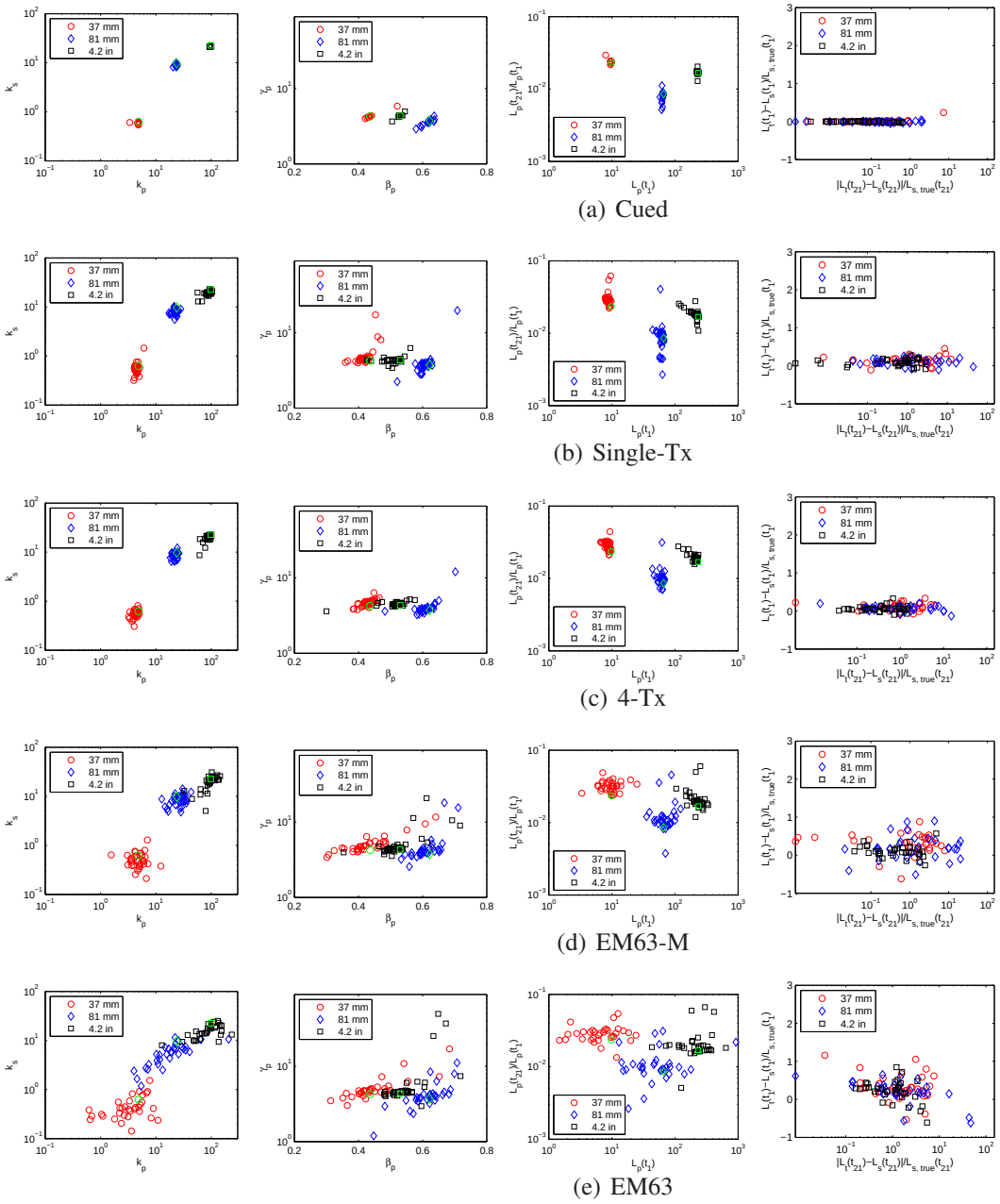

Figure 32: The results of three-polarization inversion of noisy data using 5 systems. Five rows: (a) Cued array, sensor noise only; (b) Single-Tx/25-Rx; (c) 4-Tx/25-Rx; (d) EM63-M; (e) EM63. For (b)-(e) measurement errors: sensor noise + errors in sensor position and orientation with $\sigma_{\text{orien}} = 2^0$, $\sigma_{\text{pos}} = 5$ cm. In all cases, sensor noise is simulated as $\frac{0.6}{\sqrt{t}} * \text{randn}$.

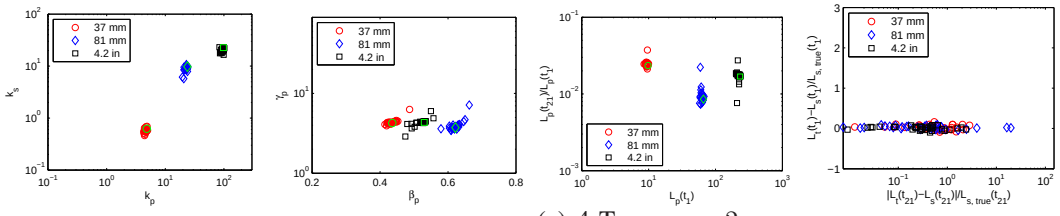

(a) 4-Tx, $\sigma_{\text{pos}} = 2$ cm.

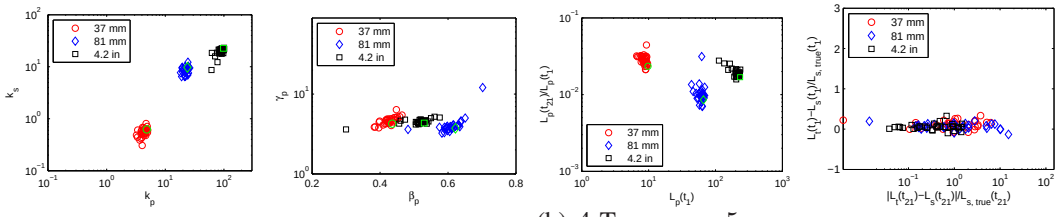

(b) 4-Tx, $\sigma_{\text{pos}} = 5$ cm.

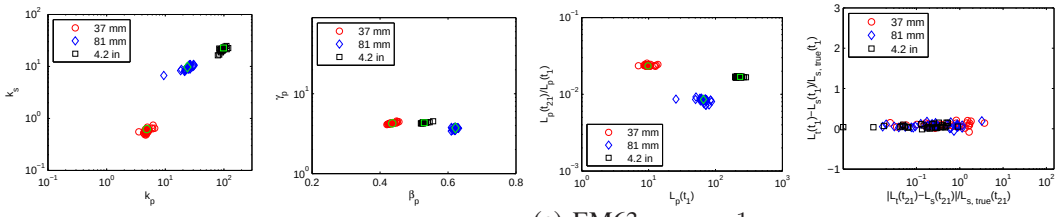

(c) EM63, $\sigma_{\text{pos}} = 1$ cm

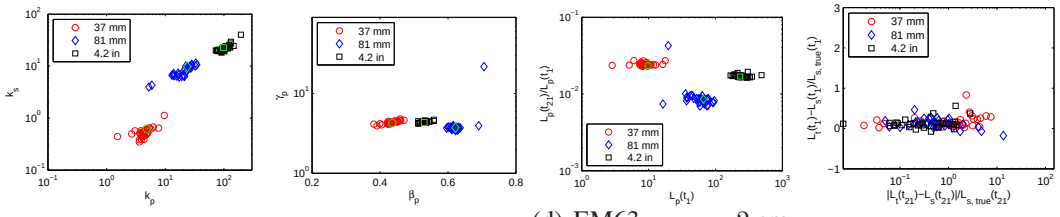

(d) EM63, $\sigma_{\text{pos}} = 2$ cm

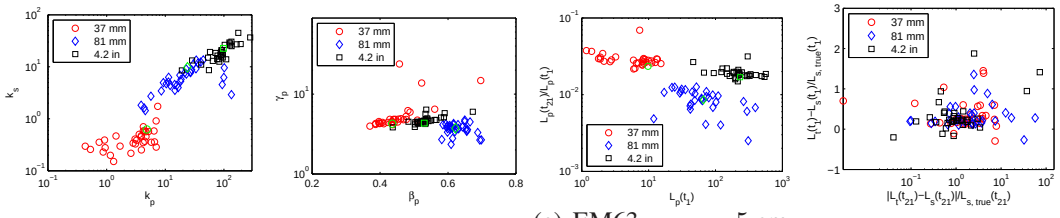

(e) EM63, $\sigma_{\text{pos}} = 5$ cm

Figure 33: The results of three-polarization inversion of noisy data using EM63 and 4-Tx systems. For 4-Tx system, measurement errors including sensor noise $(\frac{0.6}{\sqrt{t}} * \text{randn})$, perturbations in sensor position and orientation with $\sigma_{\text{orien}} = 2^0$, $\sigma_{\text{pos}} = 2, 5$ cm in row (a) and (b). For EM63: only perturbations in sensor position are simulated with $\sigma_{\text{pos}} = 1, 2, 5$ cm in row (c)-(e).

Table 7: Statistical results for 3-polarization inversion of 37 mm using 5 systems.

Parameters		k_p	k_s	k_t	β_p	β_s	β_t	γ_p	γ_s	γ_t
	True	4.84	0.62	0.62	0.44	1.15	1.15	4.25	5.67	5.67
Cued array, noise: $\frac{0.06}{\sqrt{t}}$.	SD	0.06	0.01	0.01	0.00	0.00	0.01	0.01	0.33	0.25
	RMSE	0.01	0.01	0.01	0.00	0.00	0.00	0.00	0.06	0.04
Cued array, noise: $\frac{0.6}{\sqrt{t}}$.	SD	0.26	0.03	0.06	0.02	0.02	0.04	0.28	2.04	3.26
	RMSE	0.05	0.04	0.09	0.03	0.02	0.03	0.07	0.36	0.57
Single-Tx, noisy case I	SD	0.28	0.09	0.18	0.03	0.07	0.13	2.37	6.20	8.92
	RMSE	0.06	0.14	0.29	0.06	0.06	0.11	0.56	1.09	1.57
4-Tx, noisy case I	SD	0.26	0.06	0.08	0.01	0.05	0.06	0.38	5.08	2.73
	RMSE	0.05	0.10	0.12	0.03	0.04	0.05	0.09	0.90	0.48
EM63-M, noisy case I	SD	0.58	0.12	0.28	0.04	0.15	0.16	0.53	4.62	6.23
	RMSE	0.12	0.19	0.44	0.09	0.13	0.14	0.12	0.81	1.10
EM63, noisy case I	SD	1.45	0.16	0.29	0.05	0.14	0.18	3.49	4.73	8.76
	RMSE	0.30	0.26	0.46	0.11	0.12	0.16	0.82	0.83	1.54
Single-Tx, noisy case II	SD	0.51	0.19	0.31	0.03	0.10	0.17	2.52	5.54	10.20
	RMSE	0.11	0.30	0.50	0.07	0.09	0.15	0.59	0.98	1.80
4-Tx, noisy case II	SD	0.73	0.12	0.14	0.02	0.08	0.12	0.64	8.67	9.87
	RMSE	0.15	0.19	0.23	0.05	0.07	0.11	0.15	1.53	1.74
EM63-M, noisy case II	SD	1.79	0.22	0.41	0.07	0.22	0.28	1.89	9.87	11.35
	RMSE	0.37	0.36	0.65	0.17	0.19	0.24	0.44	1.74	2.00
EM63, noisy case II	SD	2.64	0.31	0.36	0.08	0.25	0.29	2.69	9.58	7.62
	RMSE	0.55	0.50	0.58	0.17	0.22	0.25	0.63	1.69	1.34
EM63, noisy case III	SD	0.59	0.07	0.08	0.01	0.03	0.04	0.09	1.96	2.78
	RMSE	0.12	0.11	0.14	0.02	0.02	0.04	0.02	0.35	0.49
EM63, noisy case IV	SD	1.41	0.16	0.22	0.02	0.06	0.10	0.19	4.28	7.85
	RMSE	0.29	0.25	0.35	0.04	0.05	0.09	0.04	0.75	1.38
EM63, noisy case V	SD	2.43	0.33	0.42	0.06	0.29	0.26	4.27	6.33	12.74
	RMSE	0.50	0.53	0.67	0.14	0.25	0.23	1.00	1.12	2.25

Table 8: Statistical results for 3-polarization inversion of 81 mm using 5 systems.

Parameters		k_p	k_s	k_t	β_p	β_s	β_t	γ_p	γ_s	γ_t
	True	23.88	9.73	9.73	0.62	0.79	0.79	3.73	1.87	1.87
Cued array, noise: $\frac{0.06}{\sqrt{t}}$	SD	0.04	0.05	0.07	0.00	0.00	0.00	0.02	0.02	0.02
	RMSE	0.00	0.01	0.01	0.00	0.00	0.00	0.01	0.01	0.01
Cued array, noise: $\frac{0.6}{\sqrt{t}}$.	SD	0.80	0.59	0.48	0.01	0.02	0.03	0.26	0.22	0.22
	RMSE	0.03	0.06	0.05	0.02	0.03	0.04	0.07	0.12	0.12
Single-Tx, noisy case I	SD	1.95	1.42	1.27	0.03	0.06	0.07	1.60	4.84	4.84
	RMSE	0.08	0.15	0.13	0.05	0.08	0.09	0.43	2.59	2.59
4-Tx, noisy case I	SD	1.54	1.17	0.83	0.01	0.06	0.05	0.65	2.20	2.20
	RMSE	0.06	0.12	0.08	0.02	0.07	0.06	0.17	1.18	1.18
EM63-M, noisy case I	SD	4.45	1.80	2.04	0.05	0.09	0.08	8.38	1.71	1.71
	RMSE	0.19	0.19	0.21	0.08	0.11	0.10	2.24	0.92	0.92
EM63, noisy case I	SD	21.48	3.59	13.15	0.07	0.20	0.15	8.11	8.71	8.71
	RMSE	0.90	0.37	1.35	0.11	0.25	0.20	2.17	4.65	4.65
	SD	2.71	1.88	1.69	0.03	0.07	0.09	2.83	4.86	4.86
Single-Tx, noisy case II	RMSE	0.11	0.19	0.17	0.05	0.08	0.11	0.76	2.60	2.60
4-Tx, noisy case II	SD	2.52	1.62	1.54	0.03	0.08	0.08	1.50	1.74	1.74
	RMSE	0.11	0.17	0.16	0.06	0.10	0.10	0.40	0.93	0.93
EM63-M, noisy case II	SD	7.28	2.42	6.06	0.04	0.14	0.12	3.30	6.22	6.22
	RMSE	0.31	0.25	0.62	0.06	0.18	0.15	0.88	3.32	3.32
EM63, noisy case II	SD	34.96	4.69	9.74	0.07	0.13	0.13	3.78	4.39	4.39
	RMSE	1.46	0.48	1.00	0.11	0.17	0.16	1.01	2.35	2.35
EM63, noisy case III	SD	3.95	0.99	1.27	0.01	0.01	0.01	0.10	0.22	0.22
	RMSE	0.17	0.10	0.13	0.01	0.02	0.01	0.03	0.12	0.12
EM63, noisy case IV	SD	7.22	2.44	2.28	0.02	0.03	0.06	3.13	1.44	1.44
	RMSE	0.30	0.25	0.23	0.03	0.04	0.07	0.84	0.77	0.77
EM63, noisy case V	SD	31.56	4.65	5.27	0.03	0.14	0.05	0.56	2.09	2.09
	RMSE	1.32	0.48	0.54	0.05	0.17	0.06	0.15	1.12	1.12

Table 9: Statistical results for 3-polarization inversion of 4.2 inch mortars using 5 systems.

Parameters		k_p	k_s	k_t	β_p	β_s	β_t	γ_p	γ_s	γ_t
	True	98.30	22.60	22.60	0.53	0.95	0.95	4.33	3.80	3.80
Cued array, noise: $\frac{0.06}{\sqrt{t}}$.	SD	0.22	0.25	0.14	0.00	0.01	0.01	0.02	0.16	0.07
	RMSE	0.00	0.01	0.01	0.00	0.01	0.01	0.01	0.04	0.02
Cued array, noise: $\frac{0.6}{\sqrt{t}}$.	SD	2.05	0.68	0.56	0.01	0.01	0.02	0.17	0.27	0.32
	RMSE	0.02	0.03	0.02	0.01	0.01	0.02	0.04	0.07	0.08
Single-Tx, noisy case I	SD	8.53	2.09	1.61	0.03	0.03	0.03	0.55	2.69	0.83
	RMSE	0.09	0.09	0.07	0.05	0.03	0.04	0.13	0.71	0.22
4-Tx, noisy case I	SD	5.41	2.45	1.20	0.02	0.04	0.04	0.43	3.82	0.56
	RMSE	0.05	0.11	0.05	0.04	0.04	0.04	0.10	1.01	0.15
EM63-M, noisy case I	SD	8.30	3.29	3.48	0.05	0.07	0.08	1.76	4.09	0.88
	RMSE	0.08	0.15	0.15	0.10	0.07	0.09	0.41	1.08	0.23
EM63, noisy case I	SD	31.76	6.86	12.32	0.04	0.09	0.12	1.35	7.35	5.38
	RMSE	0.32	0.30	0.55	0.07	0.10	0.13	0.31	1.93	1.42
Single-Tx, noisy case II	SD	14.14	3.72	2.18	0.03	0.05	0.06	0.43	2.42	1.45
	RMSE	0.14	0.16	0.10	0.06	0.05	0.06	0.10	0.64	0.38
4-Tx, noisy case II	SD	13.77	4.06	2.16	0.05	0.10	0.07	0.35	3.35	0.86
	RMSE	0.14	0.18	0.10	0.09	0.11	0.08	0.08	0.88	0.23
EM63-M, noisy case II	SD	23.91	6.20	6.03	0.06	0.10	0.12	3.43	8.49	1.78
	RMSE	0.24	0.27	0.27	0.12	0.10	0.12	0.79	2.23	0.47
EM63, noisy case II	SD	44.10	8.03	10.35	0.06	0.15	0.12	10.44	11.44	1.56
	RMSE	0.45	0.36	0.46	0.11	0.15	0.12	2.41	3.01	0.41
EM63, noisy case III	SD	8.83	2.16	1.46	0.01	0.01	0.01	0.05	0.24	0.40
	RMSE	0.09	0.10	0.06	0.01	0.01	0.01	0.01	0.06	0.11
EM63, noisy case IV	SD	23.94	3.94	7.85	0.01	0.03	0.03	0.12	0.73	0.83
	RMSE	0.24	0.17	0.35	0.02	0.03	0.04	0.03	0.19	0.22
EM63, noisy case V	SD	142.04	8.91	23.03	0.09	0.14	0.13	0.80	2.63	5.27
	RMSE	1.45	0.39	1.02	0.17	0.14	0.13	0.18	0.69	1.39

5 DISCUSSION AND RECOMMENDATIONS

5.1 DISCUSSION

In this project, we conducted a feasibility analysis of a one-pass detection and discrimination system. We focused on (i) estimating the position and orientation accuracies that can be achieved in a dynamic survey mode; and (ii) on simulating the discrimination performance of a number of candidate EMI sensors when subjected to different position and orientation errors.

For sensor positioning we used Novatel SPAN system with a tactical grade IMU that has a drift rate of $1° \text{ hr}^{-1}$. The data were post-processed in the commercially available Inertial Explorer package. Two positional tests were conducted, the first using a Rotating Amusement Park carousel, and the second using an EM61 towed array.

The RAP was instrumented with a precision optical encoder and the SPAN system was installed on a tilt-table at a fixed position on the RAP. The known distance of the SPAN system from the axis of revolution of the RAP ride, the tilt table angle and the optical encoder information provided accurate ground-truth. The GPS and IMU data from the SPAN were augmented by an optical encoder attached to a bicycle wheel that was attached to the RAP and which was in constant contact with the ground. For one run, when the system was moving at a brisk 2 meters per second, the position estimated from the IMU/GPS combination had a root-mean-square error of between 1.1 and 1.8 cm.

For the second position test, a laser prism was mounted on the rear left corner of an EM61 towed-array, about 1.5 m away from the Novatel SPAN system which was mounted on the tow-bar in line with the center of the towed-array. The SPAN predicted positions of the prism were compared to the prism positions measured with a Trimble SCS930 Universal Total Station. Data were collected at various speeds between 0.2 and 1.3 meters per second, on both smooth and rough ground, with the array traveling along, straight or curved paths and with ramps sometimes present that one side of the cart had to travel over. Amongst all the tests the root-mean-squared (RMS) horizontal error varied from a minimum of 0.6 cm to a maximum of 1.7 cm. These represent upper bounds on the horizontal positional error of the SPAN system. If the error was entirely due to the SPAN heading, the RMS heading error would vary from a minimum of 0.2^{o} to a maximum of 0.6^{o}. RMS errors of the 3-D positions (including elevation) varied from 0.8 to 3.2 cm. The runs with larger errors typically exhibited systematic biases in the elevation angles. This indicates that there may be 1-2 cm magnitude systematic differences in the SPAN elevations along adjacent transect paths.

Numerical investigation of simulation performance occurred along two fronts. The first was semi-analytical and based on estimating the expected errors in the positions and polarizabilities of a buried metallic object. The second was based on Monte-Carlo simulations of systems subjected to different amounts of sensor, position and orientation noise. Five different sensor systems were evaluated including an EM63 equivalent, EM-63 with 3-axis receiver and three versions of the TEMTADS with one deployed in cued

mode, and the other two in dynamic mode. Both the semi-analytical and monte-carlo approaches demonstrated the excellent performance of the TEMTADS cued-system. They also revealed that the dynamic variants of that system have significantly improved performance over an EM63 equivalent. In particular, the multiple receiver coils makes the TEMTADS more tolerant of positional errors the EM63. The four-transmitter TEMTADS with 5 cm position error and 2^o orientation error outperforms an EM63 with 1 cm and 1^o error.

5.2 RECOMMENDATIONS

We recommend adapting the TEMTADS cued-interrogation array for use in a one-pass detection and discrimination mode. The following issues need to be considered when adapting the TEMTADS for use in a one-pass detection and discrimination mode:

1) Positional and orientation accuracy: In a dynamic mode, discrimination relies on accurate relative position between successive measurements. The simulations in the last section demonstrated that parameter clusters produced with one suggested mobile version of the TEMTADS deployed with 5 cm error in position and 2 degree error in orientation were comparable to clusters produced from EM63 data with 1 cm position and 1 degree orientation error. Furthermore, the tests with the EM61 towed array at FLBGR demonstrated SPAN RMS position errors of better than 1-2 cm and orientations of better than 0.6 degrees. We therefore recommend using the Novatel SPAN system with data post-processed in the Inertial Explorer software package, with the GPS potentially augmented with the Trimble SCS930 laser-positioning system.
2) Timing accuracy: The accurate and stable synchronization of the different sensor components is a critical requirement for successful discrimination based on dynamically collected data. We recommend using the SKY DAS to provide accurate time-stamping of all system components. It has the ability to simultaneously time-stamp all incoming data with 10 millisecond accuracy, synchronized to the timing pulse of a GPS receiver. The TEMTADS should be configured to output a precise pulse at the start of the transmitter on-time and an event identifier. The DAS could ingest and time-stamp the pulse and the event identifier, which could then be used to assign accurate times to the TEMTADS data which would still be logged within the existing control software for that sensor.
3) Measurement time and data-density: The longer the time-range measured, the further the array will move during a single measurement, the lower the density of the measurements and the lower the SNR at the later time-channels. The TEMTADS has the ability to measure the time-decay to 25 ms after transmitter shut-off, with a single measurement with that time range requiring about 100 ms to collect. The ESTCP MM-0504 demonstrations at FLBGR and Camp Sibert demonstrated that the wider measurement range of the EM63 (to 25 ms) resulted in superior discrimination performance to the EM61 (to 1 ms). It's not clear as to whether measurements are required all the way out to 25 ms and some compromise of measuring out to, say, 8 ms, may prove to be more effective (measurements require 32 ms and hence the data-density will be about 3 times greater than at 25 ms decay). The TEMTADS

measurement characteristics are user-configurable and should be investigated as part of the proposed follow-on ESTCP project. During that project we would also implement and investigate the efficacy of explicitly including the sensor movement during measurement in the polarization tensor inversion process.

4) Signal to noise ratio: In cued-mode, the data are stacked to improve signal-to-noise ratio (typically 27 repeats of a negative then positive transmit cycle are used). In dynamic mode, the choice of the number of stacks involves a compromise between improving SNR and blurring of spatial detail. The lower the number of stacks, the less movement that occurs during each measurement. The greater the current in the transmitter the better the SNR, but the longer the delay before the receiver response to the transmitter has decayed sufficiently. As part of the follow-on project, we recommend determining the maximum practical increase in transmitter current that can be achieved with the existing TEMTADS transmitters, and if necessary, the construction of new transmitters and circuitry to improve SNR (see 6) below). Movement during the receive period also introduces dynamic motion noise which reduces the SNR. In an effort to combat that noise source we recommend including an extra reference sensor 0.5 m higher than the existing plane of sensors. This reference sensor will sense approximately the same ambient noise as the other receivers, and due to its increased height, will have a significantly reduced response from any items of interest.
5) Change in background response from the ground: During mobile data collection, the geometry of the array relative to the ground is constantly changing. Emerging work from project SERDP MM-1573 indicates that the resulting variation in the background response can be significant and has the potential to degrade the accuracy of any polarization tensors extracted from the data. With knowledge of the array geometry relative to the ground, variations in the background response can be modeled and removed from the data. We recommend testing the effectiveness of using an accurate digital elevation model and the three-dimensional position/ orientation of the array as inputs in a background correction procedure. The high-resolution DEM could be obtained by including four or more acoustic altimeters on the front of the TEMTADS array (a set-up we have used successfully with the NRL/Sky Research HeliMag system).
6) Excitation of multiple axes: To be able to discriminate using feature vectors from all three polarizations, the object must be excited from a wide-range of different angles. In cued-mode, the TEMTADS achieves that by cycling through each of the 25 transmitters. In a mobile discrimination mode, there is not enough time to fire each transmitter separately. In the simulations section we investigated the performance of a the TEMTADS when four 1 m by 1 m transmitters are incorporated into the system. In principal it's possible to fire multiple TEMTADS transmitters at the same time. If all five-transmitters in the central row are fired, the transmitter would produce a field equivalent to a 2 m by 0.4 m transmitter. As shown in Figure 34a, this field would be vertical along the row, and would be approximately horizontal 0.4 meters in front, or behind that row of transmitters. If the transmitter were fired every, say, 40 ms, as the array moved along a line, subsurface objects would be excited by varying amounts in

the vertical and the along-line horizontal directions. However, there would be very little excitation in the transverse horizontal direction. This is why systems like the MTADS EM array must conduct two perpendicular passes over an area in order to excite an object from three orthogonal directions. The multiple transmitters/receivers of the TEMTADS along the direction of travel open up the possibility of exciting the transverse horizontal components without the need to drive lines in a perpendicular direction. For instance, if 5 transmitters along a column (i.e. in the direction of travel) are fired, the field immediately under that column would be vertical, but the field on either side would be horizontal in the transverse direction (Figure 34a with rows and columns changed). Because there are 5 receivers and transmitters along the direction of travel, each column would not need to be fired as often as the central row. For instance, a possible firing sequence would be to fire the central row every-second measurement, and then one of the five columns for every other measurement. Therefore, 10 measurements would be required for one whole sequence (r3, c1, r3, c2, r3, c3, r3, c4, r3, c5 where r3 represents row number 3 etc), and with a 40 ms measurement time, this would translate to 0.4 seconds or 40 cm of movement at 1 m/s. At that point, the measurement sequence would be repeated and as the array continued to traverse down the line, objects would be excited from the vertical and the along- and across-track directions. Horizontal fields in the transverse direction could also be obtained by firing one or more transmitters in opposite directions (Figure 34b). Assuming balanced currents, the field in the middle of the two transmitters would be horizontal. While in principal it's possible to fire multiple TEMTADS transmitters at the same time, there may be design constraints that preclude that possibility. In addition, we do not yet know if the transmitter current in the smaller 40 cm loops will be large enough to provide sufficient SNR for detection and discrimination at depths approaching 11 times the diameter of an ordnance item. We recommend conducting some initial feasibility tests at the project outset to determine if the existing transmitters can be utilized in a one-pass detection and discrimination mode. If not, then larger more powerful transmitters will need to be constructed and aligned in such a way that there is good excitation in all three orthogonal directions.

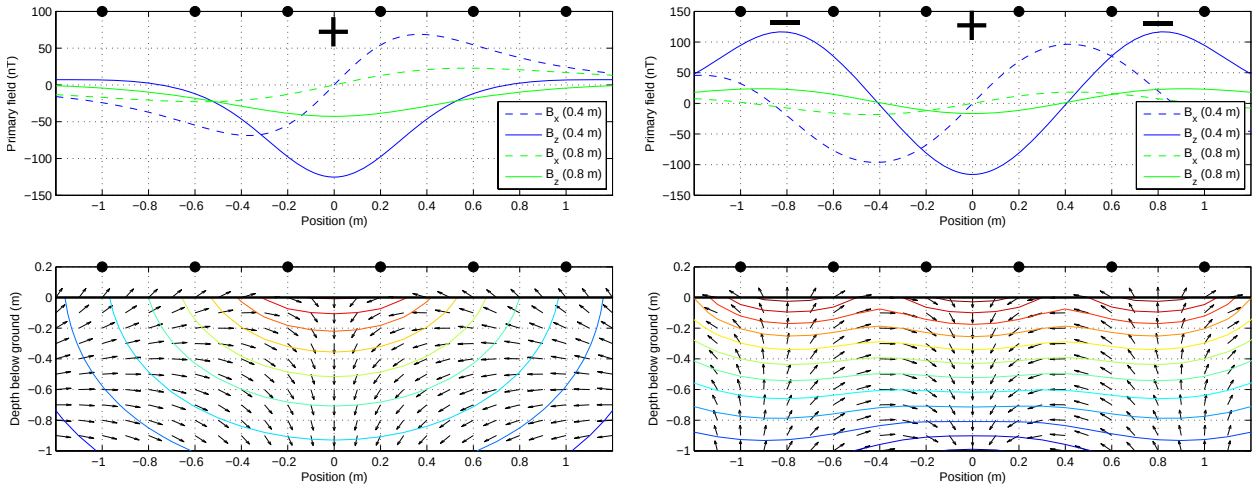

Figure 34: Cross section of the primary field pattern from the TEMTADS array: (a) when the center column (or row) is fired; and (b) when the two outer columns (or rows) are fired in opposition to the center column (or row). The black dots show the positions of the transmitter loops. The top-row shows the horizontal and vertical fields at two depths, while the bottom row shows the field direction and strength in a slice below the array.

6 REFERENCES

Billings, S. D., Pasion, L. R., Beran, L., Oldenburg, D., Sinex, D., Song, L., Lhomme, N., 2007, ESTCP MM-0504, Practical Discrimination Strategies for Application to Live Sites: Demonstration Report for the Former Lowry Bombing and Gunnery Range: ESTCP Program Office.

Billings, S. D., Pasion, L. R., Beran, L., Oldenburg, D., Sinex, D., Song, L., Lhomme, N., 2008, ESTCP MM-0504, Practical Discrimination Strategies for Application to Live Sites: ESTCP Program Office.

Bell. T., 2005, Geo-location Requirements for UXO Discrimination: *Paper prepared for UXO Location Workshop*, Annapolis, May 2005.

Carin L., Haitao, Y., Dalichaouch, Y., Perry, A. R., Czipott, P.V. and Baum, C. E., 2001, On the wideband EMI response of a rotationally symmetric permeable and conducting target: IEEE *Trans. Geoscience and Remote Sensing*, **39**, 1206-1213.

Curtis A., 1999, Optimal experiment design: Cross-borehole tomographic examples: *Geophys. J. Int*., **136**, 637-650.

Das, Y., McFee, J. E., Toews, J., and Stuart, G. C., 1990, Analysis of an electromagnetic induction detector for real-time localization of buried objects: *IEEE Trans. Geosci. Remote Sens*., **28**, 278-287.

Dennis, J. E. and Schnabel, R. B., 1996, *Numerical methods for unconstrained optimization and nonlinear equations*: SIAM, Philadelphia.

Foley, J. , R. Mehl, and N. Lhomme, 2008, UXO Navigation Technology, Draft Final Report, Draft Final Report Project SERDP MM-1441. August

Grewal, M., and A. Andrews, 1993, *Kalman Filtering: theory and practice*: Prentice-Hall, New Jersey.

Kalman, R., 1960, A new approach to linear filtering and prediction problems: *Transactions ASME Journal of Basic Engineering*, **82**, 35 - 44

Liao, X. and Carin, L., 2004, Application of the theory of optimal experiments to adaptive electromagnetic-induction sensing of buried targets: *IEEE Trans. Pattern Analysis Machine Intelligence*, **26**, 961-972.

Maybeck, P. S., 1979: *Stochastic models, estimation and control*: Academic Press, New York.

Menke, W., 1989, *Geophysical data analysis: discrete inverse theory*: Academic Press, New York.

Oldenburg, D. W., 1976, Calculation of Fourier transforms by the Backus-Gilbert method: *Geophys. J. Int*., **42**, 413-431.

Pasion L. R. and Oldenburg, D. W., 2001, A discrimination algorithm for UXO using time domain electromagnetics: *J. Eng. Environ. Geophys*., **28**, 91-102.

Smith, J. T., Morrison H. F. and Becker A., 2004, Resolution Depths for Some Transmitter-Receiver Configurations: *IEEE Transactions on Geoscience and Remote Sensing*, **42**, 1215-1221.

Steinhurst, D., Kadr, N., Barrows, B. and Nelson, H., 2005, Moving platform orientation for an unexploded ordnance discrimination system: *GPS World*, May 1 2005, 28-34.

Tarantola, A, 1987, *Inverse problem theory: methods for data fitting and model parameter estimation:* Elsevier, Amsterdam.

Welch, G., and G. Bishop, 2001: *An Introduction to the Kalman Filter*, Chapel Hill. SIGGRAPH.

Zhang, Y., Collins, L., Yu, H., Baum, C. E. & Carin, L., 2003, Sensing of Unexploded Ordnance with Magnetometer and Induction Data: Theory and Signal Processing. *IEEE Trans. Geosci. Remote Sensing*, **41**, 1005-1015.

APPENDIX A: FIGURES AND TABLES FROM MONTE CARLO SIMULATIONS

In this appendix, we include all figures and tables for each simulation of the 5 systems under various measurement errors.

The top panel of each figure displays the inverted parameters of (k, β, γ). In these scatter plots, the k_p and k_s represent the parameters for the primary and secondary polarizations that are chosen as the maximum and minimum values among the three inverted parameters, and β_p, β_s, γ_p, γ_s are found accordingly. After the primary and secondary quantities, the tertiary ones are defined. The middle panel shows the corresponding polarizations, denoted as the primary $L_p(t)$, secondary $L_s(t)$, and tertiary $L_t(t)$ polarizations with true polarization curves in shown in green. The bottom panel contains three scatter plots, derived from the recovered polarizations at the early and late times, for example, $t_1 = 0.18$ ms and $t_{21} = 10$ ms, which show how some additional information can be extracted for discriminator purpose. For instance, the bottom right plot measures the difference between the secondary and tertiary polarizations at t_1 and t_{21}. The small spread in late time in this plot indicates cylindrical symmetry.

The root-mean-square error (RMSE) and the standard deviation (SD) in the tables are defined as

$$\mathrm{SD} = \sqrt{\frac{1}{N_i}\sum_{j=1}^{N_i}\left(m_j - m_{\mathrm{true}}\right)^2} \tag{A-1}$$

and

$$\mathrm{RMS} = \sqrt{\frac{1}{N_i}\sum_{j=1}^{N_i}\left(\frac{m_j - m_{\mathrm{true}}}{m_{\mathrm{true}}}\right)^2} \tag{A-2}$$

to measure the difference or the spread of a recovered parameter of m_j in jth simulation from the true one of m_{true}. N_i is the simulation number for ith item.

Figures A-1 and A-2 and shows the results from cued array when $\alpha = 0.06$ and 0.6 in sensor noise.

Figures A-3 and A-4 show the results from the towed system of Single-Tx/25-Rx in which random measurement errors include sensor noise, perturbations in sensor orientation with a standard deviation of $\sigma_{\mathrm{orien}} = 2^0$, as well as perturbations in sensor position with a standard deviation of $\sigma_{\mathrm{pos}} = 2$ cm, 5 cm.

Figures A-5 and A-6 show the results from the towed system of 4-Tx/25-Rx in which random measurement errors include sensor noise, perturbations in sensor orientation with a standard deviation of $\sigma_{\mathrm{orien}} = 2^0$, as well as perturbations in sensor position with a standard deviation of $\sigma_{\mathrm{pos}} = 2$ cm , 5 cm.

Figures A-7 and A-8 show the results from the cart system of EM63-M in which random measurement errors include sensor noise, perturbations in sensor orientation with a standard deviation of $\sigma_{\text{orien}} = 2^0$, as well as perturbations in sensor position with a standard deviation of $\sigma_{\text{pos}} = 2$ cm , 5 cm.

Figures A-9 and A-10 show the results from the cart system of EM63 in which random measurement errors include sensor noise, perturbations in sensor orientation with a standard deviation of $\sigma_{\text{orien}} = 2^0$, as well as perturbations in sensor position with a standard deviation of $\sigma_{\text{pos}} = 2$ cm , 5 cm.

Figures A-11 and A-13 show the results from the cart system of EM63 in which random measurement errors are only from perturbations in sensor position with a standard deviation of $\sigma_{\text{pos}} = 1$ cm, 2 cm, and 5 cm.

Table A-1 list the statistical measures of Mean, SD, Min(imum), Max(imum), and RMSE for each set of recovered parameters of (k, β, γ) in the three polarizations using the cued array with different levels of sensor noise.

Table A-2 list the statistical measures of Mean, SD, Min(imum), Max(imum), and RMSE for each set of recovered parameters of (k, β, γ) in the three polarizations using the Single-Tx/25-Rx system with different levels of measurement errors arising from sensor noise as well as perturbations in sensor position and orientation.

Table A-3 list the statistical measures of Mean, SD, Min(imum), Max(imum), and RMSE for each set of recovered parameters of (k, β, γ) in the three polarizations using Four-Tx/25-Rx system with different levels of measurement errors arising from sensor noise as well as perturbations in sensor position and orientation.

Table A-4 list the statistical measures of Mean, SD, Min(imum), Max(imum), and RMSE for each set of recovered parameters of (k, β, γ) in the three polarizations using the EM63-M system with different levels of measurement errors arising from sensor noise as well as perturbations in sensor position and orientation.

Table A-5 list the statistical measures of Mean, SD, Min(imum, Max(imum), and RMSE for each set of recovered parameters of (k, β, γ) in the three polarizations using the EM63 system with different levels of measurement errors arising from sensor noise as well as perturbations in sensor position and orientation.

Table A-6 list the statistical measures of Mean, SD, Min(imum), Max(imum), and RMSE for each set of recovered parameters of (k, β, γ) in the three polarizations using Single-Tx/25-Rx system with measurement errors solely arising from different levels of perturbations in sensor position.

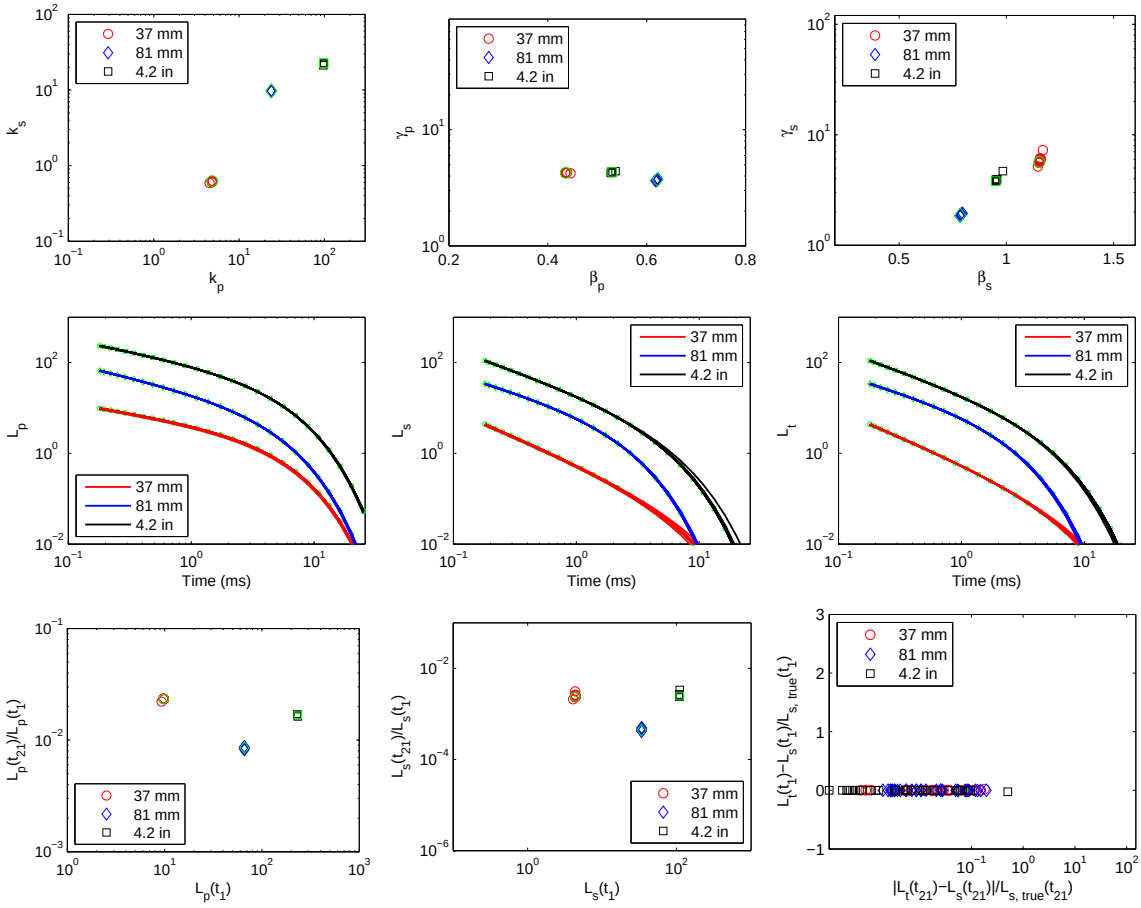

Figure A-1: The results of three-polarization inversion of noisy data using cued array with sensor noise of $\frac{0.06}{\sqrt{t}} * \mathrm{randn}$.

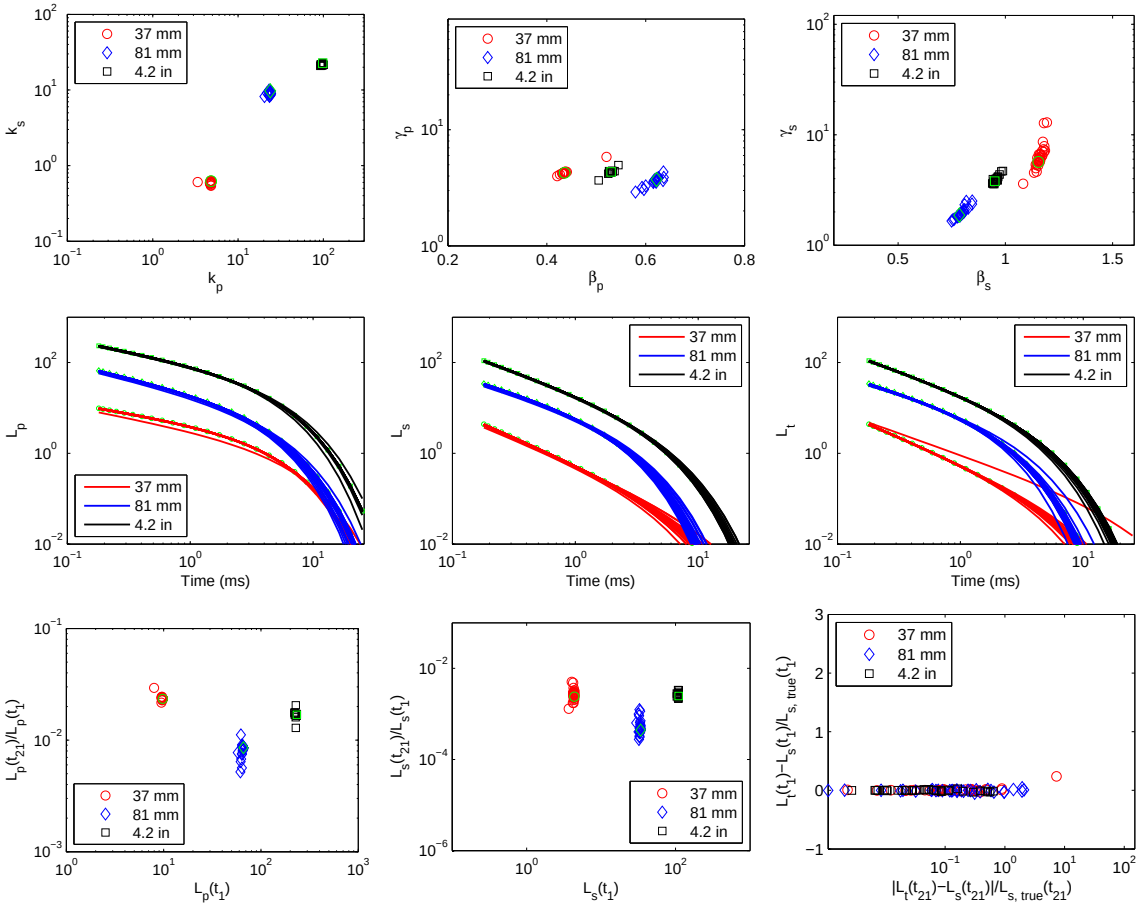

Figure A-2: The results of three-polarization inversion of noisy data using cued array with sensor noise of $\frac{0.6}{\sqrt{t}} * \mathrm{randn}$.

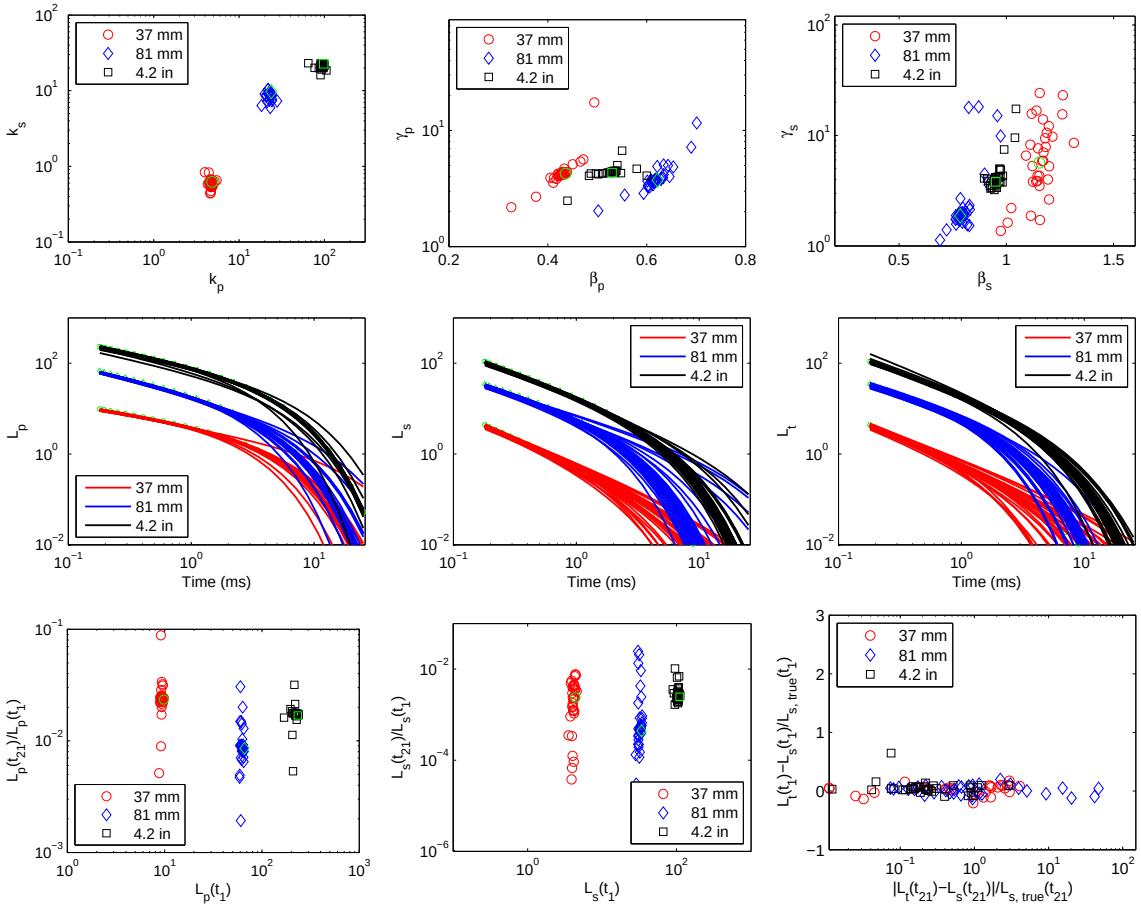

Figure A-3: The results of three-polarization inversion of noisy data using Single-Tx/25-Rx system. Measurement errors arising from sensor noise $(\frac{0.6}{\sqrt{t}} * \mathrm{randn})$ and perturbations in sensor position and orientation with $\sigma_{\mathrm{orien}} = 2^0$, $\sigma_{\mathrm{pos}} = 2$ cm.

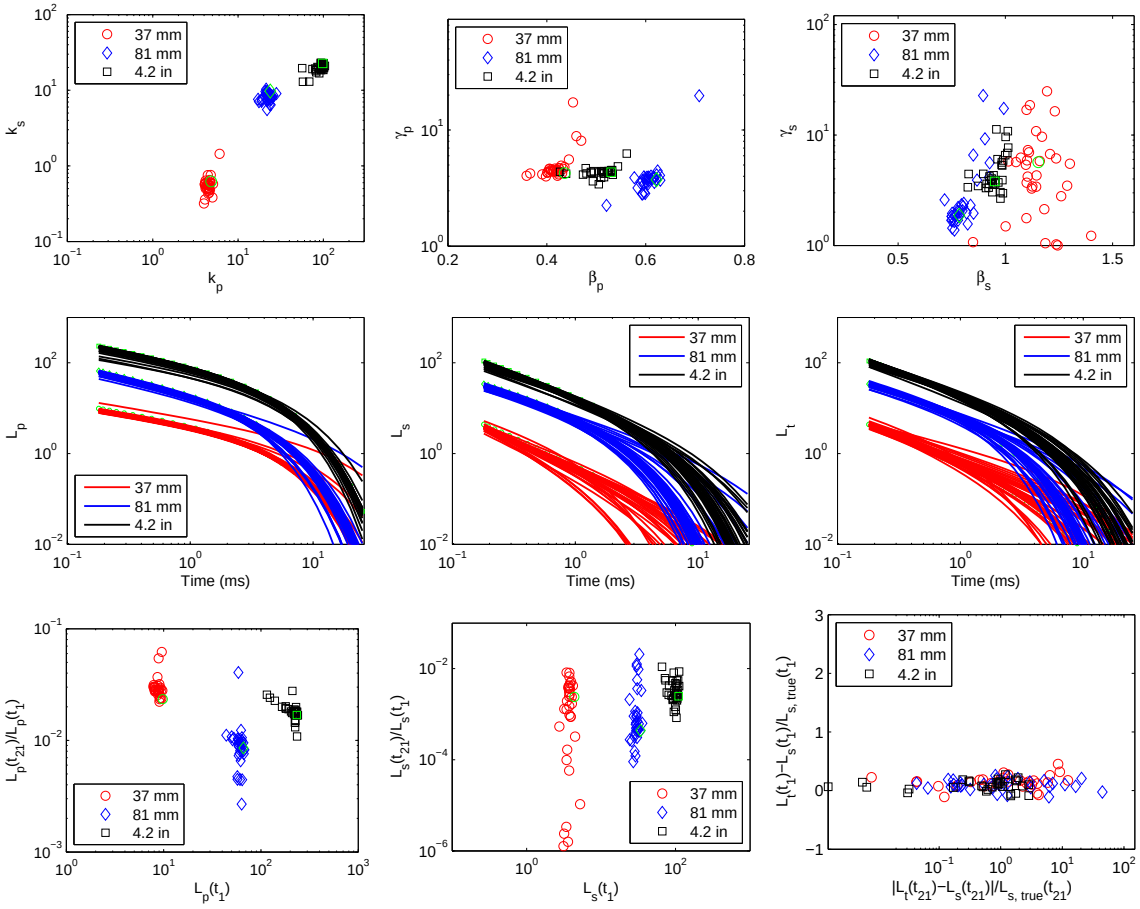

Figure A-4: The results of three-polarization inversion of noisy data using Single-Tx/25-Rx system. Measurement errors arising from sensor noise $(\frac{0.6}{\sqrt{t}} * \mathrm{randn})$ and perturbations in sensor position and orientation with $\sigma_{\mathrm{orien}} = 2^0$, $\sigma_{\mathrm{pos}} = 5$ cm.

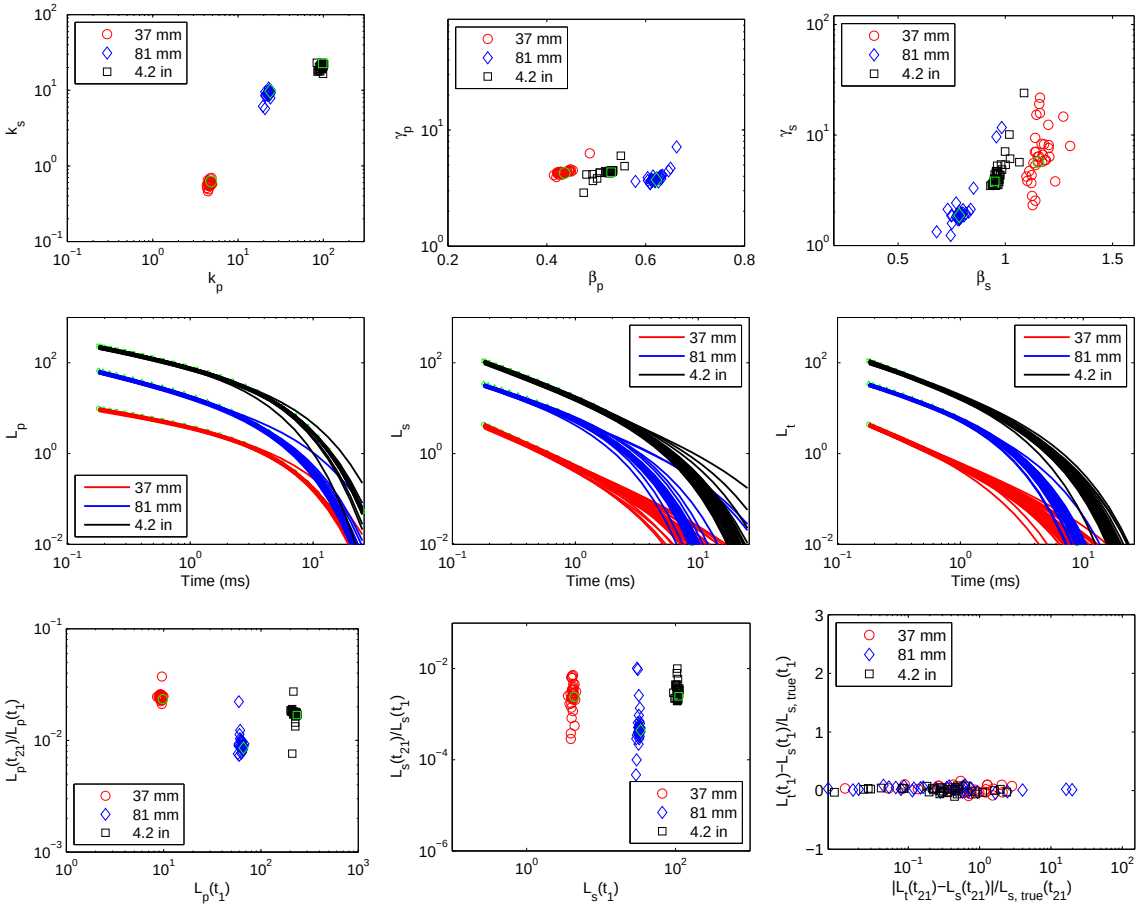

Figure A-5: The results of three-polarization inversion of noisy data using 4-Tx/25-Rx system. Measurement errors arising from sensor noise $(\frac{0.6}{\sqrt{t}} * \mathrm{randn})$ and perturbations in sensor position and orientation with $\sigma_{\mathrm{orien}} = 2^0$, $\sigma_{\mathrm{pos}} = 2$ cm.

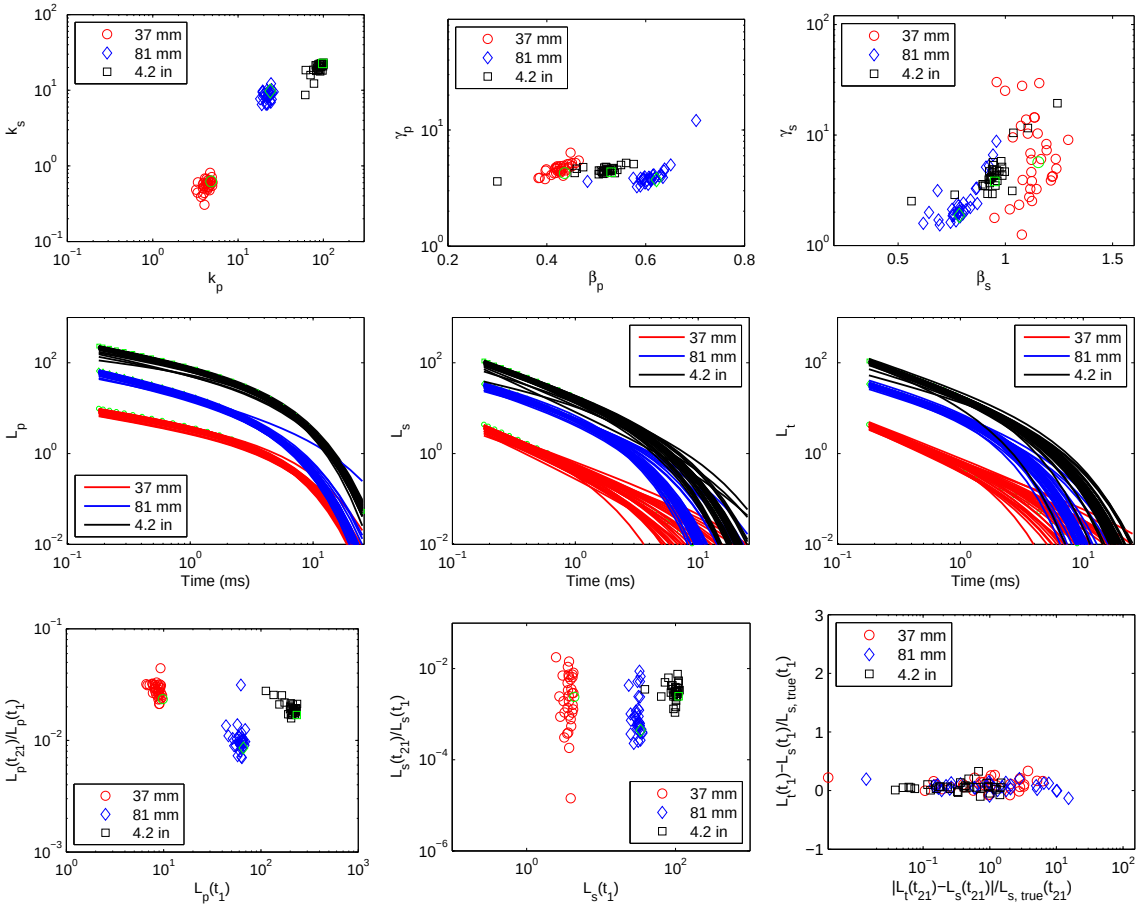

Figure A-6: The results of three-polarization inversion of noisy data using 4-Tx/25-Rx system. Measurement errors arising from sensor noise $(\frac{0.6}{\sqrt{t}} * \mathrm{randn})$ and perturbations in sensor position and orientation with $\sigma_{\mathrm{orien}} = 2^0$, $\sigma_{\mathrm{pos}} = 5$ cm.

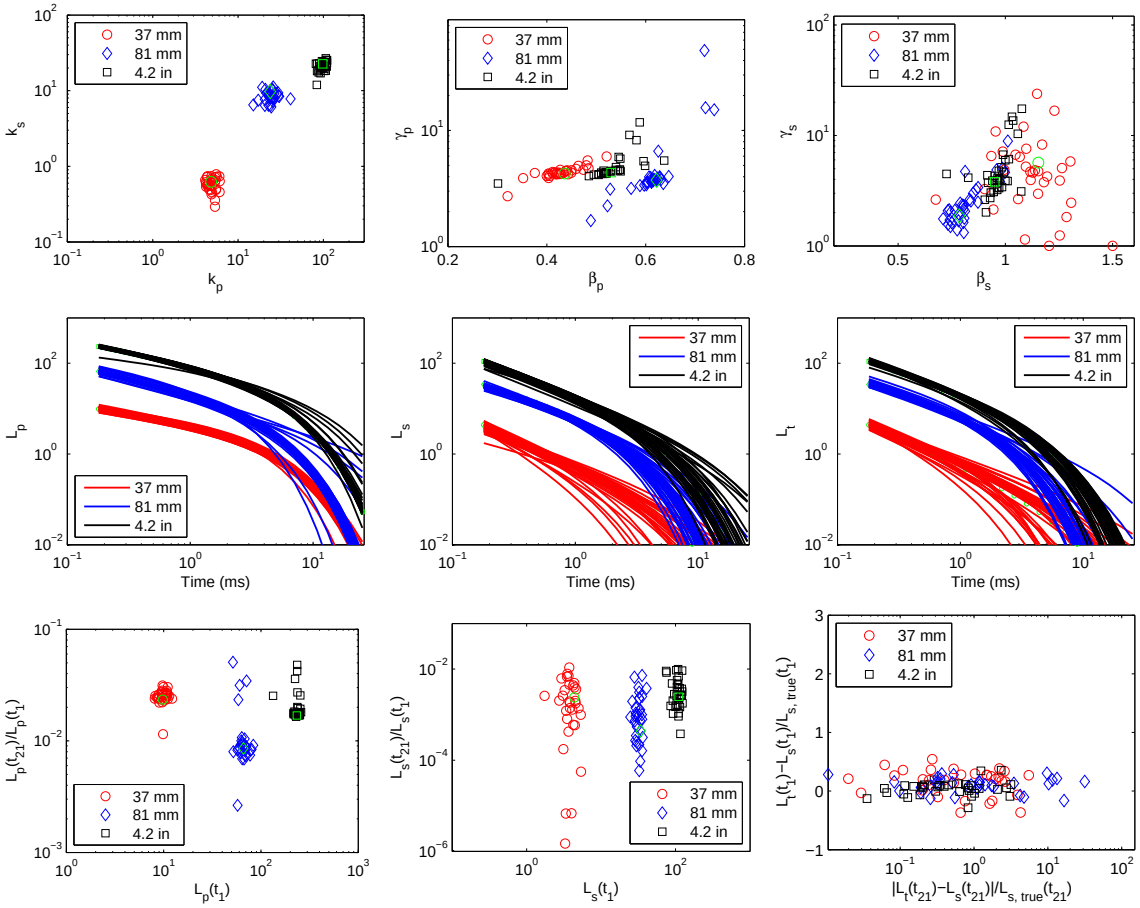

Figure A-7: The results of three-polarization inversion of noisy data using EM63-M system. Measurement errors arising from sensor noise $(\frac{0.6}{\sqrt{t}} * \mathrm{randn})$ and perturbations in sensor position and orientation with $\sigma_{\mathrm{orien}} = 2^0$, $\sigma_{\mathrm{pos}} = 2$ cm.

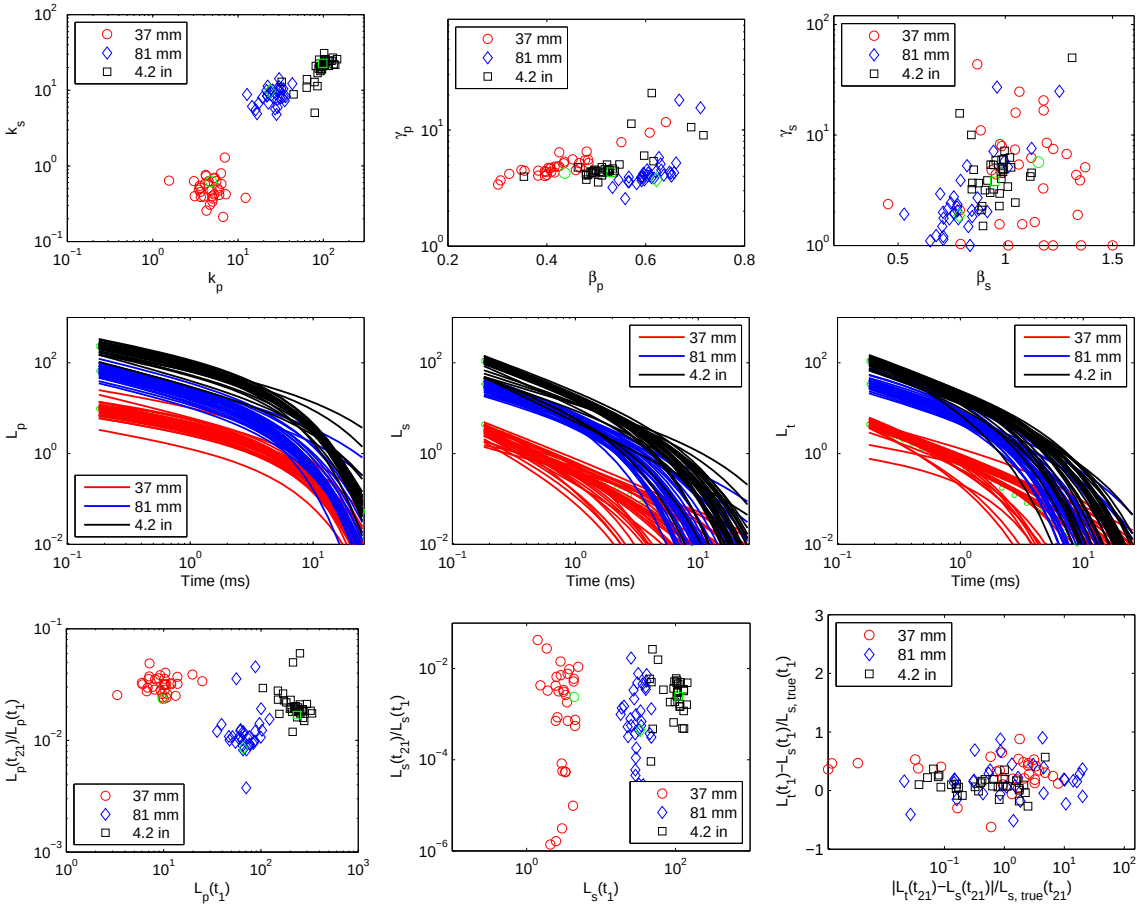

Figure A-8: The results of three-polarization inversion of noisy data using EM63-M system. Measurement errors arising from sensor noise $(\frac{0.6}{\sqrt{t}} * \mathrm{randn})$ and perturbations in sensor position and orientation with $\sigma_{\mathrm{orien}} = 2^0$, $\sigma_{\mathrm{pos}} = 5$ cm.

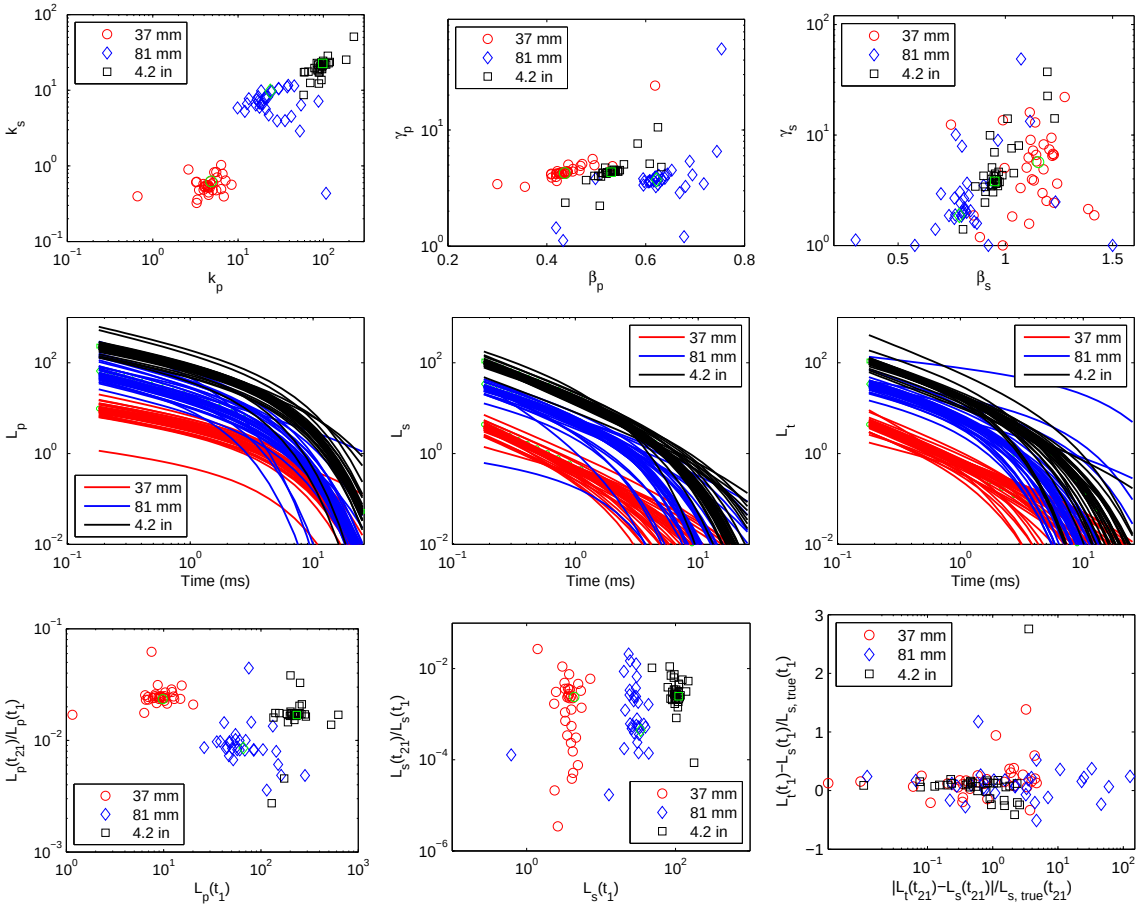

Figure A-9: The results of three-polarization inversion of noisy data using EM63 system. Measurement errors arising from sensor noise $(\frac{0.6}{\sqrt{t}} * \mathrm{randn})$ and perturbations in sensor position and orientation with $\sigma_{\mathrm{orien}} = 2^0$, $\sigma_{\mathrm{pos}} = 2$ cm.

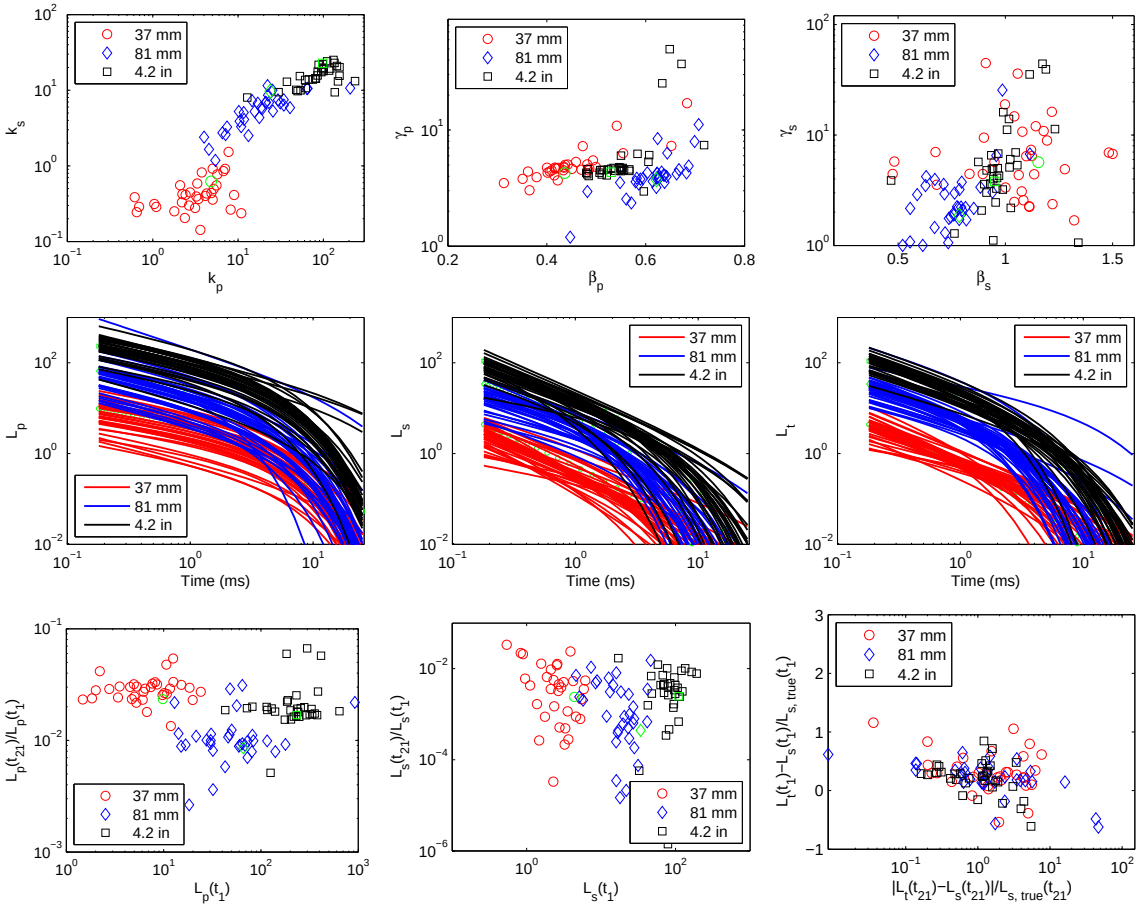

Figure A-10: The results of three-polarization inversion of noisy data using EM63 system. Measurement errors arising from sensor noise $(\frac{0.6}{\sqrt{t}} * \mathrm{randn})$ and perturbations in sensor position and orientation with $\sigma_{\mathrm{orien}} = 2^0$, $\sigma_{\mathrm{pos}} = 5$ cm.

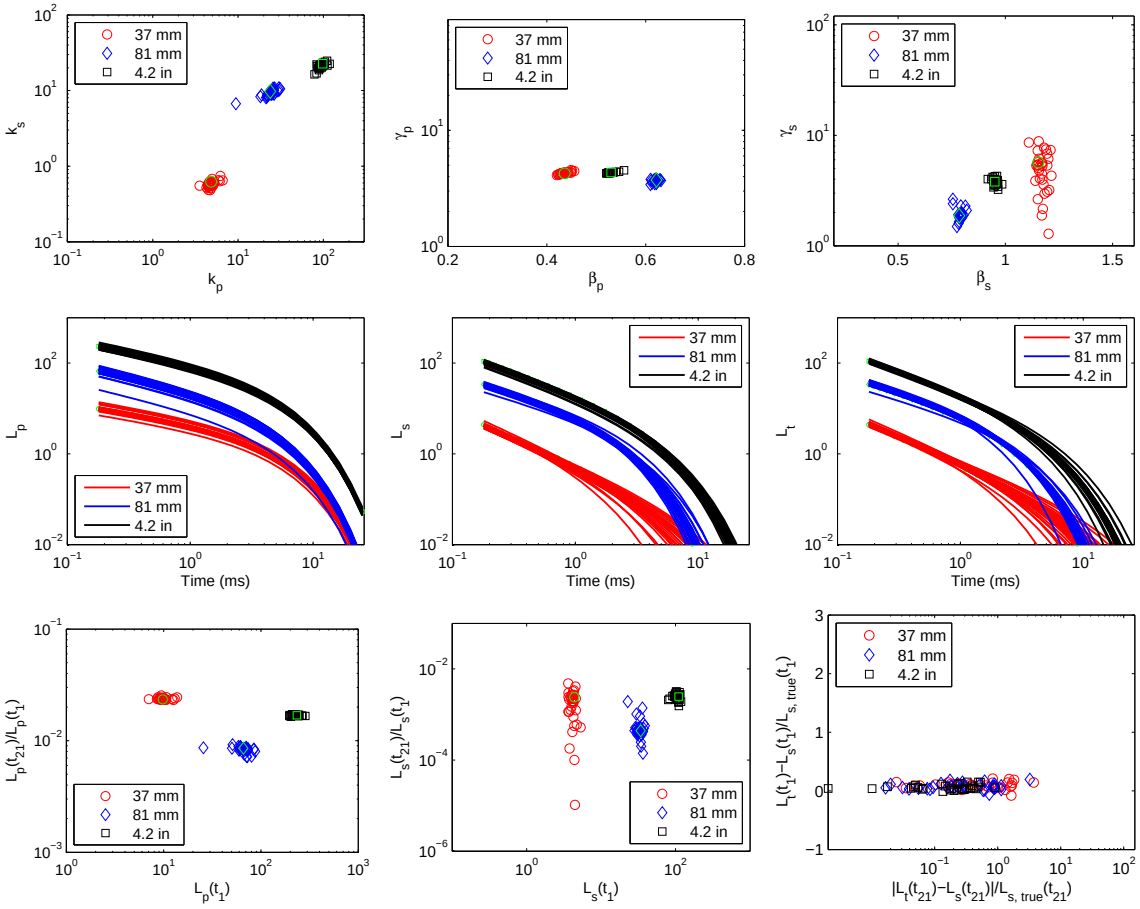

Figure A-11: The results of three-polarization inversion of noisy data using EM63 system. Measurement errors only arising from perturbations in sensor position with $\sigma_{\text{pos}} = 1$ cm.

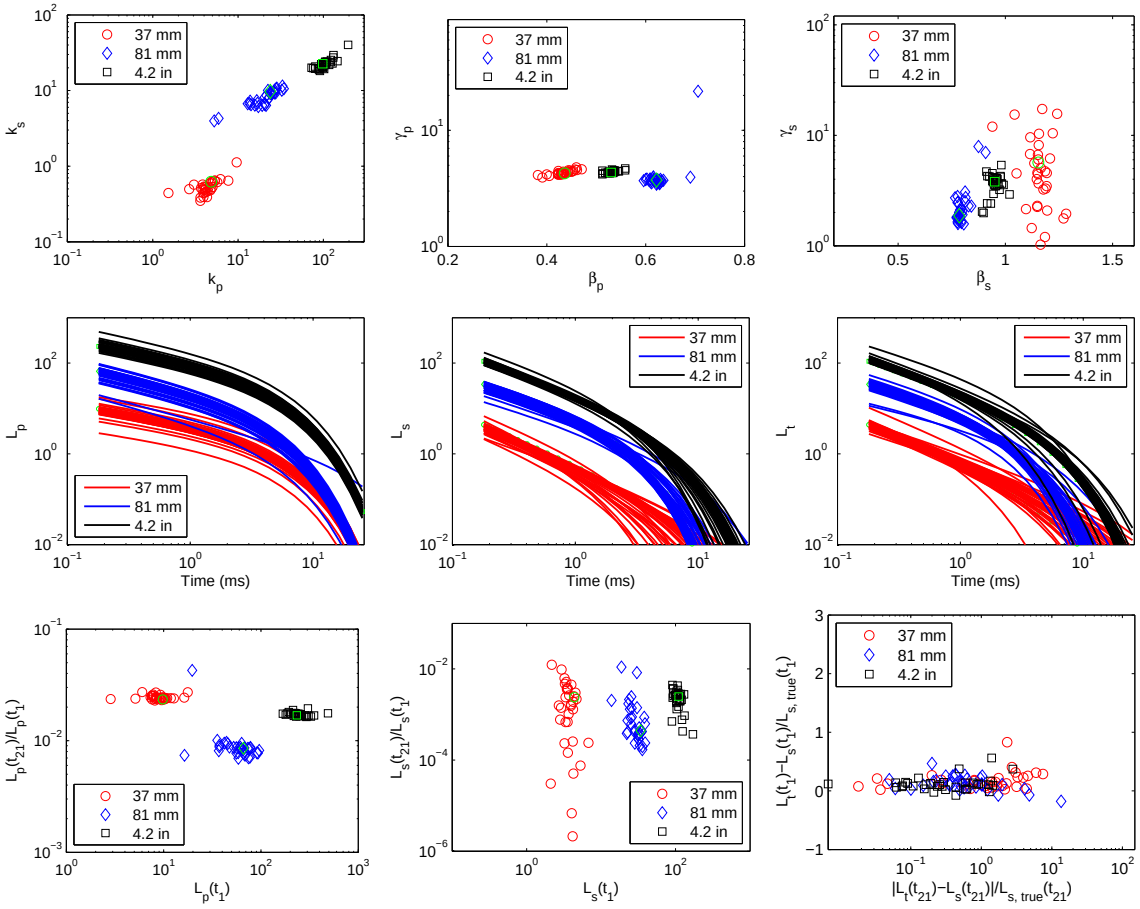

Figure A-12: The results of three-polarization inversion of noisy data using EM63 system. Measurement errors only arising from perturbations in sensor position with $\sigma_{\text{pos}} = 2$ cm.

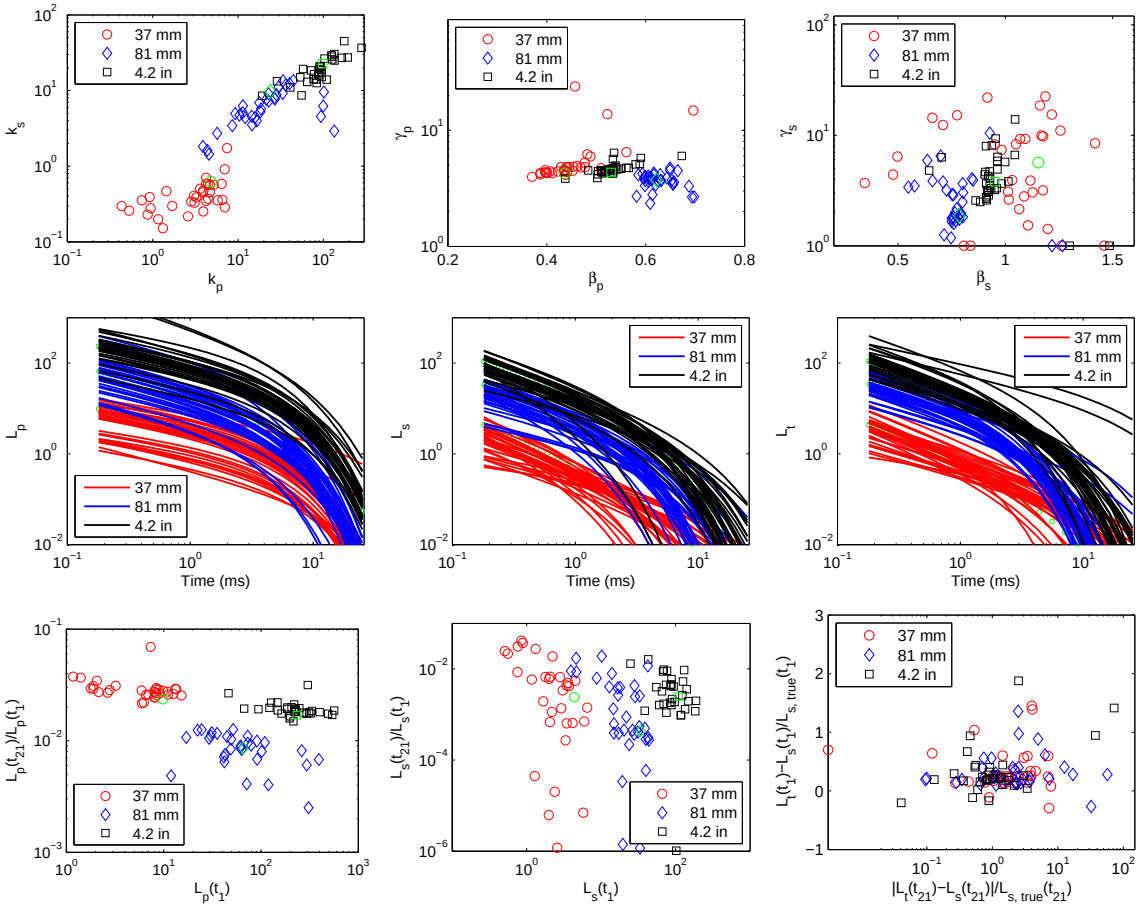

Figure A-13: The results of three-polarization inversion of noisy data using EM63 system. Measurement errors only arising from perturbations in sensor position with $\sigma_{\text{pos}} = 5$ cm.

Table A-1: Statistical results for 3-polarization inversion of noisy data using cued array.

Parameters	k_p	k_s	k_t	β_p	β_s	β_t	γ_p	γ_s	γ_t
Sensor noise: $0.06/\sqrt{t}$.									
	37 mm								
True	4.84	0.62	0.62	0.44	1.15	1.15	4.25	5.67	5.67
Mean	4.83	0.62	0.62	0.44	1.16	1.15	4.25	5.79	5.66
SD	0.06	0.01	0.01	0.00	0.00	0.01	0.01	0.33	0.25
Min	4.52	0.59	0.60	0.44	1.15	1.13	4.21	5.15	5.26
Max	4.85	0.63	0.63	0.45	1.17	1.17	4.28	7.25	6.85
RMSE	0.01	0.01	0.01	0.00	0.00	0.00	0.00	0.06	0.04
	81 mm								
True	23.88	9.73	9.73	0.62	0.79	0.79	3.73	1.87	1.87
Mean	23.88	9.71	9.77	0.62	0.79	0.78	3.73	1.88	1.86
SD	0.04	0.05	0.07	0.00	0.00	0.00	0.02	0.02	0.02
Min	23.80	9.55	9.72	0.62	0.78	0.77	3.65	1.85	1.79
Max	24.04	9.78	9.91	0.62	0.80	0.79	3.78	1.94	1.89
RMSE	0.00	0.01	0.01	0.00	0.00	0.00	0.01	0.01	0.01
	4.2 in								
True	98.30	22.60	22.60	0.53	0.95	0.95	4.33	3.80	3.80
Mean	98.25	22.53	22.66	0.53	0.95	0.95	4.33	3.84	3.77
SD	0.22	0.25	0.14	0.00	0.01	0.01	0.02	0.16	0.07
Min	97.18	21.22	22.54	0.53	0.95	0.92	4.23	3.77	3.45
Max	98.72	22.63	23.23	0.54	0.98	0.95	4.40	4.69	3.83
RMSE	0.00	0.01	0.01	0.00	0.01	0.01	0.01	0.04	0.02
Sensor noise: $0.6/\sqrt{t}$.									
	37 mm								
True	4.84	0.62	0.62	0.44	1.15	1.15	4.25	5.67	5.67
Mean	4.76	0.60	0.64	0.44	1.16	1.14	4.29	6.48	5.98
SD	0.26	0.03	0.06	0.02	0.02	0.04	0.28	2.04	3.26
Min	3.37	0.54	0.60	0.42	1.08	0.95	3.98	3.60	3.40
Max	4.85	0.63	0.94	0.52	1.19	1.17	5.83	12.92	23.78
RMSE	0.05	0.04	0.09	0.03	0.02	0.03	0.07	0.36	0.57
	81 mm								
True	23.88	9.73	9.73	0.62	0.79	0.79	3.73	1.87	1.87
Mean	23.51	9.37	9.86	0.62	0.79	0.77	3.66	1.96	1.79
SD	0.80	0.59	0.48	0.01	0.02	0.03	0.26	0.22	0.22
Min	20.42	8.19	8.62	0.58	0.75	0.66	2.91	1.66	1.31
Max	24.31	9.98	11.45	0.64	0.85	0.81	4.33	2.51	2.57
RMSE	0.03	0.06	0.05	0.02	0.03	0.04	0.07	0.12	0.12
	4.2 in								
True	98.30	22.60	22.60	0.53	0.95	0.95	4.33	3.80	3.80
Mean	97.33	22.17	22.81	0.53	0.96	0.94	4.33	3.91	3.61
SD	2.05	0.68	0.56	0.01	0.01	0.02	0.17	0.27	0.32
Min	92.43	20.88	21.28	0.50	0.94	0.90	3.66	3.58	2.79
Max	100.98	22.63	24.08	0.54	0.99	0.96	4.95	4.70	3.92
RMSE	0.02	0.03	0.02	0.01	0.01	0.02	0.04	0.07	0.08

Table A-2: Statistical results for 3-polarization inversion of noisy data using Single-Tx/25-Rx.

Parameters	k_p	k_s	k_t	β_p	β_s	β_t	γ_p	γ_s	γ_t
Sensor noise of $\frac{0.6}{\sqrt{t}} * \mathrm{randn}$ and sensor errors with $\sigma_{\mathrm{orien}} = 2^0$, $\sigma_{\mathrm{pos}} = 2$ cm.									
	37 mm								
True	4.84	0.62	0.62	0.44	1.15	1.15	4.25	5.67	5.67
Mean	4.69	0.60	0.72	0.43	1.15	1.07	4.59	7.83	8.17
SD	0.28	0.09	0.18	0.03	0.07	0.13	2.37	6.20	8.92
Min	3.97	0.44	0.57	0.33	0.97	0.77	2.18	1.37	1.00
Max	5.45	0.84	1.32	0.49	1.31	1.20	17.42	24.21	39.04
RMSE	0.06	0.14	0.29	0.06	0.06	0.11	0.56	1.09	1.57
	81 mm								
True	23.88	9.73	9.73	0.62	0.79	0.79	3.73	1.87	1.87
Mean	22.72	8.72	9.97	0.62	0.81	0.75	4.09	3.62	1.89
SD	1.95	1.42	1.27	0.03	0.06	0.07	1.60	4.84	4.84
Min	18.33	5.98	7.28	0.50	0.69	0.58	2.03	1.13	1.00
Max	28.01	10.43	12.87	0.70	0.97	0.87	11.59	18.16	4.84
RMSE	0.08	0.15	0.13	0.05	0.08	0.09	0.43	2.59	2.59
	4.2 in								
True	98.30	22.60	22.60	0.53	0.95	0.95	4.33	3.80	3.80
Mean	93.46	21.01	22.89	0.53	0.96	0.94	4.38	4.61	4.00
SD	8.53	2.09	1.61	0.03	0.03	0.03	0.55	2.69	0.83
Min	64.86	16.06	18.73	0.44	0.90	0.83	2.48	3.21	2.03
Max	105.63	23.11	27.72	0.60	1.04	1.05	6.70	17.41	6.34
RMSE	0.09	0.09	0.07	0.05	0.03	0.04	0.13	0.71	0.22
Sensor noise of $\frac{0.6}{\sqrt{t}} * \mathrm{randn}$ and sensor errors with $\sigma_{\mathrm{orien}} = 2^0$, $\sigma_{\mathrm{pos}} = 5$ cm.									
	37 mm								
True	4.84	0.62	0.62	0.44	1.15	1.15	4.25	5.67	5.67
Mean	4.50	0.57	0.82	0.42	1.15	1.01	5.09	6.18	10.81
SD	0.51	0.19	0.31	0.03	0.10	0.17	2.52	5.54	10.20
Min	3.99	0.32	0.61	0.36	0.85	0.69	3.98	1.00	1.18
Max	6.08	1.44	1.69	0.47	1.40	1.13	17.28	24.87	31.51
RMSE	0.11	0.30	0.50	0.07	0.09	0.15	0.59	0.98	1.80
	81 mm								
True	23.88	9.73	9.73	0.62	0.79	0.79	3.73	1.87	1.87
Mean	22.46	8.15	9.82	0.61	0.81	0.77	4.11	3.64	3.70
SD	2.71	1.88	1.69	0.03	0.07	0.09	2.83	4.86	4.86
Min	17.17	5.55	6.44	0.52	0.72	0.61	2.24	1.38	1.02
Max	28.14	10.30	12.93	0.71	0.99	0.97	19.75	22.72	24.91
RMSE	0.11	0.19	0.17	0.05	0.08	0.11	0.76	2.60	2.60
	4.2 in								
True	98.30	22.60	22.60	0.53	0.95	0.95	4.33	3.80	3.80
Mean	90.37	19.65	22.73	0.51	0.95	0.92	4.35	4.89	4.43
SD	14.14	3.72	2.18	0.03	0.05	0.06	0.43	2.42	1.45
Min	56.56	12.95	15.16	0.43	0.82	0.75	3.42	2.66	2.24
Max	104.26	22.98	26.99	0.56	1.01	1.02	6.26	11.26	8.40
RMSE	0.14	0.16	0.10	0.06	0.05	0.06	0.10	0.64	0.38

Table A-3: Statistical results for 3-polarization inversion of noisy data using 4-Tx/25-Rx.

Parameters	k_p	k_s	k_t	β_p	β_s	β_t	γ_p	γ_s	γ_t
Sensor noise of $\frac{0.6}{\sqrt{t}} * \mathrm{randn}$ and sensor errors with $\sigma_{\mathrm{orien}} = 2^0$, $\sigma_{\mathrm{pos}} = 2$ cm.									
	37 mm								
True	4.84	0.62	0.62	0.44	1.15	1.15	4.25	5.67	5.67
Mean	4.64	0.58	0.66	0.43	1.16	1.11	4.36	7.72	5.63
SD	0.26	0.06	0.08	0.01	0.05	0.06	0.38	5.08	2.73
Min	4.29	0.46	0.56	0.41	1.10	0.97	3.93	2.32	1.57
Max	4.98	0.69	0.94	0.49	1.30	1.17	6.29	21.78	13.10
RMSE	0.05	0.10	0.12	0.03	0.04	0.05	0.09	0.90	0.48
	81 mm								
True	23.88	9.73	9.73	0.62	0.79	0.79	3.73	1.87	1.87
Mean	22.81	9.06	10.00	0.62	0.79	0.76	3.91	2.44	1.79
SD	1.54	1.17	0.83	0.01	0.06	0.05	0.65	2.20	2.20
Min	19.55	5.72	7.44	0.58	0.68	0.66	3.44	1.23	1.26
Max	24.21	10.70	11.75	0.66	0.98	0.87	7.15	11.68	3.15
RMSE	0.06	0.12	0.08	0.02	0.07	0.06	0.17	1.18	1.18
	4.2 in								
True	98.30	22.60	22.60	0.53	0.95	0.95	4.33	3.80	3.80
Mean	95.08	20.82	22.80	0.52	0.97	0.93	4.33	5.13	3.72
SD	5.41	2.45	1.20	0.02	0.04	0.04	0.43	3.82	0.56
Min	83.69	16.48	19.78	0.47	0.93	0.81	2.88	3.46	2.26
Max	101.89	23.11	24.60	0.56	1.09	0.98	6.01	24.03	5.09
RMSE	0.05	0.11	0.05	0.04	0.04	0.04	0.10	1.01	0.15
Sensor noise of $\frac{0.6}{\sqrt{t}} * \mathrm{randn}$ and sensor errors with $\sigma_{\mathrm{orien}} = 2^0$, $\sigma_{\mathrm{pos}} = 5$ cm.									
	37 mm								
True	4.84	0.62	0.62	0.44	1.15	1.15	4.25	5.67	5.67
Mean	4.28	0.56	0.71	0.43	1.12	1.05	4.65	8.97	9.43
SD	0.73	0.12	0.14	0.02	0.08	0.12	0.64	8.67	9.87
Min	3.22	0.31	0.48	0.38	0.95	0.90	3.78	1.25	1.17
Max	5.03	0.81	1.07	0.46	1.29	1.24	6.37	30.13	43.16
RMSE	0.15	0.19	0.23	0.05	0.07	0.11	0.15	1.53	1.74
	81 mm								
True	23.88	9.73	9.73	0.62	0.79	0.79	3.73	1.87	1.87
Mean	22.40	8.70	10.13	0.61	0.79	0.75	4.12	2.65	2.10
SD	2.52	1.62	1.54	0.03	0.08	0.08	1.50	1.74	1.74
Min	18.15	6.46	7.02	0.48	0.62	0.52	3.24	1.54	1.10
Max	26.19	12.22	14.27	0.70	0.96	0.91	12.08	8.77	4.89
RMSE	0.11	0.17	0.16	0.06	0.10	0.10	0.40	0.93	0.93
	4.2 in								
True	98.30	22.60	22.60	0.53	0.95	0.95	4.33	3.80	3.80
Mean	88.54	19.85	22.80	0.51	0.95	0.90	4.52	5.00	3.73
SD	13.77	4.06	2.16	0.05	0.10	0.07	0.35	3.35	0.86
Min	61.28	8.65	16.45	0.30	0.56	0.71	3.61	2.52	1.22
Max	100.85	23.19	27.76	0.58	1.24	0.98	5.20	19.38	5.52
RMSE	0.14	0.18	0.10	0.09	0.11	0.08	0.08	0.88	0.23

Table A-4: Statistical results for 3-polarization inversion of noisy data using EM63-M.

Parameters	k_p	k_s	k_t	β_p	β_s	β_t	γ_p	γ_s	γ_t
Sensor noise of $\frac{0.6}{\sqrt{t}} * \mathrm{randn}$ and sensor errors with $\sigma_{\mathrm{orien}} = 2^0$, $\sigma_{\mathrm{pos}} = 2$ cm.									
	37 mm								
True	4.84	0.62	0.62	0.44	1.15	1.15	4.25	5.67	5.67
Mean	4.97	0.59	0.79	0.43	1.12	1.06	4.39	5.58	6.44
SD	0.58	0.12	0.28	0.04	0.15	0.16	0.53	4.62	6.23
Min	4.12	0.29	0.42	0.32	0.68	0.66	2.71	1.00	1.00
Max	6.09	0.79	1.69	0.52	1.50	1.37	5.98	23.84	30.01
RMSE	0.12	0.19	0.44	0.09	0.13	0.14	0.12	0.81	1.10
	81 mm								
True	23.88	9.73	9.73	0.62	0.79	0.79	3.73	1.87	1.87
Mean	24.48	8.50	10.36	0.62	0.82	0.78	5.74	2.70	2.62
SD	4.45	1.80	2.04	0.05	0.09	0.08	8.38	1.71	1.71
Min	15.09	6.10	6.85	0.49	0.71	0.64	1.68	1.32	1.22
Max	41.25	11.19	16.63	0.74	1.01	1.01	48.76	8.90	16.84
RMSE	0.19	0.19	0.21	0.08	0.11	0.10	2.24	0.92	0.92
	4.2 in								
True	98.30	22.60	22.60	0.53	0.95	0.95	4.33	3.80	3.80
Mean	97.48	21.21	25.19	0.53	0.97	0.90	4.99	5.47	3.39
SD	8.30	3.29	3.48	0.05	0.07	0.08	1.76	4.09	0.88
Min	81.64	11.91	20.18	0.30	0.73	0.75	3.49	2.01	1.81
Max	110.68	26.75	31.28	0.64	1.08	1.05	11.74	17.45	4.46
RMSE	0.08	0.15	0.15	0.10	0.07	0.09	0.41	1.08	0.23
Sensor noise of $\frac{0.6}{\sqrt{t}} * \mathrm{randn}$ and sensor errors with $\sigma_{\mathrm{orien}} = 2^0$, $\sigma_{\mathrm{pos}} = 5$ cm.									
	37 mm								
True	4.84	0.62	0.62	0.44	1.15	1.15	4.25	5.67	5.67
Mean	5.01	0.52	0.89	0.43	1.08	0.96	5.21	8.03	9.60
SD	1.79	0.22	0.41	0.07	0.22	0.28	1.89	9.87	11.35
Min	1.56	0.21	0.52	0.30	0.45	0.33	3.39	1.00	1.00
Max	12.29	1.29	1.81	0.64	1.50	1.30	11.69	43.68	47.08
RMSE	0.37	0.36	0.65	0.17	0.19	0.24	0.44	1.74	2.00
	81 mm								
True	23.88	9.73	9.73	0.62	0.79	0.79	3.73	1.87	1.87
Mean	26.51	8.59	12.30	0.61	0.81	0.74	4.84	4.07	2.61
SD	7.28	2.42	6.06	0.04	0.14	0.12	3.30	6.22	6.22
Min	12.75	4.79	6.06	0.53	0.53	0.58	2.56	1.00	1.00
Max	43.18	14.23	32.51	0.71	1.25	0.96	18.09	27.15	12.07
RMSE	0.31	0.25	0.62	0.06	0.18	0.15	0.88	3.32	3.32
	4.2 in								
True	98.30	22.60	22.60	0.53	0.95	0.95	4.33	3.80	3.80
Mean	96.71	20.05	25.13	0.53	0.96	0.90	5.49	6.07	3.53
SD	23.91	6.20	6.03	0.06	0.10	0.12	3.43	8.49	1.78
Min	32.51	5.03	14.44	0.35	0.79	0.59	3.54	1.50	1.00
Max	144.89	30.87	37.86	0.72	1.31	1.13	20.83	50.00	10.28
RMSE	0.24	0.27	0.27	0.12	0.10	0.12	0.79	2.23	0.47

Table A-5: Statistical results for 3-polarization inversion of noisy data using EM63.

Parameters	k_p	k_s	k_t	β_p	β_s	β_t	γ_p	γ_s	γ_t
Sensor noise of $\frac{0.6}{\sqrt{t}} * \mathrm{randn}$ and sensor errors with $\sigma_{\mathrm{orien}} = 2^0$, $\sigma_{\mathrm{pos}} = 2$ cm.									
	37 mm								
True	4.84	0.62	0.62	0.44	1.15	1.15	4.25	5.67	5.67
Mean	4.69	0.57	0.79	0.44	1.13	1.06	4.94	6.25	9.15
SD	1.45	0.16	0.29	0.05	0.14	0.18	3.49	4.73	8.76
Min	0.66	0.32	0.41	0.30	0.75	0.61	3.24	1.00	1.00
Max	8.38	1.03	1.43	0.62	1.41	1.44	24.11	22.09	26.85
RMSE	0.30	0.26	0.46	0.11	0.12	0.16	0.82	0.83	1.54
	81 mm								
True	23.88	9.73	9.73	0.62	0.79	0.79	3.73	1.87	1.87
Mean	29.60	7.18	13.07	0.62	0.84	0.69	5.03	4.52	3.82
SD	21.48	3.59	13.15	0.07	0.20	0.15	8.11	8.71	8.71
Min	9.86	0.43	5.86	0.42	0.30	0.30	1.12	1.00	1.00
Max	107.31	11.62	82.52	0.75	1.50	0.83	50.00	48.75	49.99
RMSE	0.90	0.37	1.35	0.11	0.25	0.20	2.17	4.65	4.65
	4.2 in								
True	98.30	22.60	22.60	0.53	0.95	0.95	4.33	3.80	3.80
Mean	97.63	20.89	27.05	0.53	0.97	0.89	4.55	6.49	4.38
SD	31.76	6.86	12.32	0.04	0.09	0.12	1.35	7.35	5.38
Min	58.71	8.65	10.45	0.44	0.80	0.59	2.22	1.40	1.00
Max	228.19	50.93	71.36	0.63	1.23	1.04	10.56	37.34	33.74
RMSE	0.32	0.30	0.55	0.07	0.10	0.13	0.31	1.93	1.42
Sensor noise of $\frac{0.6}{\sqrt{t}} * \mathrm{randn}$ and sensor errors with $\sigma_{\mathrm{orien}} = 2^0$, $\sigma_{\mathrm{pos}} = 5$ cm.									
	37 mm								
True	4.84	0.62	0.62	0.44	1.15	1.15	4.25	5.67	5.67
Mean	4.02	0.47	0.83	0.45	1.04	0.92	5.30	8.65	8.82
SD	2.64	0.31	0.36	0.08	0.25	0.29	2.69	9.58	7.62
Min	0.61	0.14	0.30	0.31	0.47	0.41	3.03	1.69	1.00
Max	10.92	1.53	1.87	0.68	1.50	1.17	17.02	44.72	32.22
RMSE	0.55	0.50	0.58	0.17	0.22	0.25	0.63	1.69	1.34
	81 mm								
True	23.88	9.73	9.73	0.62	0.79	0.79	3.73	1.87	1.87
Mean	26.45	5.91	10.82	0.62	0.76	0.72	4.86	3.31	3.65
SD	34.96	4.69	9.74	0.07	0.13	0.13	3.78	4.39	4.39
Min	4.00	1.18	3.31	0.45	0.52	0.30	1.19	1.00	1.00
Max	205.94	11.50	56.73	0.88	1.11	0.87	22.55	25.50	29.22
RMSE	1.46	0.48	1.00	0.11	0.17	0.16	1.01	2.35	2.35
	4.2 in								
True	98.30	22.60	22.60	0.53	0.95	0.95	4.33	3.80	3.80
Mean	95.52	16.03	25.51	0.55	0.98	0.88	7.68	8.38	4.24
SD	44.10	8.03	10.35	0.06	0.15	0.12	10.44	11.44	1.56
Min	12.85	8.00	8.68	0.48	0.47	0.60	2.96	1.06	1.16
Max	234.68	25.17	49.55	0.72	1.34	1.06	49.73	44.09	7.71
RMSE	0.45	0.36	0.46	0.11	0.15	0.12	2.41	3.01	0.41

Table A-6: Statistical results for 3-polarization inversion using EM63. Only sensor positional errors.

Parameters	k_p	k_s	k_t	β_p	β_s	β_t	γ_p	γ_s	γ_t
Perturbations in sensor position with $\sigma_{\text{pos}} = 1$ cm.									
	37 mm								
True	4.84	0.62	0.62	0.44	1.15	1.15	4.25	5.67	5.67
Mean	4.91	0.58	0.69	0.44	1.17	1.13	4.28	5.07	6.40
SD	0.59	0.07	0.08	0.01	0.03	0.04	0.09	1.96	2.78
Min	3.54	0.48	0.58	0.42	1.11	1.03	4.11	1.29	1.50
Max	6.61	0.74	0.84	0.46	1.21	1.18	4.55	8.83	14.38
RMSE	0.12	0.11	0.14	0.02	0.02	0.04	0.02	0.35	0.49
	81 mm								
True	23.88	9.73	9.73	0.62	0.79	0.79	3.73	1.87	1.87
Mean	24.31	9.36	10.21	0.62	0.79	0.78	3.69	1.92	1.93
SD	3.95	0.99	1.27	0.01	0.01	0.01	0.10	0.22	0.22
Min	9.44	6.69	6.84	0.61	0.76	0.75	3.41	1.49	1.17
Max	31.11	10.91	12.81	0.63	0.82	0.81	3.79	2.64	2.78
RMSE	0.17	0.10	0.13	0.01	0.02	0.01	0.03	0.12	0.12
	4.2 in								
True	98.30	22.60	22.60	0.53	0.95	0.95	4.33	3.80	3.80
Mean	96.01	21.32	22.97	0.53	0.95	0.94	4.33	3.81	3.91
SD	8.83	2.16	1.46	0.01	0.01	0.01	0.05	0.24	0.40
Min	78.59	16.39	19.63	0.52	0.92	0.91	4.25	3.23	2.82
Max	118.28	24.79	26.14	0.56	0.98	0.97	4.53	4.28	5.13
RMSE	0.09	0.10	0.06	0.01	0.01	0.01	0.01	0.06	0.11
Perturbations in sensor position with $\sigma_{\text{pos}} = 2$ cm.									
	37 mm								
True	4.84	0.62	0.62	0.44	1.15	1.15	4.25	5.67	5.67
Mean	4.54	0.54	0.73	0.43	1.16	1.08	4.32	5.81	10.30
SD	1.41	0.16	0.22	0.02	0.06	0.10	0.19	4.28	7.85
Min	1.53	0.35	0.51	0.38	0.94	0.87	3.93	1.02	1.00
Max	9.62	1.12	1.57	0.47	1.28	1.18	4.80	17.31	29.36
RMSE	0.29	0.25	0.35	0.04	0.05	0.09	0.04	0.75	1.38
	81 mm								
True	23.88	9.73	9.73	0.62	0.79	0.79	3.73	1.87	1.87
Mean	21.53	8.14	9.67	0.62	0.80	0.77	4.24	2.38	2.14
SD	7.22	2.44	2.28	0.02	0.03	0.06	3.13	1.44	1.44
Min	5.25	3.97	4.23	0.60	0.77	0.53	3.43	1.58	1.40
Max	34.39	11.47	16.24	0.71	0.91	0.88	21.71	7.92	5.24
RMSE	0.30	0.25	0.23	0.03	0.04	0.07	0.84	0.77	0.77
	4.2 in								
True	98.30	22.60	22.60	0.53	0.95	0.95	4.33	3.80	3.80
Mean	105.60	22.57	26.15	0.53	0.95	0.93	4.38	3.69	3.88
SD	23.94	3.94	7.85	0.01	0.03	0.03	0.12	0.73	0.83
Min	72.64	18.19	20.64	0.51	0.89	0.80	4.19	1.98	1.44
Max	194.82	40.14	62.87	0.56	1.02	0.97	4.69	5.38	6.17
RMSE	0.24	0.17	0.35	0.02	0.03	0.04	0.03	0.19	0.22

Cont. of Table A-6.

Parameters	k_p	k_s	k_t	β_p	β_s	β_t	γ_p	γ_s	γ_t
Perturbations in sensor position with $\sigma_{\text{pos}} = 5$ cm.									
	37 mm								
True	4.84	0.62	0.62	0.44	1.15	1.15	4.25	5.67	5.67
Mean	3.53	0.44	0.78	0.45	1.01	0.95	5.87	7.53	12.28
SD	2.43	0.33	0.42	0.06	0.29	0.26	4.27	6.33	12.74
Min	0.43	0.15	0.30	0.37	0.34	0.40	3.98	1.00	1.04
Max	7.43	1.73	2.14	0.70	1.46	1.18	23.87	22.51	48.89
RMSE	0.50	0.53	0.67	0.14	0.25	0.23	1.00	1.12	2.25
	81 mm								
True	23.88	9.73	9.73	0.62	0.79	0.79	3.73	1.87	1.87
Mean	30.09	6.49	10.32	0.63	0.78	0.75	3.69	2.84	2.98
SD	31.56	4.65	5.27	0.03	0.14	0.05	0.56	2.09	2.09
Min	3.88	1.44	3.24	0.58	0.55	0.67	2.35	1.00	1.45
Max	134.34	13.57	24.40	0.70	1.27	0.86	4.74	10.45	14.43
RMSE	1.32	0.48	0.54	0.05	0.17	0.06	0.15	1.12	1.12
	4.2 in								
True	98.30	22.60	22.60	0.53	0.95	0.95	4.33	3.80	3.80
Mean	133.23	19.50	32.38	0.55	0.95	0.86	4.80	4.57	5.38
SD	142.04	8.91	23.03	0.09	0.14	0.13	0.80	2.63	5.27
Min	19.19	6.26	11.39	0.44	0.64	0.57	3.83	1.00	1.35
Max	679.48	45.04	98.00	0.87	1.49	0.97	6.60	13.93	24.81
RMSE	1.45	0.39	1.02	0.17	0.14	0.13	0.18	0.69	1.39